Visible light-driven catalysts for water oxidation: towards solar fuel biorefineries

Visible light-driven catalysts for water oxidation: towards solar fuel biorefineries

Kristine Rodulfo Tolod

Supervisors
Prof. Nunzio Russo (Politecnico di Torino)
Asst. Prof. Simelys Hernández (Politecnico di Torino)
Host institution's supervisor: Dr. Alessandra Quadrelli (CNRS -CPE Lyon)

A doctoral dissertation submitted for the degrees of
Doctor of Philosophy in Chemical Engineering (Politecnico di Torino)
Doctor of Philosophy in Chemistry (Université Claude Bernard Lyon 1)

Torino, Italy
March 12, 2019

I hereby declare that, the contents and organization of this dissertation constitute my own original work and does not compromise in any way the rights of third parties, including those relating to the security of personal data.

……

Kristine Rodulfo Tolod

Turin, 12 March 2019

Summary

Photoelectrochemical (PEC) water splitting is a direct way of producing a solar fuel like hydrogen from water. The bottleneck of this process is the photoanode which is responsible for the water oxidation side of the reaction[1,2]. Semiconductor metal oxides are preferred catalysts for this reaction because of their stability under oxidizing conditions and being generally low-cost. However, no single catalyst can fulfil all the requirements for an efficient water oxidation reaction. There are always trade-offs among the light-harvesting ability, the charge transport and charge transfer processes, and the catalyst's influence in the kinetics of the reaction.

In this work, the use of $BiVO_4$ as a photoanode was extensively studied in order to improve its photoactivity. $BiVO_4$ has a conduction band edge position that almost coincides with the thermodynamic hydrogen evolution potential, thus, it can promote an earlier photocurrent onset, and can generate a higher photocurrent in the low bias region compared to the other photoanodes. These properties are vital in obtaining a high overall operating current and can eventually lead to a higher STH efficiency. In addition, $BiVO_4$ has a relatively low band gap energy of 2.4-2.5 eV, which makes it readily absorb visible light[3]. Its theoretical maximum photocurrent density is 7.5 mA/cm^2. However, the drawbacks of using $BiVO_4$ photoanodes are poor electron mobility and poor water oxidation kinetics. Poor

electron mobility brings about the loss of the photon efficiency to electron-hole recombination[4]. Moreover, $BiVO_4$ is not a good water oxidation catalyst.

The optimization of $BiVO_4$ photoanode synthesis via thin film electrodeposition on FTO was performed. The factors affecting the photoelectrochemical activity such as the electrodeposition time, ratio of the Bi-KI to benzoquinone-EtOH in the deposition bath, and the calcination temperature, have been investigated by using the Central Composite Design of Experiments. Pristine monoclinic scheelite $BiVO_4$ photoanodes having a photocurrent density of $0.45 \pm 0.05 mA/cm^2$ at 1.23 V vs RHE have been obtained. It was shown that a high photocurrent density are generally dictated by the following physico-chemical properties: higher crystallite size, an optimal thickness, and a more compact, porous morphology. Furthermore, the following photoelectrochemical characteristics give rise to a higher photocurrent density: low onset potential, and a high donor density.

Surface states on the $BiVO_4$ surface give rise to defect levels, which can mediate electron-hole recombination via the Shockley-Read-Hall mechanism[5]. In order to minimize the inefficiencies due to electron-hole recombination and passivate the surface states, ultrathin overlayers of Al_2O_3 and TiO_2 were deposited to the $BiVO_4$ thin film electrodes in an ALD-like manner. This was also performed in order to protect the $BiVO_4$ surface from photocorrosion and increase its stability. A photocurrent density of $0.54 mA/cm^2$ at 1.23 V vs RHE was obtained for the Al_2O_3-modified $BiVO_4$, which was a 54% improvement from the bare $BiVO_4$ that demonstrated a photocurrent density of $0.35 mA/cm^2$ at 1.23 V vs RHE. A 15% increase in stability of the Al_2O_3- modified $BiVO_4$ electrode was also observed over 7.5 hours of continuous irradiation. Moreover, through surface capacitance measurements, it was shown that the Al_2O_3 overlayer was indeed passivating the surface states of the $BiVO_4$ electrodes. The nature of the $BiVO_4$ surface was studied in this chapter by investigating the reactivity of powder $BiVO_4$ with a chemical titrant. The existence of surface hydroxyl groups on $BiVO_4$ was confirmed and quantified (max 1.5 OH/nm^2) via chemical titration. The reaction of the $BiVO_4$ powder with one pulse of $AlMe_3$ and 1 pulse of H_2O showed that there were 1.2 molecules of CH_4 evolved per Bi-OH.

Meanwhile, there were no photocurrent density improvements that were observed for the TiO_2-modified $BiVO_4$ at the synthesis conditions that were used in this experiment.

The addition of Ni-Mo to bare $BiVO_4$ increases the photocurrent density by 3-fold, from 0.35 mA/cm^2 to 1 mA/cm^2 at 1.23 V vs RHE. This was mainly due to the much lower charge transfer resistance of this electrode with respect to bare $BiVO_4$. Moreover, the addition of Ni-Mo to $BiVO_4$ with an overlayer of 2 cycles of Al_2O_3 produces a photocurrent density (0.39 mA/cm^2 at 1.23 V vs RHE) that is lower than that of just $BiVO_4$ with Ni-Mo, and slightly higher than that of the bare $BiVO_4$ for potentials up to 1.3 V vs RHE. It is apparent that the charges were able to transfer more efficiently from the $BiVO_4$ surface to the Ni-Mo, than from the Al_2O_3 overlayer to the Ni-Mo. This very important interface needs to be further examined and optimized.

In this work, we were able to highlight which factors are important in the synthesis of $BiVO_4$, and how they affect the resulting photoactivity. We have also achieved the passivation of the $BiVO_4$ surface states using Al_2O_3, which is not well-explored in literature. Moreover, we were able to probe and discuss the nature of the $BiVO_4$ surface. This is a very fundamental knowledge and the first of its kind, to the best of our knowledge. A good understanding of this important semiconductor surface and its interactions will aid in the design of a more efficient $BiVO_4$ photoanode.

Acknowledgments

Three years ago, I was a planning engineer for the biggest oil company in the Philippines. During my 4-year stint in the industry, I have always had this hunger to build a career doing scientific research but I really never imagined that 3 years down the road, I will be writing this acknowledgement page on my thesis as a PhD candidate in Europe.

I am very grateful to the Erasmus+ PhD SINCHEM (Sustainable Industrial Chemistry) programme for the opportunity that it has given me to do this joint PhD in Politecnico di Torino (PoliTo) and Université Claude Bernard Lyon 1. The experience did not only make me mature as a researcher but also as an individual. I will be forever thankful to the SINCHEM coordinator, Prof. Stefania Albonetti of UniBo, Prof. Raffaele Pirone of PoliTo, and the rest of the SINCHEM consortium for awarding me this once-in-a-lifetime opportunity.

I started my PhD with a very basic background on photocatalysis. I owe it to my supervisors Prof. Nunzio Russo and Asst. Prof. Simelys Hernández for believing in what I can do and always leading me to the right direction whenever I get confused. I came in as a newbie in electrochemistry and I am very much thankful to them for imparting in me their experience and expertise in the field and teaching me all the techniques. Their constant guidance and feedback have made me a more confident and very curious researcher.

I am equally thankful to Dr. Alessandra Quadrelli, for putting a lot of faith in this chemical engineer to do organometallic chemistry. She took me in without any

background at all in organometallic chemistry. The experience has definitely put me out of my comfort zone but it taught me how to persevere and have a deeper understanding of the things that I do, as seen from a different perspective. She has pushed me to go in uncharted territory and I am grateful to have survived it with her guidance. And I will never forget that moment when she called a lot of offices in search for English-speaking doctors in Lyon because she noticed that I wasn't in top shape one day.

Collecting all the data requires a lot of assistance, especially when it comes to operating some analytical instruments. This thesis would not have been completed if not for the gracious help of Micaella Castellino of PoliTo for the XPS measurements, Mauro Raimondo of PoliTO for the FE-SEM and EDS, Fabio Deorsola and Camilla Galletti of PoliTO for the XRD measurements, Fatwa Abdi of Helmholtz-Zentrum Berlin for the rapid scan voltammetry measurements, Lhoussain Khrouz of ENS Lyon for the EPR measurements, Gleb Veryasov of CPE Lyon for the Raman spectroscopy, and Sebastián Murcia of IREC Barcelona and his peers in Aalto University for the Ni-Mo catalysts.

It is without doubt that doing a PhD in itself is quite gruelling and demanding, but doing it far from the comforts of home makes it even more difficult. I am grateful to the friends that I have found here in Europe, who have helped me through and supported me in all my endeavours, both professionally and personally. Many thanks to my SINCHEM peers and my friends Alba, Aisha, Pooja, Matilde, Tapish, Tahrizi, Erwin, and Ferenc, for the support, encouragement and good moments that we shared to relieve ourselves of stress. I also thank my colleagues in PoliTo for always lending a helping hand and my friends and colleagues in CPE Lyon for always looking out for me.

In everything that I do, my family has always been very supportive, even if it meant going away and living on the other side of the world. I am thankful to Papa for always letting me do the things that I want to do, and for never questioning my career decisions even if they make him very uncomfortable at times. I am equally grateful to my sisters Hazel, Sheryll, Renee, Minnie, Katrina, and Janine, for the encouragement at the times that I doubted myself. I don't really understand how they could have so much confidence in me to be able to accomplish the things that I do, without exactly understanding what I do ,and just really believing 100% that I can do it whatever it is. The same gratitude goes out to my Tita Nimfa and Auntie Meldy and their families, who always made sure that I have a family to run to here

in Europe, especially whenever I go to France or Luxembourg. The Christmases and New Year's Eves wouldn't have been as festive and enjoyable if not for you.

I am most especially grateful to Eugenio, first and foremost for all the love, and for always believing in me, bearing with me when my nerves get the better of me, and encouraging and enabling me to believe in myself in the most trying times. I think he is the one who suffered and endured the most during the crucial times of the PhD, when the pressure was the highest. Thank you so much for helping me find that motivation whenever I felt defeated, and for helping me out in however way you could. He always had bigger faith in me, much more than what I have for myself actually. My deepest gratitude also to the Gurrieris, for being very supportive and treating me like their own. I don't know what I did to deserve such a wonderful family, and I am very grateful for all the care and affection that they showered me throughout this journey.

Overall, it has been quite a roller coaster ride. It was a series of highs and lows, of eurekas and disappointments, of failing and winning. But without a doubt, these 3 years have been life-changing for me in a very very good way, and I have nothing but gratitude and appreciation to everyone that has been part of it.

Kristine

Glossary of Terms

ALD	atomic layer deposition
$AlMe_3$	trimethylaluminum
CA	chronoamperometry
CBM	conduction band minimum
CCDE	central composite design of experiment
CV	cyclic voltammetry
DRIFTS	diffuse reflectance infrared fourier transform spectroscopy
EIS	electrochemical impedance spectroscopy
EPR	electron paramagnetic resonance
FTO	fluorine-doped tin oxide
GC	gas chromatography
LSV	linear sweep voltammetry
MS	Mott-Schottky
OEC	oxygen evolution catalyst
OER	oxygen evolution reaction
PEC	photoelectrochemical
SPEIS	staircase potentio electrochemical impedance spectroscopy
TTIP	titanium isopropoxide
UHV	ultra-high vacuum
VBM	valence band maximum
XPS	X-ray photoelectron spectroscopy

Contents

List of Figures

List of Tables

Chapter 1

Introduction

1.1 Solar fuels

An economy which grows more complex by the day, and a growing population, demand the use of sustainable energy resources that are not damaging the environment. Several decades have passed after the industrial revolution, but the world is still largely dependent on fossil fuels, and the problem of meeting the energy demands with a sustainable infrastructure remains.

The Intergovernmental Panel on Climate Change (IPCC) has reported in its Fifth Assessment Report that the anthropogenic greenhouse gas emissions are the main causes of the unprecedented levels of the atmospheric concentrations of CO_2, CH_4, and N_2O in the last 800,000 years. They said that these have impacted the entire climate system, and that they are the primary cause of global warming since the 1950s[6]. Innovative scientific interventions are needed to fight the environmentally-degrading effects of a fossil fuel-reliant global energy mix.

Technologies that can harness the available renewable sources of energy are extremely necessary. For example, the sun provides an average incident solar energy of 120,000 TW on the Earth's surface. Of this, there is an estimated power generating capacity of 20 TW, which is more than what is necessary to support the world's energy consumption[7]. This is one of the main reasons why solar-based energy solutions are extremely promising because of the huge amount of resource that is available. The problem lies solely on devising an efficient technology that can convert the available solar energy into energy forms that are readily deliverable and useful for human consumption. The share of solar energy in the electricity grid is projected to increase as solar technology matures and the costs of solar infrastructure decline.

One of the main drawbacks of using solar energy is its intermittency, thus, it cannot be used as a reliable base load source of power like coal and other fossil fuels. Energy storage solutions for this intermittent resource have to be devised. A very promising way of implementing this is via the conversion of solar energy into chemical energy, the resulting fuels being called solar fuels. A photon possesses an energy of 1-3 eV, which is sufficient to promote many chemical reactions[7]. Solar fuels, i.e. hydrogen, methane, and methanol, are advantageous over the traditional battery systems because they offer a higher energy storage density and facilitate easier transport logistics. Among these solar fuels, the production of hydrogen from water splitting is very promising, mainly because of the use of water, another abundant resource, as a raw material.

1.2 Photoelectrochemical water splitting

Water splitting can be accomplished using several systems. First, a photovoltaic (PV) – electrolyzer system can be used. The PV – electrolyzer system employs devices which are commercially available - a photovoltaic panel and an electrolyzer. This is clearly a big advantage, because apart from being readily available, both devices can be optimized separately. However, the PV part of this system is bound by the Shockley-Queisser limit, with a calculated maximum of 33% solar conversion efficiency for a single-junction solar cell having a band gap of 1.4 eV. Moreover, the electrolyzers normally rely on noble metals as catalysts, thus, they are operated at higher current densities to be more economical[8]. Thus, there is the necessity of high overpotentials, typically at least 1.9 V, in order to operate the electrolyzer. On the other hand, photocatalytic systems have much simpler design, but the hydrogen and oxygen gases in these systems are produced together in the same compartment. This brings about safety issues and it is necessary to add gas separation processes. Alternatively, photoelectrochemical systems make use of a monolithic light-harvesting and water splitting device that produces the hydrogen and oxygen gases in separate electrodes.

Photoelectrochemical (PEC) water splitting is a direct way of producing a solar fuel like hydrogen from water. This process often makes use of semiconductor photoelectrodes that facilitate the conversion of solar energy to chemical energy. Because of this, the harvest and storage of solar energy become feasible, and the solar energy is converted to a form that can be easily stored.

Fujishima and Honda[9] started working with photoelectrochemical systems in 1972. They utilized a TiO_2 photoanode and a Pt black cathode to perform photoelectrochemical water splitting by irradiating the photoanode with ultraviolet (UV) light. This started the investigations in solar water splitting and the interest in the field has grown since then. Solar water splitting is a sustainable way of producing H_2, which is a clean source of fuel. In this process, liquid water is split into H_2 and O_2 gases using photoactivated catalysts, which use the photons coming

from the sun to directly convert the solar energy into chemical energy. This process typically makes use of semiconductor photoelectrodes for the energy conversion[7,10].

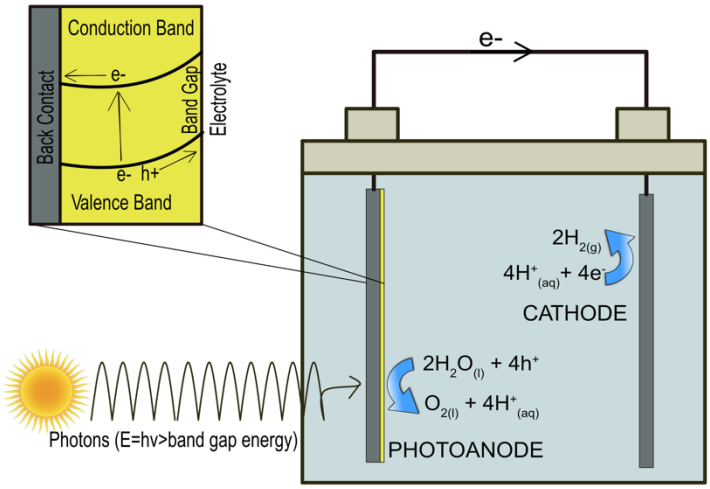

Figure 1. Schematic diagram of photoelectrochemical water splitting

A schematic diagram of a typical photoelectrochemical water splitting setup is shown in Figure 1. The system shown consists of a semiconductor photoanode and a cathode. A semiconductor consists of a valence band and a conduction band, and the energy gap between these two bands is called the band gap energy. When light with sufficient energy strikes the semiconductor, the electrons in the valence band are promoted to the conduction band, leaving holes in the valence band. The holes flow to the surface of the semiconductor and they participate in the water oxidation reaction that produces oxygen. Meanwhile, the electrons flow towards the conducting material and they get transported towards the cathode where they reduce H^+ ions to hydrogen gas.

For an efficient and sustainable process of splitting water into hydrogen and oxygen, several requirements have to be met simultaneously by the photoactive material[11,12]: (1) sufficient photovoltage and appropriate band alignment to split water, (2) substantial absorption of the solar spectrum, which is dominantly composed of visible light, (3) efficient and fast transport of charges between the semiconductor and the electrolyte solution, and (4) stability and cost-effectiveness. On-going researches on photocatalysis are in search of suitable materials that satisfy these requirements.

The bottleneck in the photoelectrochemical water splitting process is the photoanode, which is responsible for the water oxidation side of the reaction[1,2]. As shown in the following chemical equations, it is a 4-electron oxidation process of two water molecules, which is happening alongside the removal of two protons to form a weak oxygen-oxygen bond.

$$2H_2O \longrightarrow O_2 + 4H^+ + 4e^-$$
$$4H^+ + 4e^- \longrightarrow 2H_2$$
$$2H_2O \longrightarrow 2H_2 + O_2$$

Because it is a photochemical process, accumulated stepwise one-electron transfers are necessary under very specific photon-flux-density conditions. It is very challenging to keep an oxidized state in a desired microenvironment and to avoid quenching it while waiting for the arrival of the next photon[13].

Several molecular catalysts[14] and inorganic catalysts[15] may be used to catalyze the water oxidation reaction via photo-assisted methods. Preference is on the use of semiconductor metal oxides because of their stability under oxidizing conditions and being generally low-cost. The use of earth-abundant and non-noble metallic elements in these oxides is given special attention for economic purposes and sustainability interests.

No single catalyst can fulfil all the requirements for an efficient water oxidation reaction. As frequently seen in literature, there are always trade-offs among the light-harvesting ability, the charge transport and charge transfer processes, and the catalyst's influence in the kinetics of the reaction.

1.3 Visible light-responsive photocatalysts for solar water oxidation

1.3.1 Hematite (α-Fe_2O_3)

Hematite is a photocatalyst with a relatively good light-harvesting ability. It is stable in aqueous environment, abundant in nature, and is not harmful to the environment. Its band gap energy ranges from 1.9 to 2.2 eV, depending on the synthesis method[16]. This relatively low band gap is advantageous because a wider range of the visible light spectrum can be accessed as compared to other photoanodes used in solar water oxidation. It is also noteworthy that the maximum photocurrent density that can be generated from hematite with a band gap of 2.2 eV is relatively high. The photocurrent density can reach 12.6 mA cm^{-2} at 1.23 V vs RHE (reversible hydrogen electrode) at intensity of 1 sun, which corresponds to a maximum solar-to-hydrogen (STH) efficiency of 16.8%.

However, hematite has a low intrinsic electrical conductivity. The overall charge carrier decay for hematite is exceedingly fast, i.e. no measurable transient absorption occurs at ~100 ps, with 70 % of decay happening in only 8 ps[17]. Apparently, this was due to the intrinsic mid-bandgap states and trap states in the hematite, rather than the surface states. The transport of charges within the material is slow, which can aid in the recombination of photogenerated electrons and holes.

The hole diffusion length for hematite was reported to be very short at 2-20 nm[18,19]. The absorption depth for incident photons is 46 nm to 120 nm for wavelengths ranging from 450 nm to 550 nm[20]. The absorption depth refers to the depth at which 63% of the photons are absorbed. For hematite, the absorption depth needs to be thicker because of its indirect (d --> d) band gap transition[17]. This is a problem because it requires a relatively higher thickness to be able to absorb most of the incident photons, but at the same time, it has to be very thin to avoid fast electron-hole recombination brought about by the very short diffusion length. This value is shorter when compared to the hole diffusion coefficients of other water oxidation catalysts like TiO_2, WO_3, and $BiVO_4$.

Lastly, the position of the conduction band minimum of a hematite photoanode is too positive (0.3-0.6 V vs RHE)[18,19,21], thus, photogenerated electrons are not capable of H^+ reduction to H_2 at the cathode.

1.3.2 Tungsten oxide (WO_3)

Tungsten oxide (WO_3) is one of the few oxides that are chemically stable under aqueous acidic media. It is also nontoxic, inexpensive, and exhibits high resistance to photocorrosion. WO_3 can capture about 12 % of the solar spectrum and can absorb visible light up to 500 nm. The hole diffusion length of WO_3 is about 150 nm[22], which is much longer than hematite. The onset potential of WO_3 has been reported to be at ~ 0.5 V vs RHE[23], which is lower than that of hematite (0.8-1.1 V vs RHE[16,24,25]) and higher than $BiVO_4$ (0.25-0.44 V vs RHE) [26,27].

WO_3 crystals are formed by corner- and edge- sharing of WO_6 octahedra, giving rise to various phases such as monoclinic, triclinic, orthorhombic, tetragonal, and cubic WO_3. At room temperature, the most stable phase is the monoclinic WO_3 obtained between 17 ^oC and 330 ^oC. WO_3 used as photoanodes normally utilize the monoclinic phase. Annealing at 330 ^oC to 740 ^oC produces the orthorhombic structure and the tetragonal structure is formed at temperatures above 740 ^oC[28].

Moreover, WO_3 has an indirect band gap transition and its band gap energy is relatively high at 2.7 - 2.8 eV[29,30]. Also, its conduction band minimum is located at a relatively higher position of 0.24-0.73 V vs RHE[21,31] versus other photoanodes, thus, it also cannot reduce H^+ without an applied bias potential. It is also noteworthy that the formation and accumulation of peroxo species on WO_3 surface was shown to compete with the water oxidation reaction producing O_2, which causes a gradual loss of photoactivity[32].

1.3.3 Bismuth vanadate ($BiVO_4$)

$BiVO_4$ is commercially used as a yellow dye and it is known to be an inexpensive and nontoxic material. $BiVO_4$ has 3 main crystal forms: monoclinic scheelite, tetragonal zircon-type and tetragonal scheelite structure[33]. An irreversible transition from the tetragonal zircon-type to the monoclinic scheelite structure occurs at 400 ^oC to 500 ^oC. In addition, a reversible transition between the monoclinic-scheelite to the tetragonal scheelite structures occurs at 255 ^oC. Among the three crystal structures of $BiVO_4$, the monoclinic scheelite structure is the usual choice for photocatalysis because it demonstrated higher activity than the other structures[34].

The conduction band edge position of $BiVO_4$ is at 0.02 V vs RHE[33]. This is more strategic because it is more negative than that of Fe_2O_3 and WO_3, thus, it requires less bias potential than these photoanodes[33]. Because its conduction band edge position almost coincides with the thermodynamic hydrogen evolution potential, it promotes an earlier photocurrent onset, and can generate a higher photocurrent in the low bias region than the other photoanodes. These are vital in obtaining a high overall operating current and can eventually lead to a higher STH efficiency. In addition, $BiVO_4$ has a relatively low band gap energy of 2.4-2.6 eV[3,35,36], which makes it readily absorb visible light[3]. Its theoretical maximum photocurrent density is 7.5 mA/cm^2. Assuming all the photons with energies greater than 2.4 eV are absorbed, this translates to a 9% STH efficiency[37].

The drawbacks of using $BiVO_4$ photoanodes are poor electron mobility and poor water oxidation kinetics. Poor electron mobility brings about the loss of the photon efficiency to electron-hole recombination[4]. This was attributed to the fact that the VO_4 tetrahedra in $BiVO_4$ are not connected to each other, thus, the flow of photogenerated electrons towards the conducting support become more difficult.

$BiVO_4$ is not a good water oxidation catalyst, thus, it is usually coupled with an oxygen evolution reaction (OER) co-catalyst to improve the reaction kinetics. In addition, in order to maximize the photogeneration of charges, the thickness of the material has to be optimized according to the optical penetration depth. However, $BiVO_4$ has a short hole diffusion length that is estimated at 70-100 nm[38,39], which compromises and restricts the needed light penetration depth.

1.3.4 Comparison of various photoanodes

The following table summarizes the critical properties of some of the more prominent visible light-responsive photocatalysts for solar water oxidation, as reported in literature and in the previous section.

Table 1. Comparison of various visible light-responsive photoanodes

Photo-anode	Conduction band min (V vs RHE)	Valence band max (V vs RHE)	Band gap energy (eV)	Hole diffusion length (nm)	Onset potential (V vs RHE)
α-Fe_2O_3	0.3-0.6[18,19,21]	2.4-2.7[18,19,21]	1.9-2.2[16,17] (indirect)	2-20[18,19]	0.8-1.1[16,24,25]
WO_3	0.24-0.73[21,31]	3.0-3.45[21,31]	2.7-2.8[29,30] (indirect)	150[22]	~0.5[23]
$BiVO_4$	0.02[33]	2.5[33]	2.4-2.6[3,35,36] (direct/ indirect)	70-100[38,39]	0.25-0.44[26,27]

One of the main considerations in screening and choosing an appropriate semiconductor oxide as a photocatalyst is the proper alignment of the conduction and valence bands, relative to the potentials involved in the desired reactions. To effect a complete water splitting process, this necessitates that the conduction band minimum (CBM) should be more negative than the water reduction potential H^+/H_2 (0.0 V vs RHE), and the valence band maximum (VBM) should be more positive than the water oxidation potential O_2/H_2O (1.23 V vs RHE). As shown in Table 1, all the semiconductors satisfy the VBM requirement. It should be noted, though, that compared to many metal oxides having a VBM close to 3 V vs RHE, the VBM of $BiVO_4$ is less positive because of the incorporation of the Bi 6s orbital character to the typically dominant O 2p states in metal oxides[40] like α-Fe_2O_3 and WO_3. This is advantageous because it shifts the VB closer to the vacuum level, lowers the band gap, minimizes an overpotential that is otherwise wasted, and provides a relatively lighter effective mass for the holes, which can result to a better hole diffusion capability[40].On the other hand, the CBM requirement was not achieved by any of the materials. The closest value is for $BiVO_4$, which has a CBM that is almost coinciding with the water reduction potential. Therefore, none of these photocatalysts are solely capable of a complete photo-driven water splitting reaction, thereby, needing bias potentials to perform the whole process.

From Table 1, it can also be seen that the band gap energy of α-Fe_2O_3 is the most favourable, however, it possesses the shortest hole diffusion length and the highest onset potential. It should be mentioned that the materials with an indirect band gap transition such as α-Fe_2O_3 and WO_3, usually suffer from a larger light absorption depth. An optimal compromise between the light absorption depth and the hole diffusion length must be reached, because both parameters taken to the extreme will negatively affect the photoactivity of the photoanode. Moreover, a lower onset potential is significant because it allows to achieve a more practical performance at lower bias.

WO_3 suffers from having the highest band gap energy among the three, which negatively impacts its light harvesting ability as compared to α-Fe_2O_3 and $BiVO_4$. Having the longest hole diffusion length can be positive for its photoactivity,

however, as mentioned previously, the use of WO_3 also gives rise to the production of peroxo species, which is a competing reaction to the water oxidation reaction.

Considering these insights, this thesis focused on the use of $BiVO_4$ photoanodes for photoelectrochemical water oxidation. The intention was to use non-noble and earth-abundant materials, combined with scalable techniques, in order to produce a more practical and sustainable solution.

1.4 Thesis agenda

1.4.1 Objectives

The work described in this thesis is about the use of $BiVO_4$ as a photoanode for the water oxidation reaction. There were four main objectives:

- Optimize the performance of pristine $BiVO_4$ by identifying the important parameters and correlating them with the photocurrent density
- Probe the surface of $BiVO_4$
- Improve the stability of $BiVO_4$ by surface modification, i.e. deposition of a passivation layer
- Improve the water oxidation kinetics through the use of a co-catalyst

1.4.2 Overview

This thesis progresses as follows. Chapter 2 offers an extensive study of the $BiVO_4$ literature as a photoanode for water oxidation. It starts by summarizing the top-performing $BiVO_4$-based photoanodes to date, and identifying the strategies that were performed, which were done mainly to improve the electron mobility as well as the kinetics of the reaction. It finishes by explaining the gap and what strategies could be performed to address them.

Chapter 3 discusses the synthesis, characterization, and the photoactivity of bare $BiVO_4$ photoanodes that were synthesized via electrodeposition. It reports the findings on the effect of the electrodeposition time, the calcination temperature, and the composition of the electrodeposition solution on the photoactivity. It provides a comprehensive discussion about how the different material properties are correlated to the photoactivity, and how the studied factors impact these parameters. Moreover, more insights are presented considering the various photoelectrochemical characterization techniques.

Chapter 4 presents novel findings about the $BiVO_4$ surface characteristics. An organometallic chemistry approach was used to study the surface as well as to introduce surface modifications that could help improve the photoactivity and stability of this material. These surface modifications include the addition of

overlayers as well as a water oxidation co-catalyst, the results of which are thoroughly discussed.

Finally, Chapter 5 serves as the concluding chapter, which summarizes the major contributions of this work to the field. It also discusses the future directions moving forward.

Chapter 2

$BiVO_4$ as a photoanode

$BiVO_4$ was first synthesized by Roth and Waring in 1963 using solid state and melting reactions[41]. The interest in the study of $BiVO_4$ was initially due to its ferroelastic property, and its ferroelastic-paraelastic transition at 528 K (255 °C)[33], a property that depends on the crystal structure. As mentioned earlier, $BiVO_4$ has three main crystal forms, which are monoclinic scheelite, tetragonal zircon-type and tetragonal scheelite. Apart from the temperature-induced transitions that were mentioned in Chapter 1, it has also been reported that mechanical grinding at room temperature could irreversibly transform the tetragonal structure into a monoclinic structure[42]. Of the three $BiVO_4$ crystal structures, the monoclinic scheelite structure is the one that is most commonly used for photocatalysis because of its higher activity than the other structures[34].

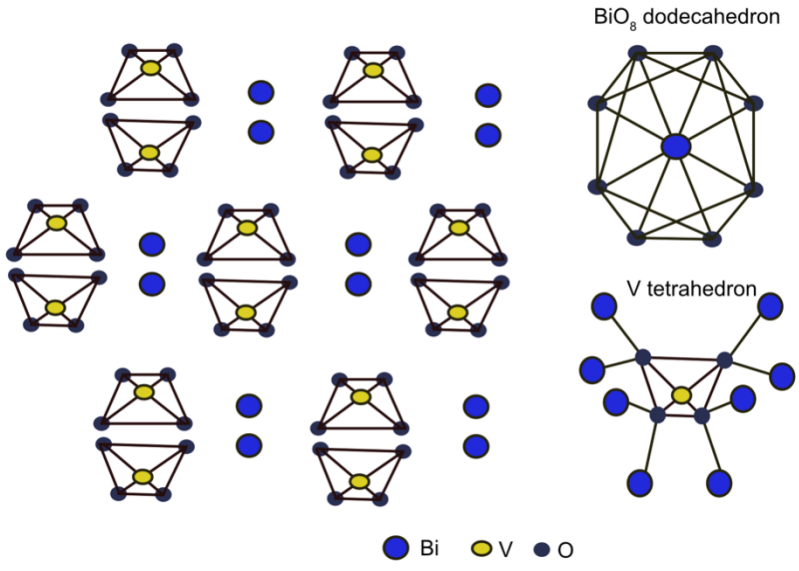

Figure 2. $BiVO_4$ monoclinic scheelite structure

The monoclinic scheelite structure of $BiVO_4$ is illustrated in Figure 2. The Bi in monoclinic scheelite $BiVO_4$ is coordinated to O in a distorted oxygen octahedron, while V is the centre of a distorted oxygen tetrahedron, thus implying oxidation states of Bi^{3+} ($5d^{10}6s^2$), V^{5+} ($3d^0$), and O^{2-} ($2p^6$), according to Walsh *et al*[43].

Moreover, the valence band mainly consists of O 2p, coupled to Bi 6s, while the conduction band is dominantly constituted by V 3d states, with contributions from the O 2p and Bi 6p states[43,44]. These couplings result in an upward dispersion of the valence band, and a lowering of the conduction band to a minimum, thereby causing relatively symmetric electron and hole masses, which facilitate an efficient charge carrier separation and extraction. As far as its calculated optical absorption spectrum is concerned, it has been reported that the fundamental band-edge transitions are dipole-allowed, beginning at 2.1 eV and with peaks at 2.4 eV, and thus, displays absorption in the visible light range. Cooper *et al*[44] stated that the poor electron mobility of $BiVO_4$ could be a consequence of the localization of the V 3d orbitals in the conduction band minimum, due to its poor overlapping with the Bi 6p orbitals.

In 1998, Kudo *et al*[3] first reported the photoactivity of a $BiVO_4$ powder for the water splitting reaction and measured the production of O_2 under visible light irradiation, in the presence of Ag^+ as a hole scavenger. This opened up huge interest in the photocatalysis field in which the potential of $BiVO_4$ has been explored as a photoanode.

2.1 Advantages of $BiVO_4$ as a Photoanode

$BiVO_4$ has a relatively low band gap energy of 2.4-2.6 eV, which makes it capable of readily absorbing visible light[3,45]. Moreover, as mentioned in Chapter 1, the conduction band edge position of $BiVO_4$ is favourably located, because it almost coincides with the thermodynamic hydrogen evolution potential[46,47]. This promotes an earlier photocurrent onset and the generation of a higher photocurrent in the low bias region than other photoanodes[48].

Finally, $BiVO_4$ is an inexpensive and nontoxic material that is composed of earth-abundant elements. In general, like most metal oxides, it is also known to be relatively stable against chemical corrosion[49,50].

2.2 Disadvantages of $BiVO_4$ as a Photoanode

The use of $BiVO_4$ as a photoanode also involves some drawbacks. $BiVO_4$ is known to suffer from poor electron mobility, and photon efficiency is therefore lost relatively easily to electron-hole recombination[4,51]. This phenomenon is reportedly due to the fact that the VO_4 tetrahedra are not connected to each other[52], thus making it hard for photogenerated electrons to flow towards the conducting support.

In addition, in order to maximize the photogeneration of charges, the thickness of the material has to be optimized according to the optical penetration depth[11]. However, $BiVO_4$ has a short hole diffusion length, estimated at 70–100 nm[38,39], which compromises and restricts the necessary light penetration depth.

Moreover, $BiVO_4$ has low intrinsic stability under extremely acidic (pH<3) or extremely basic conditions (pH>11), which are desirable for practical use in solar fuel generators[53].

Finally, $BiVO_4$ is known to exhibit poor water oxidation kinetics, which is a bottleneck that still has to be overcome in the design of photoanodes.

2.3 Top-Performing $BiVO_4$-based Photoanodes

The best-performing photoanodes that have been produced to date have been made via a combination of several techniques that address the issues associated with charge transport, charge transfer, and water oxidation kinetics.

The following sections present a summary of the reported photoactivities of the top-performing pristine and modified $BiVO_4$ photoanodes to date. All the photocurrent densities that are reported hereafter refer to standard conditions, under AM 1.5G illumination, illuminated under an intensity of 1 sun (100 mW/cm^2), and measured at 1.23 V vs. RHE.

2.3.1 Pristine $BiVO_4$

The best-performing pristine $BiVO_4$ that have been synthesized to date have been summarized in Table 2. Notably, the highest performance for pristine $BiVO_4$ that was obtained was the [001]-oriented $BiVO_4$ by Han *et al*[54], which was synthesized via a laser ablation technique. They showed that an effective crystal orientation and control of the exposed facet can result to better intrinsic properties of the $BiVO_4$. The (001) facet was reported to enhance electron transport by increasing the charge carrier density through the generation of oxygen vacancies under the oxygen-deficient conditions during synthesis[54]. This facet was also shown to exhibit a higher oxygen evolution reaction (OER) activity than other facets. Moreover, the chemical etching process that was performed in this photoanode enhanced the surface roughness, which enhanced the light absorption, as well as the specific surface area.

Table 2. Top-performing pristine $BiVO_4$ photoanodes

Photoanode	Photocurrent Density*(mA/cm^2)	Illuminated Area (cm^2)	Efficiency	Synthesis
Etched [001] – oriented $BiVO_4$[54]	4.9	0.24	IPCE 40-70%, 400-500 nm at 1.23 V vs RHE	Laser ablation

Nanoporous $BiVO_4$[55]	1.8	0.2	Not reported	Electrodeposition of Bi + drop-casting of V
Textured $BiVO_4$[53]	1.7	1.2 - 1.4	Peak External Quantum Efficiency (EQE): 30%	Spin-coating
Porous $BiVO_4$[56]	1.1	0.1 - 0.2	Not reported	Electrodeposition of Bi + drop-casting of V

*measured using AM 1.5G filter, intensity of 1 sun, at 1.23 V vs RHE

On the other hand, it should be noted that the less-studied electrodeposition synthesis of $BiVO_4$ also gave rise to a relatively high photocurrent density as compared to most of the work done in literature. Most of the reported pristine $BiVO_4$ photoanode performances rarely reach a photocurrent density above 1 mA/cm^2 at 1.23 V vs RHE, due to some intrinsic material inefficiencies. Because of these, several strategies to modify the $BiVO_4$ photoanode have been done in order to further improve its performance.

2.3.2 Modified $BiVO_4$

The best-performing modified $BiVO_4$-based photoanode reported are shown in Table 3. Among these $BiVO_4$-based photoanodes, the highest performance obtained was with the $WO_3/BiVO_4$ core-shell nanorod structure with Co-Pi, which was synthesized by Pihosh *et al*[57], and which yielded a photocurrent density of 6.72 mA/cm^2 at 1.23 V vs. RHE. The WO_3 layer was synthesized via glancing angle deposition (GLAD), the $BiVO_4$ via electrodeposition, and the cobalt phosphate (Co-Pi) oxygen evolution catalyst (OEC) was added via a photo-assisted electrodeposition. More details on the performancesare given in the following sections.

Table 3. Modified $BiVO_4$-based photoanodes with current densities > 3.5 mA/cm^2

Photoanode	**Photocurrent Density* (mA/cm^2)**	**Illuminated Area (cm^2)**	**Efficiency**	**Stability**
$WO_3/BiVO_4$ nanorods with Co-Pi[57]	6.72	Unspecified. Electrode Area: 0.226	IPCE 80%–90%, 400–500 nm at 1V vs. RHE	Not reported
W:$BiVO_4/V_2O_5$ with FeOOH/NiOOH[58]	6.6	0.5	Charge separation efficiency of 98.9% at 1.23 V vs RHE; Light absorption efficiency of 94.0%	About 6.6 mA/cm^2 at 1.23 V vs RHE after 2 h
Etched [001] – oriented $BiVO_4$ with Co-Pi[54]	6.1	0.24	Not reported	Photocurrent decay of 10% after 6 hours
SiO_x/Pt/SnO_2 Mo:$BiVO_4$nanocone with Fe(Ni)OOH[59]	5.82	0.25	IPCE >75%, <460 nm, at 1.23 V vs. RHE; APBE ~ 2.05% at 0.62 V vs. RHE	About 5.8 mA/cm^2 at 1.23 V vs. RHE for 5 h

WO_3/(W,Mo):$BiVO_4$ helix nanostructures with FeOOH/NiOOH[60]	5.35	Unspecified. Electrode Area: 2.25	IPCE 90%, 330–450 nm at 1.23 V vs. RHE	About 3 mA/cm^2 at 1.23 V vs. RHE for 7 days (8.7% decay)
EMI triflate ionic liquid BiVO4/FeOOH/NiOOH/Co (bpy-P)$_2$[61]	5.2	0.28	IPCE 60-90%, 400-450 nm at 1.23 V vs RHE	3.8 mA/cm^2 at 1.23 V vs RHE after 4h
N:$BiVO_4$ with FeOOH/NiOOH[48]	5.0	0.1–0.2	IPCE 50%–60%, 400–470 nm at 0.6 V vs. RHE	About 3.2 mA/cm^2 at 0.6 V vs. RHE for 30 h
(H, 3% Mo):$BiVO_4$with Co-Ci[62]	4.9	Unspecified	IPCE ~80%, 420 nm at 1.23 V vs. RHE	About 3.5 mA/cm^2 at 1.03 V vs. RHE for 12 h
Nanoporous $BiVO_4$ with FeOOH/NiOOH[55]	4.2	0.2	APBE 2.2% at 0.58 V vs. CE (Pt)	2.73 mA/cm^2 at 0.6 V vs. RHE for 48 h
SiO_x/Pt/SnO_2 Mo:$BiVO_4$nanocone[59]	4.18	0.25	ABPE about 0.75% at 0.87 V vs. RHE	Not reported
WO_3/(W, Mo):$BiVO_4$ with FeOOH/NiOOH[63]	4.0	Unspecified. Electrode area: 2.25	Not reported	Not reported
W(0%–1%) gradient-doped $BiVO_4$ with Co-Pi[26]	3.6	Unspecified	Carrier separation efficiency of up to 80%	Not reported
Nanoporous $BiVO_4$ with FeOOH[55]	3.6	0.2	Not reported	Not reported

*measured using AM 1.5Gfilter, intensity of 1 sun, at 1.23 V vs RHE

Looking at the reported stability of these modified $BiVO_4$-based photoanodes, it can be seen that obtaining a photo-stable material for practical applications still remains a challenge. The longest stability test that was performed on a $BiVO_4$ photoanode was done on WO3/(W,Mo):$BiVO_4$ helix nanostructures[60] with FeOOH/NiOOH, which only lasted for 7 days, with a corresponding 8.7 % decay on its performance.

2.4 Strategies to Enhance Reaction Kinetics

Oxygen evolution catalysts (OECs) improve the photocurrent density by reducing the kinetic barrier of water oxidation and providing unique catalytically active sites with specific selectivity[64]. They promote the negative shift of the overpotential, which promotes the use of less bias potential to achieve photoelectrochemical water oxidation[65].

As seen in Table 3, OECs are used in top-performing $BiVO_4$ photoanodes mainly to address the issue of poor water oxidation kinetics. A lot of efforts have been done to focus on the use of non-noble metals and earth-abundant materials as OECs.

The use of FeOOH as an OEC has shown an outstanding performance when used with $BiVO_4$ in the low-bias region, as reported by Seabold and Choi[32]. A photocurrent density of 1 mA/cm^2 was achieved with $BiVO_4$/FeOOH electrodes using an average bias potential of 0.6 V vs. RHE, while operating at a neutral pH condition in a phosphate buffer. In the presence of FeOOH, the photocurrent onset was negatively shifted by 0.5 V. In addition, a photocurrent density of 1.7 mA/cm^2 at 1.2 V vs. RHE was obtained and maintained for 6 h, with only 2 % of decay for $BiVO_4$/FeOOH, versus the significant decrease in the photocurrent that was observed within a few minutes for the bare $BiVO_4$. This suggests that the FeOOH layer induced the photostability of $BiVO_4$/FeOOH. For these reasons, the use of FeOOH as an OEC has been replicated in other studies[56,66].

Kim and Choi have shown that the use of NiOOH as an OEC for $BiVO_4$ exhibits an earlier photocurrent onset of 0.26 V vs. RHE, which is slightly lower than the 0.31 V vs. RHE that was obtained for $BiVO_4$/FeOOH. The authors also reported that the $BiVO_4$/NiOOH has a more negative flat band potential than the $BiVO_4$/FeOOH. However, a photocurrent density of 3.3 mA/cm^2 at 1.23 V vs. RHE has been reported for $BiVO_4$/NiOOH, a value which is lower than the 3.6 mA/cm^2 at 1.23 V vs. RHE for $BiVO_4$/FeOOH, under neutral pH conditions in a phosphate buffer. In the same study, Kim and Choi reported that an optimum dual OEC structure with FeOOH and NiOOH that are used in series is responsible for the simultaneous optimization of the $BiVO_4$/OEC and OEC/electrolyte junction[48,55]. A similar dual OEC structure was employed in several other studies to produce high-performing $BiVO_4$ photoanodes.

The in situ production of Co-Pi as an OEC was first presented by Kanan and Nocera[67]. In this method, oxygen is generated at neutral pH using Co-Pi under atmospheric pressure and room temperature. Co-Pi OEC also exhibits a self-healing nature in the presence of phosphate, which should ensure the long-term stability of the catalyst system[68]. A 2-fold increase in the photocurrent density that was accompanied by a 0.15 V vs. RHE cathodic shift in the onset potential was reported by Abdi *et al*[26]. Up to a 7-fold increase in photocurrent density was also reported, following the use of Co-Pi in several other studies as the use of Co-Pi became popular in the field[32,69,70].

In another work, Zhong *et al*[71] introduced CoO_x as an OEC. It was found to increase the photocurrent density of bare $BiVO_4$ from 1 mA/cm^2 to about 1.5 mA/cm^2 at 1.2 V vs. RHE, when tested at neutral pH in a phosphate electrolyte. The same authors then used the dual OECs NiOOH (deposited in situ)/CoOx with an ultrathin ALD-deposited NiO layer on top, and added them to a $BiVO_4$/Ti layer. This process was reported to triple the photocurrent density, yielding up to 3.5 mA/cm^2 at 1.23 V vs. RHE, at neutral pH in a phosphate electrolyte. The NiO functioned as a passivating layer for the $BiVO_4$ surface states, consequently enhancing charge separation.

Joya *et al*[72] reported the use of a cobalt carbonate (Co-Ci) OEC formed in situ. It was generated from a CO_2-saturated bicarbonate solution containing Co^{2+} ions. They reported that the Co-Ci OEC in a HCO^{3-}/CO_2 electrolyte showed a stable current density of about 2 mA/cm^2 at 1.35 V vs. NHE (normal hydrogen electrode), and it remained active for 16 h. It was also reported that Co-based OECs, such as Co-Pi and Co-Ci, tend to lose stability in phosphate electrolyte during anodic water oxidation, despite exhibiting a sustained current density and higher stability in a HCO^{3-}/CO_2system. Using the same OEC system at neutral pH, Jin Hyun Kim *et al*[73]reported a shift in the onset potential from 0.5 V vs. RHE to 0.2 V vs. RHE after adding Co-Ci to a $BiVO_4/WO_3$ photoelectrode. The Co-Ci/$BiVO_4/WO_3$material generated a photocurrent density of 3.5 mA/cm^2 at 1.23 V vs. RHE, which was higher than the 2.5 mA/cm^2 that was generated at the same potential by the $BiVO_4/WO_3$ without any additional OEC. In another work, Jin Hyun Kim *et al*[62]used the same OEC in a tandem cell assembly, using a H and 3 % Mo co-doped BiVO4 photoanode, which generated a photocurrent density of 4.8 mA/cm^2 at 1.23 V vs. RHE. It reached 5 mA/cm^2 at 1.23 V vs. RHE when it was enhanced by Co-Ci. This performance was similar to that of Co-Pi, but with higher stability.

From among all of the OECs that were discussed above, it should be noted that most of the photoelectrochemical tests were conducted using neutral pH electrolytes. This is an important consideration for $BiVO_4$-based photoanodes, because $BiVO_4$ gradually dissolves at extreme pH conditions in long experiments. Furthermore, operating under neutral pH conditions lowers the corrosivity of materials and other components of the system, although maintaining a high activity under neutral pH environment has been proven difficult. Thus, it is also essential to understand the stability of these OECs in different pH environments.

The electrocatalytic stability of OECs, such as CoOx, Co-Pi, CoFeOx, IrOx, NiOx, NiCeOx, NiCoOx, NiCuOx, NiFeOx, and NiLaOx has been tested in the OEC benchmarking work of McCrory *et al*[74,75]. The OECs were studied in both alkaline (1 M NaOH) and acidic (1 M H_2SO_4) environments, and held at a constant current density of 10 mA/cm^2 for 2 h at a 1600 rpm rotation rate while measuring the operating potential as a time function. Most of the catalysts have exhibited stable performances under alkaline conditions, showing only < 0.03 V shifts in overpotential, except for CoFeOx and IrOx, which were affected by catalyst dissolution and loss of material, respectively. Meanwhile, only the IrOx exhibited a stable overpotential of 0.27–0.30 V for 2 h in acidic conditions. All the other OECs exhibited a dramatic increase in the overpotential after just a few minutes, which is indicative of instability. The activity of other OECs, such as PdO_2[64], Pt[60], Mn_2O_3[76], and CoO[77] has also been demonstrated in various studies, although their long-term stability have not yet been established.

2.5 Strategies to Enhance the Electron Mobility

In order to address the poor electron mobility of $BiVO_4$ as a photoanode in a PEC water splitting system, several strategies have been performed to improve the intrinsic photocurrent density of this material. The $BiVO_4$ photoanode has been altered using different strategies in order to improve its surface properties, enhance the electron transport mobility, and ultimately reduce the undesired electron-hole recombination. The most successful of these strategies are described in this section.

2.5.1 Morphology Control

Effect of Porosity and the Synthesis Procedure

Bare porous $BiVO_4$[56] and bare nanoporous $BiVO_4$[35] films have been synthesized via an electrodeposition procedure of the Bi precursor followed by drop-casting of the vanadium precursor. They have yielded photocurrent densities of 1.1 mA/cm^2 and 1.8 mA/cm^2 at 1.23 V vs. RHE, respectively. It was reported that apart from contributing a higher surface area, the porosity of the material increases the volume of the depletion layer in the semiconductor and improves the electron-hole separation[56]. The improvements in photocurrent densities reaching1.7 mA/cm^2 and 4.2 mA/cm^2 (at 1.23 V vs. RHE), respectively, have been reported for each of these materials after the addition of a FeOOH OEC to the bare porous $BiVO_4$, and of an FeOOH/NiOOH OEC to the bare nanoporous $BiVO_4$.

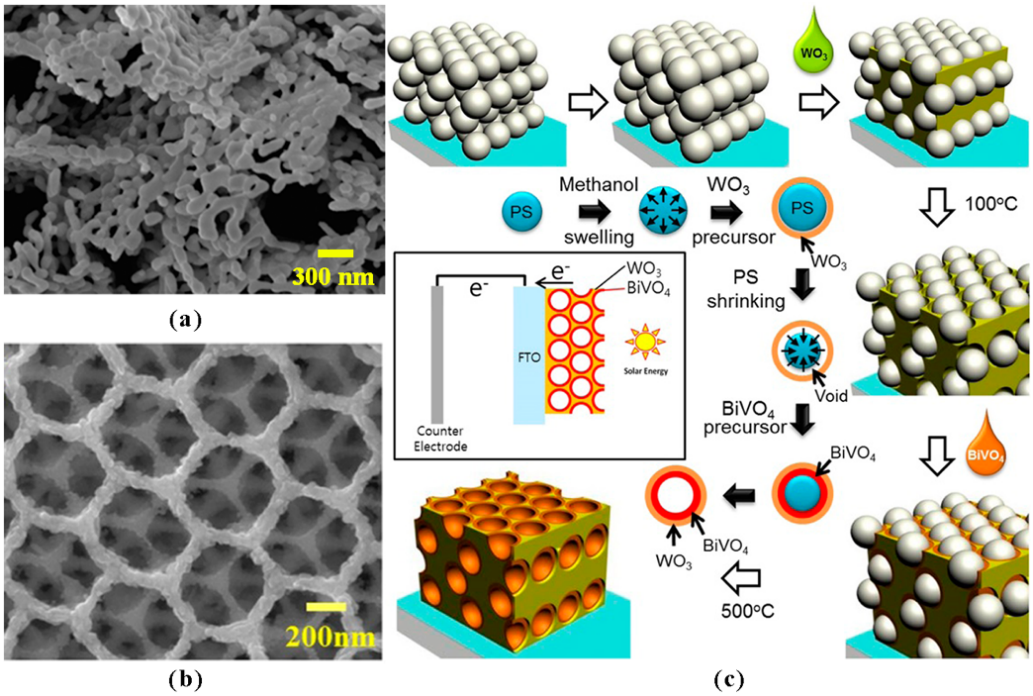

Figure 3. Morphology enhancement techniques for $BiVO_4$ synthesis. (a) Field emission scanning electron microscopy (FE-SEM) image of porous $BiVO_4$ on FTO that the authors synthesized using the electrodeposition route suggested by Kim & Choi[35]. (b) SEM image and(**c**) schematic diagram of the synthesis of double-deck inverse opal $WO_3/BiVO_4$ synthesized by Ma et al., adapted with permission from [78], Copyright American Chemical Society, 2014.

Figure 3a shows the FE-SEM image of porous $BiVO_4$ that was synthesized using the electrodeposition route of Kim and Choi[35]. An increased porosity was achieved through the cathodic electrodeposition of BiOI, which served as the bismuth precursor, on a F-doped Tin Oxide (FTO) conductive surface. The thin 2D structure of BiOI gave rise to a porous $BiVO_4$ structure upon calcination, after heat treatment while in contact with the vanadium precursor.

In another study by Hernández *et al*[79], dense and porous $BiVO_4$ photoanodes were synthesized using spin-coating. The photocurrent density that was achieved by the dense electrode reached up to 3 mA/cm^2 at 1.23 V vs. RHE, when enhanced by a Co-Pi OEC. Electrochemical impedance spectroscopy (EIS) measurements showed that the charge transfer kinetics in the dense $BiVO_4$ was 3-fold faster than that obtained from the porous film. On the other hand, the porous film was found to have a higher resistance to charge transfer across the electrode–electrolyte interface, thereby causing the electrons to accumulate in the conduction band, and eventually recombining with the holes in the valence band. However, the authors stated that the presence of defective states that were induced by the synthesis procedure may have caused the higher charge recombination in this particular porous photoanode. Indeed, as seen from a different study, the synthesis of porous $BiVO_4$ via double magnetron sputtering generated a photocurrent density of 1.2 mA/cm^2 at 1.23 V vs. RHE[80], which is 4-fold greater than the pristine $BiVO_4$ that was produced via spin-coating. It is very important to understand from here that the nature of the synthesis procedure and the manner by which it is performed heavily affect the intrinsic properties of a material, and ultimately, determines its performance.

There are different characteristics that are induced by the synthesis processes that have been identified as essential to achieve a high performance on pristine $BiVO_4$[79]. First, the crystallite size was found to have a direct correlation to the O_2 production activity of $BiVO_4$ samples[81], i.e., doubling the size of the $BiVO_4$ crystals, from 90 to 170 nm has increased the rate of O_2 evolution 5-fold. Second, the preferential orientation towards the (040) facets as well as the (001) facets have both been reported to have a positive influence on the water oxidation photoactivity of scheelite monoclinic $BiVO_4$[54,81]. In addition, the higher the distortion of the VO_4^{3-} tetrahedron and the lower the V–O distance, the higher is the mobility of the charge carriers in the material, and therefore the more the charge recombination is suppressed. Finally, a reduced concentration of defects at the grain boundaries of crystals sintered together, which can be achieved by controlling the crystallization, i.e., thermal treatment steps during the synthesis process, is able to diminish the superficial recombination[79,82].

Effect of Ordered Structures/Inverse Opals

Another method of altering the $BiVO_4$ morphology involves the fabrication of compact, ordered structures called inverse opals, which provide an ordered transport path for the electrons in order to enhance the electron mobility. For the preparation of inverse opals, well-ordered polystyrene (PS) spheres that are arranged in crystal templates, are placed on the substrates and are infiltrated with the $BiVO_4$ precursor solution. The PS templates are removed by annealing, and this yields inverse opal structured-catalysts. Zhou *et al*[52] were able to produce pristine BiVO4 with a photocurrent density of 0.6 mA/cm^2 at 1.23 V vs. RHE, using this technique. Doping with 2 atom % Mo increased the photocurrent density to 1.1 mA/cm^2 at 1.23 V vs. RHE.

Ma *et al*[78], produced a double-deck heterojunction structure of WO_3 and $BiVO_4$ with an inverse opal nanostructure, which generated a high photocurrent density of 3.3 mA/cm^2 at 1.23 V vs. RHE, without the aid of a dopant or an OEC. Figure 3b shows the FE-SEM image of this photoanode which clearly shows the ordered pattern. It was achieved through the use of monodisperse PS scaffold films that had been swollen with a methanol solvent, and infiltrated with a WO_3 precursor solution, as shown in Figure 3c. The authors were able to induce the growth of $BiVO_4$ in a controlled manner, thus resulting to its even distribution over the WO_3 skeleton.

2.5.2 Addition of *n*-Type Conductivity Dopants

Doping $BiVO_4$ with Mo and W has been performed extensively[83–91]. W and Mo are characterized to be shallow electron donors and their primary effect is increasing the charge carrier density, which then increases the electron mobility by increasing the n-type conductivity of the $BiVO_4$[92]. This phenomenon as well as the superior n-type conductivity that was induced by Mo doping than by W doping, has been demonstrated through first-principle density functional theory (DFT) calculations[84] and experiments[44,86].

Moreover, Thalluri *et al*[93] have identified the role of the amounts of W and Mo dopants for the water oxidation reaction. They determined that charge carrier separation is enhanced on the surface of $BiVO_4$ for up to a certain amount of dopants: 0.9 at.% of W or 1.2 at.% of Mo, for which the electron-hole recombination is reduced and the $BiVO_4$ photocatalytic activity is improved.

In a study by Pattengale *et al*[94], it was reported that the W dopant replaces the V site, causing the bulk structure to change to a mixture of monoclinic and tetragonal scheelite $BiVO_4$ structures. The Bi center is less distorted than the undoped $BiVO_4$. These structural changes are thought to eliminate hole traps, and therefore extend the electron lifetime.

Park *et al*[66] reported that 3 at.% Mo doping on the V site almost doubled the absorbed photon-to-current efficiency (APCE), and it also enhanced the photocurrent density of $BiVO_4$, from between 0.1 and 0.2 mA/cm^2 at 1.23 V vs. RHE, to a final photocurrent density of about 1.0 mA/cm^2 at 1.23 V vs. RHE. After addition of a FeOOH OEC, the photocurrent density increased further to 3 mA/cm^2 at 1.23 V vs. RHE.

Abdi *et al*[26] utilized a gradient-doping technique on $BiVO_4$ using 0 %–1 % of W. This was reported to enhance the charge separation 1.6-fold. The improvement was due to the induced band bending, which generates a desirable built-in electric field. The photocurrent density of gradient-doped W reached 1.1 mA/cm^2 at 1.23 V vs. RHE. Adding a Co-Pi OEC was found to further enhance the photocurrent density to reach 3.6 mA/cm^2 at 1.23 V vs. RHE.

Gong *et al*[95] reported an increase of up to 2.6-fold in photocurrent density when they performed 10 at.% doping of Mo on bare 150 nm-thick $BiVO_4$ that had been produced by magnetron co-sputtering, and reached a photocurrent density of 1.2 mA/cm^2 at 1.23 V vs. RHE.

Doping with PO_4 oxoanion was reported to increase the activity by 30-fold, and the improvement was attributed to the improved charge transfer in the semiconductor-electrolyte interface, as shown by EIS analyses[86].

Tae Woo Kim *et al*[48] have performed N-doping on nanoporous $BiVO_4$ and, using a FeOOH/NiOOH OEC in series, they were able to reach a remarkable photocurrent density value of 5 mA/cm^2 at 1.23 V vs. RHE, versus the 4 mA/cm^2 at 1.23 V vs. RHE that was obtained without N-doping. IPCE values were 50 % and 60 % at 400 and 470 nm, respectively, at 0.6 V vs. RHE. Nitrogen was reported to enhance the light absorption and charge transport, due to a further lowering of the band gap energy, which gives access to a wider range of the solar spectrum. This was achieved by elevating the VBM, decreasing the static dielectric constant, and improving the electron mobility.

Jin Hyun Kim *et al*[96] produced a dual-doped $BiVO_4$ photoanode, which was accomplished through a H-treatment and the use of 3 at.% Mo. This generated a photocurrent density of about 3 mA/cm^2 at 1.23 V vs. RHE. The H_2 treatment and Mo-doping was reported to increase the charge carrier density significantly, i.e. 2 orders of magnitude, due to the formation of intrinsic and extrinsic defects. Doping was also found to extend the diffusion length of the holes. The addition of a Co-Ci OEC further increased the photocurrent density to 4.9 mA/cm^2 at 1.23 V vs. RHE.

Monfort *et al*[97] used 10 at.% of Nb to enhance the photoelectrochemical performance of $BiVO_4$. The photocurrent density was improved from about 0.5 mA/cm^2 at 1.23 V vs. RHE to about 2 mA/cm^2 at 1.23 V vs. RHE in a $NaHCO_3$

electrolyte. The enhanced activity was attributed to the formation of a hierarchical nanostructure, which favoured the charge separation.

2.5.3 Heterojunction Formation

The charge recombination in $BiVO_4$ can be attributed to the short carrier diffusion length of approximately 70–100 nm[38], and the charge recombination happening as a consequence. The use of a heterojunction[98–100], formed by using an underlayer made up of a more conductive core material that will enhance the electron mobility, has been investigated to solve this problem.

In a study by Ma *et al*[78] (Figure 3b-c), WO_3 inverse opals were used as the core structure and were reported to have better electron transporting properties than the $BiVO_4$ shell, generating a photocurrent density of 3.3 mA/cm^2 at 1.23 V vs. RHE. Similarly, a conducting inverse opal network, made from an Al-doped ZnO, was utilized by Zhang *et al*[101] as an electron collector, and it resulted to a photocurrent density of 1.5 mA/cm^2 at 1.23 V vs. RHE.

Pilli *et* al[102] fabricated a $CuWO_4/BiVO_4$ heterojunction through the electrodeposition of the $CuWO_4$ on FTO, and the spray deposition of a highly porous $BiVO_4$ film on the electrodeposited surface. The photocurrent density was improved 1.8-fold, which reached about 1.6 mA/cm^2 and IPCE of 42 % at 420 nm measured at 1.23 V vs. RHE, was attributed to the enhanced charge collection efficiency. Furthermore, the heterojunction was reported to have caused a shift in the onset potential of up to 0.23 V, when a $NaHCO_3$ electrolyte was used.

A core-shell $WO_3/BiVO_4$ helix nanostructure that was doped with Mo and naturally doped with W from the WO_3 core was synthesized by Shi *et al*[60]. This produced a photocurrent density of 3.6 mA/cm^2 at 1.23 V vs. RHE. The addition of an FeOOH/NiOOH co-catalyst yielded a remarkable photocurrent density of 5.35 mA/cm^2, and an IPCE of 90 % between 330 and 450 nm at 1.23 V vs. RHE. Shi *et al* stated that the nanohelix structure improved the light absorption, because of the resulting light scattering, and it also promoted charge separation by introducing a complex distribution of the electric field.

In a separate work, Shi *et al*[103]synthesized a mesoporous WO_3 bottom layer that was spin-coated with a Mo-doped $BiVO_4$ on the top. Natural doping of the W on the WO_3 layer occurred at the $BiVO_4$ due to intimate contact during heat treatment. The photocurrent density generated was about 3 mA/cm^2 at 1.23 V vs. RHE, while a further addition of the FeOOH/NiOOH OEC increased the photocurrent density to a value of 4 mA/cm^2 at 1.23 V vs. RHE.

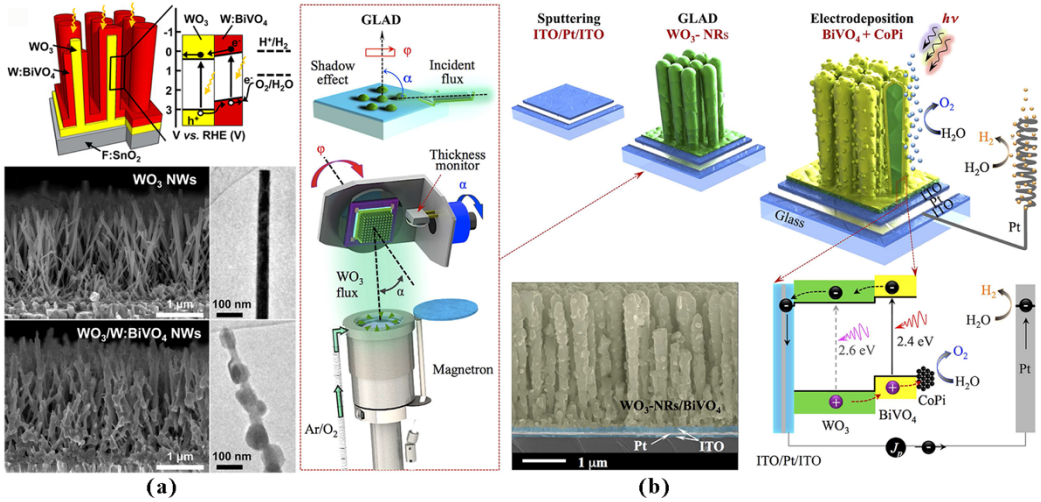

Figure 4. (**a**) $WO_3/BiVO_4$ core-shell nanowires (NWs) according to Rao et al[104]and (**b**) $WO_3/BiVO_4$ core-shell nanorods (NRs) by Pihosh et al[57]. Image (a) reprinted/adapted with permission from [104], Copyright American Chemical Society, 2014. Image (b) used under the Creative Commons CC-BY license attributed to[57]. Copyright Nature Publishing Group, 2015.

Rao *et al*[104] fabricated a $WO_3/BiVO_4$ core-shell nanowire photoanode, synthesized using combination of flame vapor deposition and drop-casting techniques, as illustrated in Figure 4a. A photocurrent density of 3.1 mA/cm^2 at 1.23 V vs. RHE was obtained. The W:$BiVO_4$ shell that they synthesized was only 60 nm thick, which is less than the 70–100 nm hole diffusion length reported in literature. Because of this, hole/electron charges separation was enhanced because the holes were readily able to reach the semiconductor/electrolyte interface. Furthermore, they reported that the axial electron conductivity of the WO_3 nanowire core was higher than that of the $BiVO_4$ film, thus, the preferential flow of the photogenerated electrons was radially inward to the WO_3 cores.

The highest photocurrent density recorded to date is for the CoPi-coated $WO_3/BiVO_4$ core-shell nanorods shown in

Figure 4b. It was synthesized by Pihosh *et al*[57], which yielded a photocurrent density of 6.72 mA/cm^2 at 1.23 V vs. RHE. This corresponds to about 90% of the maximum theoretical photocurrent density of $BiVO_4$. An IPCE of 80–90 % was achieved for wavelengths ranging from 400–500 nm at 1 V vs. RHE. The WO_3 nanorods were grown using GLAD, the $BiVO_4$ was synthesized via electrodeposition, and the Co-Pi OEC was added via a photo-assisted electrodeposition technique. The key improvement in $BiVO_4$ performance has been attributed to the use of an extremely thin absorber (ETA) heterojunction structure to address the problem concerning the short carrier diffusion length. This minimizes the electron-hole recombination. In addition, Pihosh *et al* reported that the ETA structure also enhanced the photon absorption, because of a more efficient light scattering.

2.5.4 Use of Passivation Layers

Solid semiconductors such as $BiVO_4$ have surface states that are associated with the abrupt termination and discontinuity of the solid crystal at the crystal boundary, with an electronic band structure that is quite different from the bulk, and characterized by dangling bonds[5]. These surface states having a modified band structure may give rise to defect levels, which are energy levels that do not lie near the band gap edges and may lie within the previously forbidden band gap region. These can mediate electron-hole recombination via the Shockley-Read-Hall mechanism wherein the electron from the conduction band can move towards the defect level, release the energy as photon or phonons, and eventually relax in the valence band, annihilating a hole in the process.

Surface recombination can be reduced in two ways: (1) reducing the rate by which the surface states can capture electrons and holes by reducing the number of the said surface states or having lesser capture probabilities, and (2) reducing the number of one type of charge carrier that is available in the surface[5,105]. The former can be achieved via chemical passivation, where the dangling bonds are completed using a surface dielectric coating or chemical species such as Hydrogen. The former is accomplished either via field-effect passivation, in which an internal electric field is responsible for modifying the surface carrier concentration, or via introduction of dopants with high concentration of a certain carrier type in the surface.

In photoelectrochemical systems, passivation layers have been used as an effective strategy to improve the charge separation and transfer processes across semiconductor–liquid interfaces. These thin layers can reduce the charge recombination at surface states, increase the water oxidation reaction kinetics, and protect the semiconductor from chemical corrosion. These layers are <100 nm thick but quite often, only 1–2 nm are used to allow the charge transfer by means of tunneling. Passivation layers can be fabricated by means of several relatively scalable techniques such as atomic layer deposition (ALD), spin-coating, electrochemical deposition, sputtering, electron beam evaporation, floating transfer and dip-casting [7,24,106].

$BiVO_4$ surface passivation with Al_2O_3

Al_2O_3 is a wide band gap material (5-9 eV) having different crystalline forms, exhibiting low leakage current, and a modest value of dielectric constant[107]. It finds its use as a gate dielectric in metal oxide semiconductor (MOS) transistors and is a suitable insulator for various electronic applications.

In the solar photovoltaic field, the importance and crucial impact of surface recombination to the resulting photoactivity of conventional semiconductors has been very much highlighted. Al_2O_3 has been used as a passivation layer for both p- and n-type silicon solar cells. Al_2O_3as a passivation layer is unique because it

combines the effect of both chemical and field effect passivation by providing hydrogen to the Si interface during the post-deposition thermal treatments and also for having a very high density of negative charges located near the interface[108].

However, literature is scarce for the use of Al_2O_3as a passivation layer for $BiVO_4$ photoanodes. To date, only two papers reported the use of Al_2O_3 as a passivation layer for $BiVO_4$[109,110]. It was shown that adding an Al_2O_3 layer with an optimal thickness enhances the photocurrent density, however, the nature of the specific surface interactions between Al_2O_3 and $BiVO_4$ remains to be studied.

$BiVO_4$ surface passivation with TiO_2

TiO_2 is the most studied semiconductor oxide since its photoactivity was reported in 1972. However, it possesses a band gap of 3.2 eV, thus, inefficient for sun-driven reactions, if used bare. TiO_2 has also been used in the photovoltaic field as an antireflective passivating layer. Charge trapping of valence band electrons in defects near the valence band of TiO_2 have been demonstrated and also found to increase the conductivity. It was hypothesized that illuminating TiO_2 negatively charges it by exciting an electron into the conduction band, while simultaneously, the corresponding valence band hole is filled by reacting with silicon or the outside ambient[111].

In order to overcome the degradation of $BiVO_4$ under extreme pH conditions, TiO_2 has been used to passivate the material, mainly as a protection coating. A thin layer of amorphous TiO_2 (80–120 nm thick deposited for 15–30 s)[85], resulted to a 5.5-fold increase in photocurrent density as well as a shift in the photocurrent onset potential by -0.5 V. The authors explained that the enhancement was in part due to the TiO_2 layer passivating the FTO surface, which was not completely covered by the W-doped $BiVO_4$. This reduced the back-reduction of the photo-oxidized intermediates on the conducting substrate and passivated the defect sites on the surface of the W-doped $BiVO_4$ films. The authors also noted that a possible improvement in charge collection, may be due to band bending at the TiO_2–$BiVO_4$ interface.

Ultrathin dual layers of TiO_2 and Ni have also been used to stabilize polycrystalline $BiVO_4$ photoanodes against photocorrosion in an aqueous alkaline (pH = 13) electrolyte[112]. The dual-layer coating extended the lifetime of the $BiVO_4$ photoanodes during photoelectrochemical water oxidation from minutes, for the bare $BiVO_4$, to hours, for the modified electrodes. $ZnFe_2O_4$ (10-15 nm thick) has also been used as a protection layer to stabilize $BiVO_4$ in a 0.1 M KOH solution[87], which generated a photocurrent density that was >2 mA/cm^2 at 1.23 V versus RHE, with a significantly improved stability, compared to the pristine $BiVO_4$ electrode. It was also suggested that the $ZnFe_2O_4$ protection layer could also contribute to photocurrent generation via an increased photon absorption and electron–hole separation.

It is worth noting that, although significant advantages are possible with a surface passivation layer, other problems may arise. The surface layer creates new interfaces that need to be considered. While a surface layer can improve one property, it may simultaneously make another property worse. However, the engineering of multiple component passivation layers can provide a solution for the many material problems encountered in PEC water splitting.

2.5.5 Substrate Modification

Since the performance of the $BiVO_4$ photoanode is hindered to a great extent by the short hole diffusion length, which is a very evident phenomenon when dealing with flat substrates, efforts have been made to alter the conductive substrate surface by 3D nano-structuring to compensate for this limitation. A few studies have recently reported the 3D structuration of the conductive substrate of the $BiVO_4$ photoanode. However, it should be noted that expensive materials, such as Au and Pt, were used in these techniques to enhance the conductivity of the engineered substrates.

Zhao *et al*[113], for instance, deposited the $BiVO_4$ onto textured polydimethylsiloxane (PDMS) substrates, which were fabricated via a water-assisted transfer printing method. This was done to take advantage of the enhanced light absorption, via a dual light-trapping strategy, and of the enhanced surface reactions due to surface roughness. An Au film was deposited onto the SiO_2/Si wafer, via electron beam deposition, to serve as an electron back collector and light reflector. Thin SnO_2 and $BiVO_4$ films were then spin-coated onto this surface. A pristine 80 nm thick $BiVO_4$ photoanode was synthesized, and it exhibited a photocurrent density of 1.37 mA/cm^2, which increased to approximately 2 mA/cm^2 at 1.23 V vs. RHE when enhanced by an FeOOH OEC.

Another example is the work of Qiu *et al*[59], who reported the synthesis of $BiVO_4$ photoanode on an engineered nanocone substrate, which is shown in Figure 5. Engineered substrate structures, such as the nanocone, have the advantage of depositing thicker materials that can bring about a more efficient charge separation. The cone nanostructure was prepared by means of reactive-ion etching of SiO_2, while its conductivity was enhanced via magnetron sputtering of Pt. A SnO_2 film was then applied as a blocking layer by ultrasonic spray pyrolysis to reduce back e^- recombination. Finally, $BiVO_4$ was formed via a sol-gel process, and the generated photocurrent density was 4.18 mA/cm^2 at 1.23 V vs. RHE.

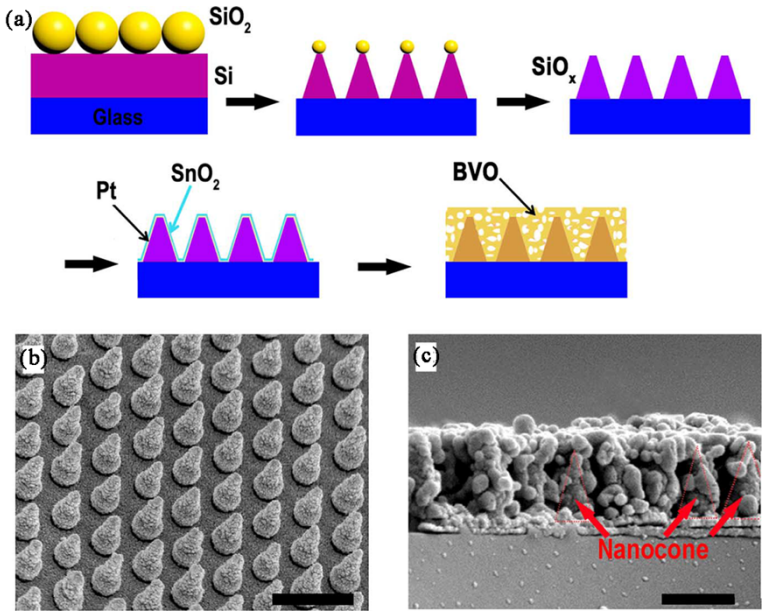

Figure 5. Pt/SnO_2/Mo:$BiVO_4$ on an engineered nanocone substrate. (a) Schematic illustration of the fabrication process of the conductive nanocone substrate; (b) scanning electron microscope (SEM) image (60° tilting) of the final SiOx/Pt/SnO_2 nanocone arrays; (c) cross-sectional SEM images of Mo:$BiVO_4$ on the SiOx/Pt/SnO_2 nanocone substrate. Some exposed nanocones were also marked in the figure (c). Scale bars, 500 nm. Images adapted and used under Creative Commons CC-BY-NC license, attributed to [59] . Reprinted with permission of from [59]. Copyright American Association for the Advancement of Science, 2016.

Substrate modification strategy is a key element in the design of photoanodes in a real PEC water splitting device. The development of transparent, conductive, porous, and robust substrates, for use as supports for photoelectroactive materials, remains a challenge.

2.6 What are the gaps?

2.6.1 Need to focus on scalable synthesis techniques

The $BiVO_4$ photoanodes can be prepared via a couple of techniques. One route is through the synthesis of $BiVO_4$ powder via solid-state synthesis or solution-based techniques such as hydrothermal synthesis or sol-gel synthesis. An extensive amount of literature covers the powder synthesis techniques employed in producing $BiVO_4$. Then, the synthesized powders are deposited on conductive electrodes via spin-coating, dip-coating or the very simple doctor-blade technique. These are simple techniques that can be easily implemented at cheaper cost. However, $BiVO_4$ powders synthesized by these methods usually suffer from very low surface area[56,114], typically having values which are less than 10 m^2/g. Uniformity in the photoanode films produced by this method is also an issue for scaling up these methods. Meanwhile, direct $BiVO_4$ thin films have been prepared by employing different deposition techniques.

There are physical vapor deposition processes like molecular beam epitaxy and magnetron sputtering[80], which offer uniformity over large areas, a better control on stoichiometry, and ease of scalability[115], but may require highly specialized and crystalline substrates as well as need high power and high vacuum (at least 10^{-6} Pa) requirements which might not be compatible with the more low-cost glass substrates normally used[11]. Chemical vapor deposition processes to deposit $BiVO_4$ offer highly crystalline and high quality thin films, with ample control on morphology via controlling the process conditions[116], but it uses relatively high temperature in order to evaporate the precursors.

Among the various thin film deposition techniques, the most promising in terms of scalability and ease of execution is electrodeposition. Although the technique is limited to the deposition of electrically-conductive materials, it is very much suited for producing polycrystalline films of $BiVO_4$ with favorable porosity and well-developed nanostructured materials. Because it is essentially a solution-based technique, the control of morphology can be accomplished by just varying the different solution parameters while the thickness control can be accomplished via controlling the electrodeposition parameters, all done under ambient conditions, thus, relatively cheap and practical. However, the literature for electrodeposited $BiVO_4$ is not exhaustive. Despite its promise, it is not very well-studied and thus, it is a very good field to explore.

2.6.2 Need to probe $BiVO_4$ surface chemistry/interactions

The nature of the surface of the photocatalyst plays a major role in its performance. There have been varying opinions about the role of surface states or defects on the $BiVO_4$ photoanodes in their photoelectrochemical water splitting activity, with some studies claiming that they are beneficial by promoting charge transport and collection[117] by directly impacting the electronic structure of the $BiVO_4$, while some others are faulting them as providing harmful trap sites that cater to electron-hole recombination[118].

The dominant intrinsic defects in the monoclinic scheelite $BiVO_4$ are the oxygen vacancies, which can be found both in the bulk and the surface, characteristically being more pronounced in the surface. Oxygen vacancies at oxide surfaces such as that of $BiVO_4$ can alter the geometric and chemical structures and properties of the electrode[119], and in turn, impact its activity to a large extent. A very good understanding of the fundamental contributions of these surface defects to the overall activity of the photoanode is crucial in determining the extent of the functionality. This has not yet been clearly elucidated and much work needs to be done for the role of these oxygen vacancies in the use of $BiVO_4$ photoanodes in PEC water splitting.

In addition, while there are many studies dedicated to the improvement of $BiVO_4$ photocatalytic performance by aiming for a higher current density, the

nature of the surface of pristine $BiVO_4$ and its interactions have not been comprehensively studied. This is of utmost significance in order to determine what kind of surface phenomenon will prevail, and will give insights about how the surface species are interacting with other elements, i.e., a passivation layer or an OEC overlayer.

2.6.3 Need for stability improvement

In order to be practical, PEC water splitting systems have to be stable for a long period of time, the typical benchmark being a lifetime of 10 years[120]. However, achieving such a lifetime still remains a challenge as scientists are still trying to overcome the effect of the strong reductive and oxidative properties of the photogenerated electron-hole pair on the stability of semiconductor electrodes.

Toma *et al*[121] performed a mechanistic study on the chemical and photochemical transformations of $BiVO_4$ photoanodes in which insights are given about issues concerning the source of instability in $BiVO_4$ photoanodes. In this study, it was shown that the degradation of the $BiVO_4$ photoanodes takes place under all aqueous testing conditions and was seen to be accelerated by illumination, as well as by increase of the pH and of the applied anodic bias. This phenomenon was prevalently attributed to the following: (1) an inability to achieve self-passivation, brought about by the inability to form a stable Bi-O surface phase, due to kinetic limitations on the room-temperature structural transformation of V-deprived degradation product; and (2) an accumulation of holes on the surface of the lattice, which were observed to cause the $BiVO_4$ destabilization.

The longest stability test that was performed on a $BiVO_4$-based photoanode was done on WO_3/(W,Mo):$BiVO_4$ helix nanostructures[60] with FeOOH/NiOOH, which only lasted for 7 days, accompanied by a corresponding 8.7% decay on its performance. Evidently, the 10-year stability target is still far from being achieved as current research trends are still focusing on solving the problem of inefficiency.

Chapter 3

Bare $BiVO_4$ electrodes: synthesis, characterization, and photoactivity

This chapter discusses the synthesis, characterization, and the photoactivity of pristine $BiVO_4$ photoanodes that were synthesized via the electrodeposition of the Bi precursor and subsequent drop-casting of the V precursor. It reports the findings on the effect of the electrodeposition time, the calcination temperature, and the composition of the electrodeposition solution on the photocurrent density and material properties. This chapter provides a comprehensive discussion about how the different material properties are correlated to the photoactivity, and how the studied factors impact these parameters. Moreover, more insights are presented considering the various photoelectrochemical characterization techniques.

3.1 Materials and Methods

3.1.1 Materials

Bismuth (III) nitrate pentahydrate ($Bi(NO_3)_3 \bullet 5H_2O$, ≥98%), vanadyl acetylacetonate ($VO(acac)_2$, ≥98%), potassium iodide (KI, ≥99%), p-benzoquinone ($C_6H_4(=O)_2$, ≥98%), absolute ethanol (CH_3CH_2OH, ETOH,≥99.8%), dimethyl sulfoxide/DMSO ($(CH_3)_2SO$, ≥99.9%), nitric acid (HNO_3,70%) and sodium hydroxide (NaOH pellets, ≥97%), were utilized as-received from Sigma-Aldrich. Fluorine-doped tin oxide (FTO) conductive glasses with a sheet resistance of 7 Ω/cm^2 were obtained from Solaronix Inc. The FTO glasses were cleaned by sonicating in acetone, ethanol and water, respectively, for 10 minutes each, prior to their use.

3.1.2 Investigation and optimization of $BiVO_4$ synthesis

The $BiVO_4$ synthesis procedure was based on a method employed by Kim and

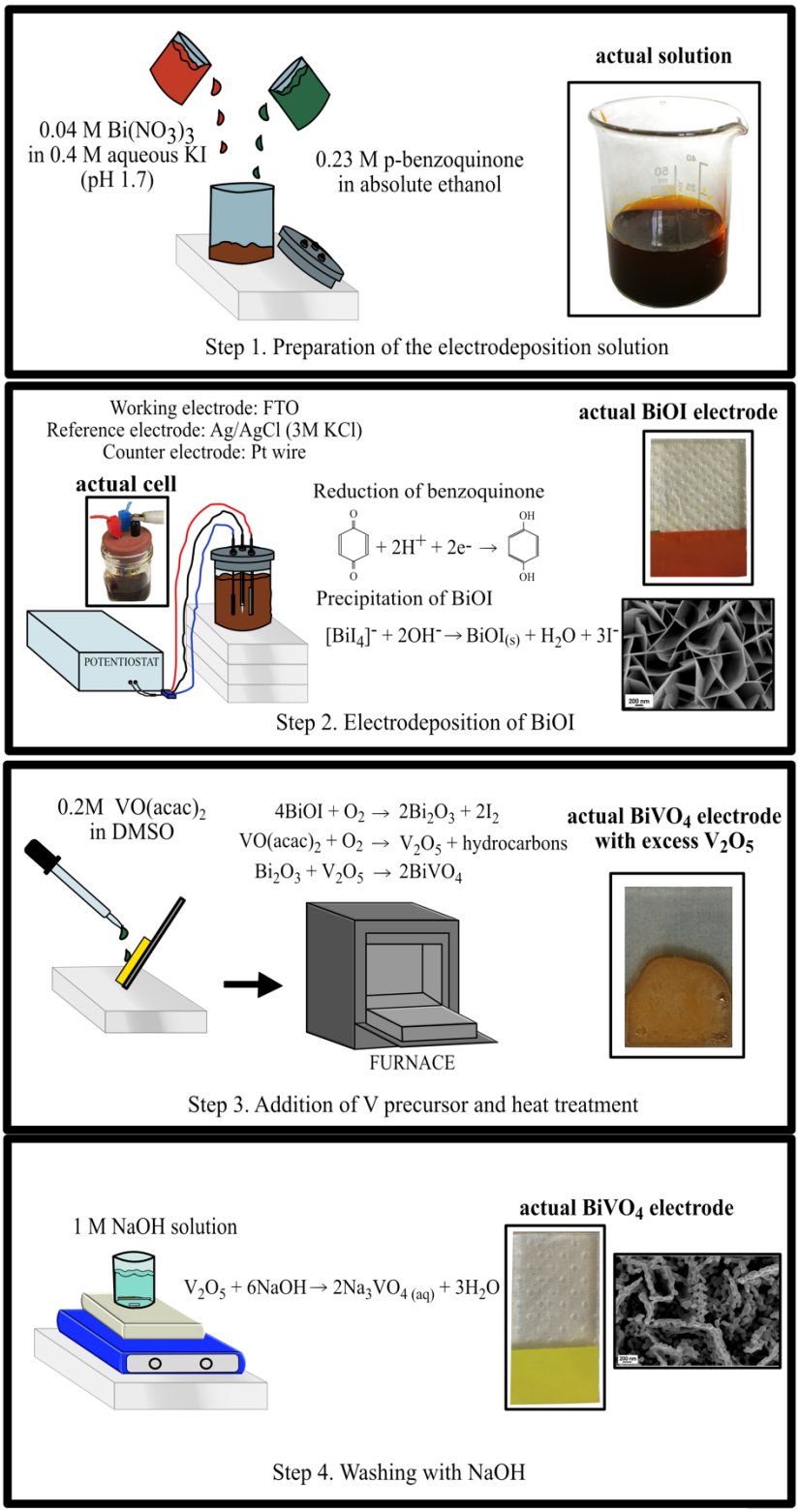

Figure 6. Synthesis of pristine $BiVO_4$

Choi[35], which involves the electrodeposition of BiOI on FTO as the first step. The whole procedure is outlined in Figure 6, which also shows the actual solutions and electrodes that were obtained. The electrodeposition solution was prepared by

mixing 0.04 M of $Bi(NO_3)_3 \bullet 5H_2O$ dissolved in acidified 0.4 M KI aqueous solution (pH 1.7), with 0.23 M p-benzoquinone in absolute ethanol (Step 1). For this, potentiostatic cathodic deposition was performed by using a 3-electrode system. An FTO glass served as the working electrode, Ag/AgCl (3 M KCl) served as the reference electrode, and a Pt wire was used as the counter electrode to close the circuit. Different voltages (from -0.05 V to -2 V) and electrodeposition times (from 0.5 min to 10 min) were investigated (Step 2). The geometric area was kept constant at 2 cm^2. The film thickness was obtained using a profilometer by tracing the surface topography of the samples.

After the deposition of BiOI, Vanadium was introduced on the BiOI film by a dropwise addition of 180 μL of a 0.2 M vanadyl acetylacetonate solution. Two different solvents were investigated for the dissolution of the V-precursor: dimethyl sulfoxide (DMSO) and dimethyl fluoride (DMF).

In order to induce the formation of crystalline $BiVO_4$, the samples were calcined by using different ramping rates, a slow rate (2 ^oC/min) and a fast one (20 ^oC/min), and at various temperatures from 350 ^oC to 500 ^oC (Step 3).The calcined FTOs were then gently stirred in 1 M NaOH solution for 30 minutes to dissolve the excess V_2O_5 (Step 4). Finally, pristine $BiVO_4$ electrodes were obtained after washing the electrodes with ultrapure H_2O.

Table 4. Important factors that were optimized using the experimental design

Factor	**Levels**		**Fixed factor**		
	Min	**Max**	**Electro-deposition time (min)**	**Calcination temperature (^oC)**	**Bi-KI to benzoquinone-EtOH ratio**
Electrodeposition time (min)	0.5	10	---	425	1.9
Calcination temperature (^oC)	350	500	5.25	---	1.9
Bi-KI to benzoquinone-EtOH ratio	1.3	2.5	5.25	425	---

Preliminary factor screening tests (details shown in Appendix 1) were performed in order to identify the factors that have the most influence to the photoactivity. The effects of each identified factor (indicated in Table 4) and their different levels on the photoactivity have been thoroughly investigated.

Furthermore, the identified factors (indicated in Table 4) were then optimized using the central composite design of experiments (CCDE) by utilizing the photocurrent density as the response variable. Each factor was varied across 5 levels in the experiment. The experimental runs have been performed in a randomized order, employing the design principles of replication, randomization and blocking.

A 6-point replication of the center points of the experimental design have been performed.

3.1.3 $BiVO_4$ thin film characterization

A Merlin Zeiss Field Emission – Scanning Electron Microscope (FE-SEM) equipped with an Energy Dispersive X-ray Spectroscopy System (EDS) was used to study the morphology of the samples.

XRD spectra were obtained by using a Panalytical X'Pert PRO diffractometer under Cu Kα radiation (λ =1.5418 Å) set at 40 kV and 40 mA, in order to determine the crystallinity of the $BiVO_4$ films. Crystallite sizes were calculated by using the Scherrer formula $D = k\lambda / \beta \cos\theta$, where D is the average crystallite size (nm), λ is the wavelength of the X-ray radiation (0.15418 nm), k is the shape factor (0.90) and β is the full-width half maximum, which was corrected for instrumental broadening. Calculations were done in the Panalytical High Score software by referencing the profile width of the samples to the one of the LaB_6 employed as standard, whose pattern was collected in the same optical and acquisition conditions of the samples. The calculation was done after fitting a Pseudo-Voigt profile function into the measured data.

UV-vis absorption spectra were obtained by using a Varian Cary 5000 spectrophotometer in the diffuse reflectance mode with an integrating sphere. Optical band gap energies were calculated by using the Tauc relation $\alpha h\nu = A(h\nu - E_g)^n$, where α is the absorption coefficient, A is a constant that is related to the mass of electrons and holes, E_g is the band gap energy, and the value of n depends on the type of transition (n=1/2 for allowed direct transition and 2 for allowed indirect transition). The majority of the literature suggests that $BiVO_4$ follows an allowed direct transition. In this work, the band gap of the $BiVO_4$ films was calculated by using the equation $\alpha h\nu^2 = A(h\nu - E_g)$, through a plot of $\alpha h\nu^2$ *vs* hν, which has a linear region having a slope A and the extrapolation of $\alpha h\nu = 0$ gives the direct E_g. The band gap calculations using indirect band gap transition were also performed and the results obtained were almost equivalent to the direct band gap transition calculations.

X-ray photoelectron spectroscopy (XPS) measurements were performed by using a PHI 5000 Versa probe instrument equipped with a monochromatic X-ray source of 1486.6 eV (Al Kα) in order to determine the surface composition of the synthesized electrodes. High resolution (HR) analysis has been performed with a pass energy of 23 eV, with a double charge compensation made by Ar^+ and electron beam sources. The deconvolution procedure has been completed by using Multipak 9.0 dedicated software. C 1s core level has been used as referenced at 284.5 eV. Pseudo-Voigt function has been applied for curve fitting the experimental data, while Shirley function has been used to subtract the background signal.

3.1.4 Photoelectrochemical tests

A 3-electrode system with a Pt coil counter electrode (CE), Ag/AgCl (3M KCl) reference electrode (RE), and the synthesized $BiVO_4$ photoanode as the working electrode (WE), were set up in a single-compartment quartz cell containing a 0.1 M phosphate buffer solution at pH 7. To simulate sunlight irradiation, a Newport 450 W Xe lamp with an AM 1.5G filter was employed, using an intensity of 100 mW/cm^2 for all the tests. The entire electrode geometric area of 2 cm^2 was illuminated.

PEC activity tests were performed by using a BioLogic VSP 300 potentiostat. In order to characterize the photocatalytic activity of the $BiVO_4$ photoanodes, linear sweep voltammetry (LSV) in continuous and chopped light modes, and chronoamperometry (CA), were employed. The LSV curves show the behaviour of the photocurrent density as a function of the applied potential in the PEC system, while the CA curves show the behaviour of photocurrent density over time at a fixed voltage, which was 0.61 V vs Ag/AgCl (1.23 V vs RHE) in this case. Linear sweep voltammetry was performed at the potential range of -0.3 to 1 V *vs.* Ag/AgCl at a scan rate of 10 mV/s. Chronoamperometry was done at 0.61V *vs.* Ag/AgCl. For the conversion of the measured potentials versus the Ag/AgCl (3M KCl) reference electrode to RHE (NHE at pH=0), the following Nernst equation was used.

$$E_{RHE} = E_{\frac{Ag}{AgCl}} + 0.059pH + E^{o}_{\frac{Ag}{AgCl}} \left(E^{o}_{\frac{Ag}{AgCl}} = +0.199\,V \right) \qquad (1)$$

In order to examine the carrier mobility and the photocatalytic potential of the $BiVO_4$ films, staircase potentio electrochemical impedance spectroscopy (SPEIS) was performed for each sample, using the potential range of -0.8 to 1 V (*vs.* Ag/AgCl),and a frequency of 7.5 kHz with an amplitude of 25 mV. Thus, Mott-Schottky plots were drawn to extrapolate the flat band potentials (E_{fb}) and donor densities (N_D) of the photoanodes, according to the equation:

$$\frac{1}{C^2} = \frac{2}{\varepsilon\varepsilon_o A^2 e N_D}\left(E - E_{fb} - \frac{k_B T}{e}\right) \qquad (2)$$

where C is the interfacial capacitance, ε is the dielectric constant of the semiconductor, ε_o is the permittivity of free space, A is the area of the interfacial capacitance, N_D is the donor density, E is the applied potential, E_{fb} is the flat-band potential, k_B is the Boltzmann's constant, T is the temperature and e is the electronic charge. A plot of $\frac{1}{C^2}A^2$ versus the potential yields a linear region. From the value of this slope, the N_D of a semiconductor can be calculated and the intercept of the extrapolation of this linear plot to $\frac{1}{C^2}A^2 = 0$ gives its flat band potential. A positive slope indicates that the material is an n-type semiconductor and electrons are the majority charge carriers.

Charge transport and transfer properties of the photoanodes were investigated using electrochemical impedance spectroscopy (EIS) measurements, in the frequencies ranging from 0.1 Hz to 0.5 MHz, at 0.61 V *vs.* Ag/AgCl, under simulated sunlight illumination (100 mW/cm^2).

3.2 Results and Discussion

3.2.1 Effect of various factors on physico-chemical properties

In this section, the effect of the various electrodeposition factors on the morphology, physico-chemical properties, and charge carrier mobility of the $BiVO_4$ electrodes is presented. The FESEM and XRD images of $BiVO_4$ films prepared under different conditions as reported in Table 4 are shown in Figure 7 and Figure 8, respectively.

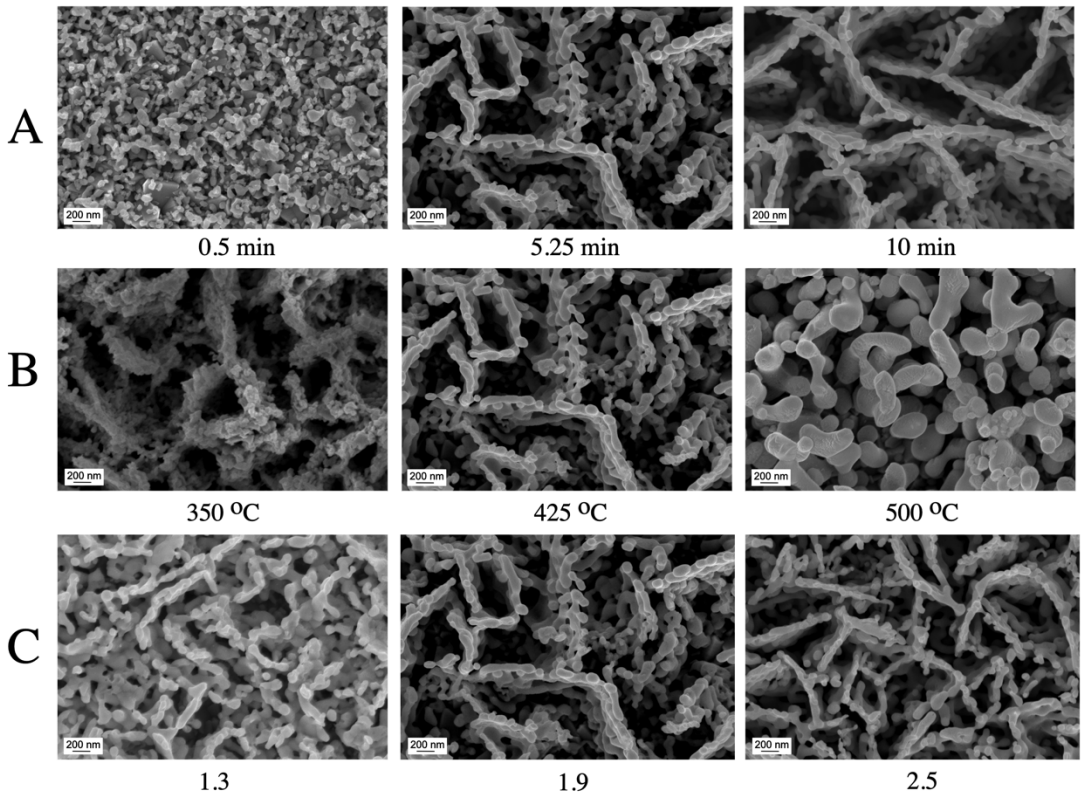

Figure 7. FESEM images of the bare $BiVO_4$ photoanodes synthesized at different: (A) electrodeposition times, (B) calcination temperatures, and (C) Bi-KI to Benzoquinone-EtOH ratio, as detailed in Table 4.

From the FE-SEM images in Figure 7, there were very pronounced changes in morphology that can be clearly observed resulting from the different synthesis conditions that were employed. Porous structures with varying grain sizes, agglomeration, and growth patterns can be seen. The specific effects of each factor variation are extensively discussed in the following factor-specific sections.

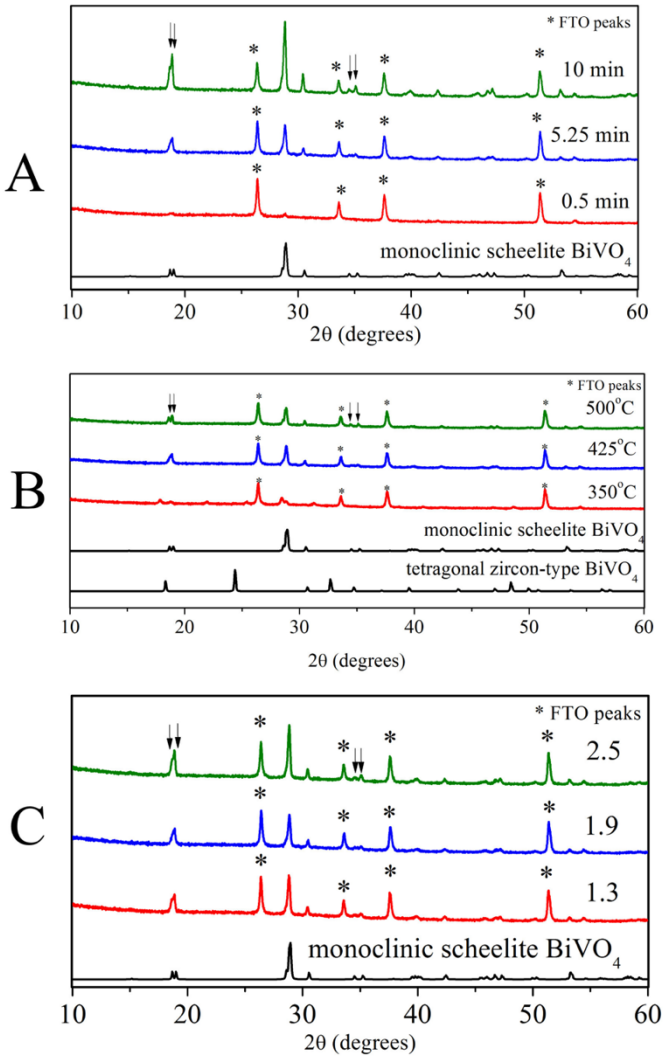

Figure 8. XRD spectra of the bare $BiVO_4$ photoanodes synthesized at different: (a) electrodeposition times, (b) calcination temperatures, and (c) Bi-KI to Benzoquin one-EtOH ratio, as specified in Table 4.

From the XRD spectra shown in Figure 8, it can be seen that the monoclinic scheelite structure (JCPDS No. 14-0688, space group: I2/a, a=5.195, b=11.701, c=5.092, β=90.38°) was obtained for almost all the electrodes, which is evident from the peak splitting at the 18.5° and 35° of 2θ (see arrows in the figure). The only exception was the 0.5 min sample that is the thinnest electrode, which manifested a spectra that is practically similar to that of the FTO, because of the very low amount of $BiVO_4$ that was deposited on it. The thickness of this electrode is 56 nm.

The physico-chemical properties of the synthesized $BiVO_4$ electrodes have been summarized in Figure 9 for every factor, in order to evaluate their effects on

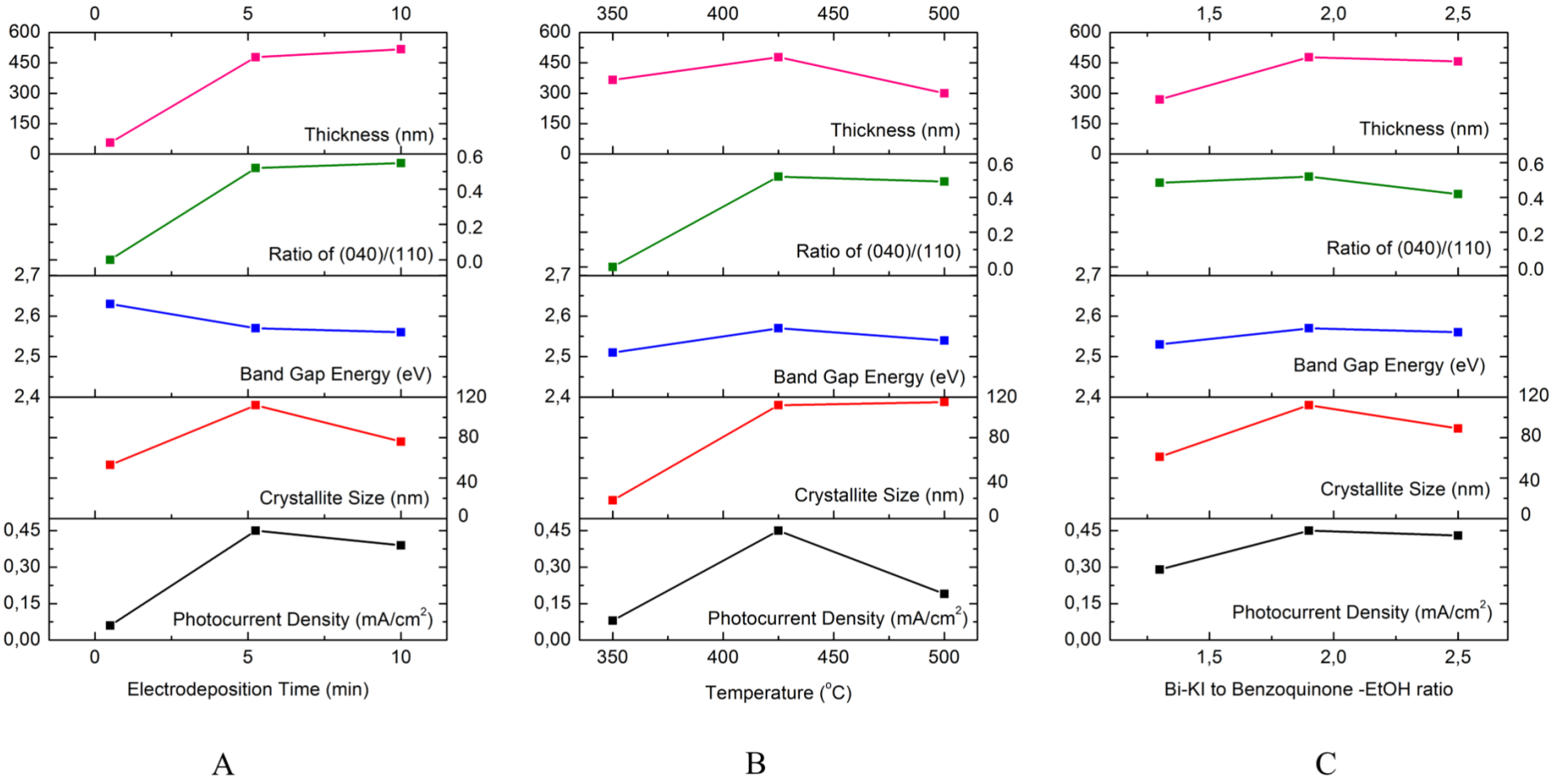

Figure 9. Summary of physico-chemical properties at various (A) electrodeposition time, (B) calcination temperature, and (C) Bi-KI to benzoquinone-EtOH ratio, plotted with respect to the photocurrent density at 1.23 V vs RHE

the resulting photocurrent density. A more detailed analysis of this figure is given in the succeeding subsections while the following sentences describe the information contained therein, in general. The mean crystallite sizes (calculated from data on (011), (121) and (040) facets), and the ratio between the crystal facets (040) and (110) were calculated from the XRD data. The photocatalytic activity of $BiVO_4$ powders have previously been reported to be directly proportional to the exposure of the (040) facet, which is assumed to provide a multi-atomic BiV_4 center that makes the electron transfer more facile. Hence, the normalized XRD intensity peak parameter, (040)/(110) ratio, was used to compare the XRD intensities, using the (110) peak used as an internal standard. Moreover, optical band gap energies were calculated from the UV-vis diffuse reflectance spectra by using the Kubelka-Munk function and the Tauc relation for a direct band gap semiconductor, as it was done in previous literature reports, and in agreement with the behavior of all of the $BiVO_4$ thin films that were synthesized in this study. Please refer to Appendix 2 for these plots. From these data, it can be seen that the band gap energy calculations yielded values ranging from 2.51 to 2.63 eV, signifying absorption in the visible light range. The corresponding thicknesses of the films that were obtained using a profilometer are also presented in Figure 9.

The high resolution XPS spectra for Bi 4f, V 2p, and O 1s binding energy regions that were obtained for all the samples at various synthesis conditions are shown in Figure 10. All of the samples manifest the spin-orbit splitting for both the Bi $4f_{7/2}$ and Bi $4f_{5/2}$, and the V $2p_{3/2}$ and V $2p_{1/2}$, that are in good agreement with those reported in literature for $BiVO_4$[122]. It is noteworthy that the Bi $4f_{7/2}$ and Bi $4f_{5/2}$ peaks appear in the binding energy region (158.5 eV and 163.8 eV, respectively) that is much higher than that of metallic Bi, *i.e.* 156.8 eV and 162.2 eV[122], respectively. These Bi 4f peaks indicate the presence of Bi occurring mainly as Bi^{3+}species in the surface of the electrodes. Meanwhile, the V $2p_{3/2}$ and V $2p_{1/2}$ peaks at 516.1 eV and 523.7eV, respectively, are characteristic of V occurring as V^{4+} species on the surface of the photoanode. This is different from the bulk V species, which have V^{5+} oxidation state. Quite interestingly, this is a demonstration of the surface reduction of V from V^{5+} to V^{4+} as reported by Rossell *et al*[123], which was attributed to the presence of intrinsic surface defects in the form of oxygen vacancies that directly impact the electronic structure of monoclinic scheelite $BiVO_4$. Meanwhile, a deconvolution procedure applied to the O 1s spectrum reveals that the O species are divided into oxygen due to the lattice structure, the non-lattice oxygen, and oxygen due to adsorbed molecules[122,124]. The deconvoluted O 1s peak at 529.2 eV is assigned to oxygen in a $BiVO_4$ lattice environment, while the peaks at 530.3 eV and 532.0 eV are assigned to non-lattice and adsorbed oxygen species[125], respectively. Non-lattice oxygen refers to oxygen-deficient regions, which might be populated with OH groups in order to correct the charge balance. Finally, the O 1s peak at 532.0 eV refer to chemisorbed or dissociated oxygen from the water molecules.

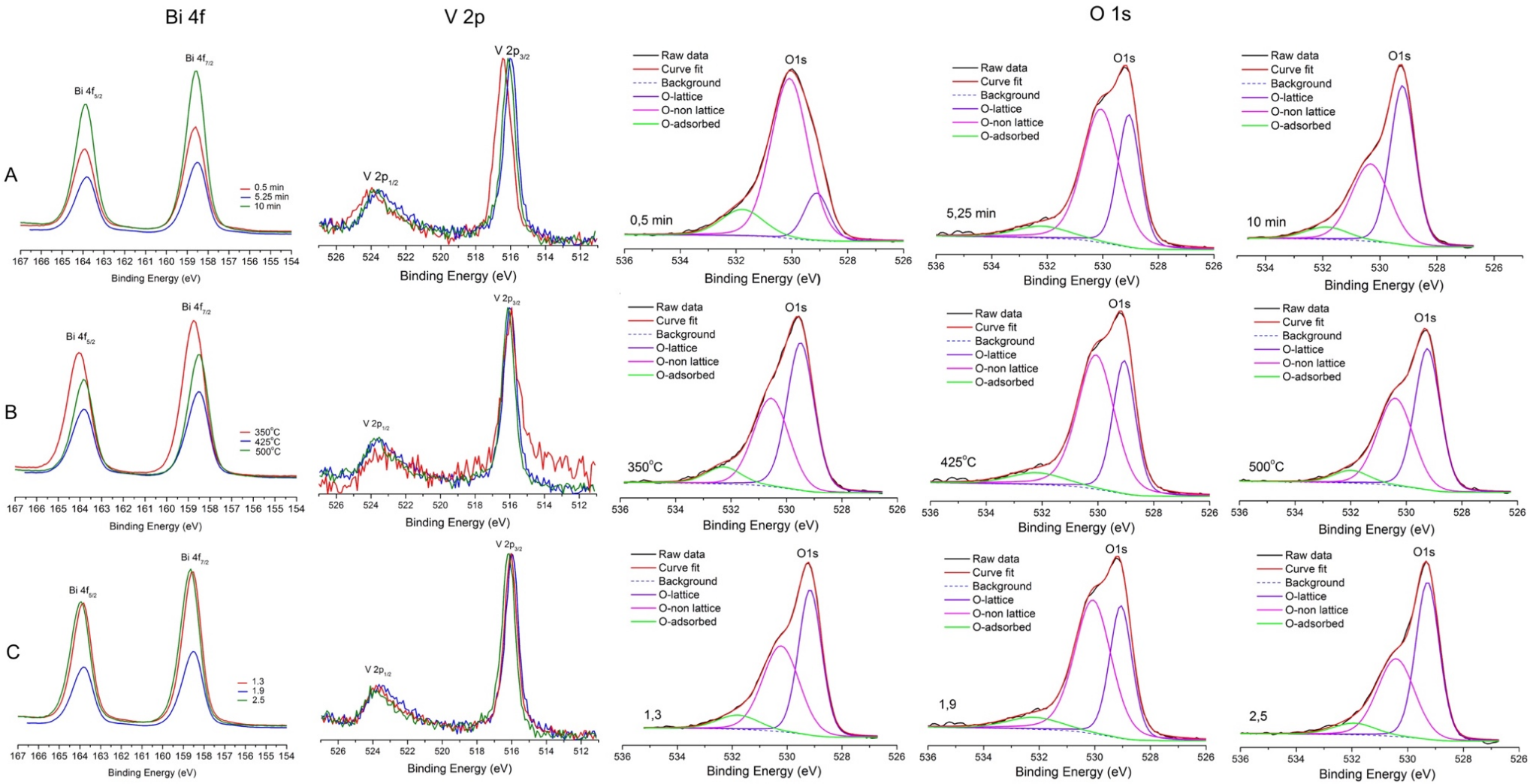

Figure 10. Bi 4f, V 2p, and O 1s XPS spectra for various (A) electrodeposition time, (B) calcination temperature, and (C) Bi-KI to benzoquinone-EtOH ratio

A proper amount of oxygen vacancies can aid in both bulk and surface charge separation[126]. The creation of oxygen vacancies bring about free electrons, which are shallow electron donors that enhance the conductivity of the semiconductor. They also enhance the interfacial charge transfer by increasing the active sites, i.e. turning the V site into an active site, and by lowering the adsorption energies of some intermediates like H_2O_{ads}, OH_{ads}, and O_{ads}, thereby promoting an easier charge transfer to the electrolyte and improving surface catalysis[126]. Meanwhile, an excessive amount of oxygen vacancies is detrimental to the photoactivity because the V^{4+} is characterized by a larger ionic radius than the V^{5+}, and what happens is that when it is excessive, this can result to lattice distortion that can subsequently reduce the hole diffusion length[127].

Surface Bi/V atomic ratios as measured using XPS and bulk Bi/V atomic ratios as measured using EDS are reported in Figure 11. As shown in Figure 11, the bulk Bi/V ratio is consistently about 1, confirming the 1:1 ratio of Bi:V atoms of $BiVO_4$. However, looking at the surface species of Bi/V tells a different story, wherein the Bi concentration tends to be higher than that of the V atoms for all the synthesized electrodes. We have found that the Bi/V ratio for an untested electrode deposited at 5.25 minutes, 425°C and 1.9 Bi-KI to benzoquinone-EtOH ratio, results to a surface Bi/V of 2.3. This Bi-rich surface, consistent with the findings of Sayama *et al*[128] could have been due to the segregation phenomenon that has been observed for different Bi-containing oxides. The depletion of O in the subsurface happens because of the segregation of O to the surface, which leads to Bi-O surface terminations as reported by Passerone *et al*[129]. This Bi-rich surface can either enhance the photoactivity by serving as a protective layer or be detrimental to it by worsening the catalytic activity of $BiVO_4$ as a water oxidation catalyst[123]. This Bi/V ratio increases to 2.96 after the photoelectrochemical tests, while that for the bulk Bi/V remains unchanged at about 1.Thus, there was also a dissolution of surface V atoms from the $BiVO_4$ surface during the photoelectrochemical tests.

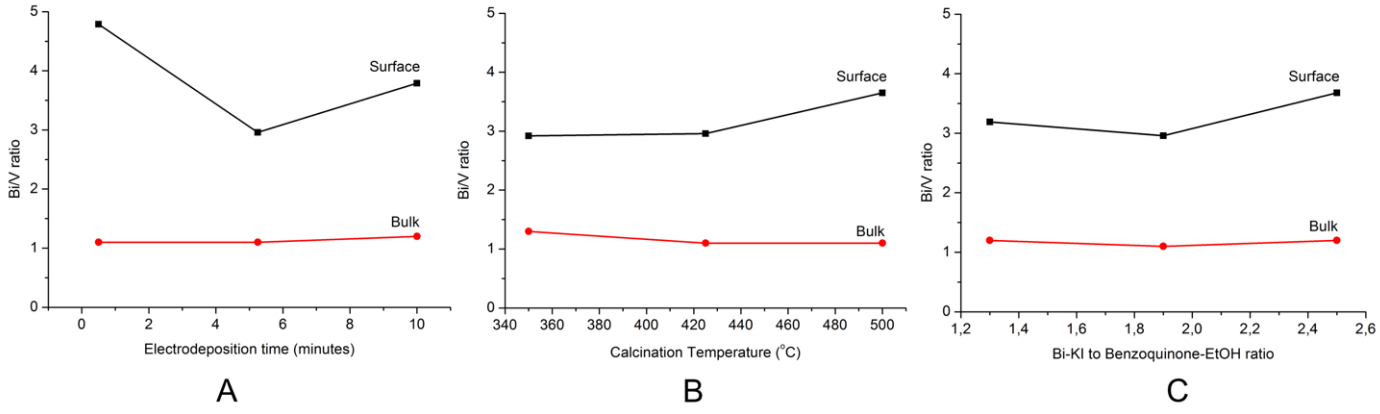

Figure 11. Surface and bulk Bi/V ratio

Effect of electrodeposition time

As expected, increasing film thicknesses were obtained by using different electrodeposition times of 0.5 minute, 5.25 minutes, and 10 minutes, at a calcination temperature of 425 ^{o}C and a Bi-KI to benzoquinone-EtOH ratio of 1.9. The obtained film thicknesses, measured by using a profilometer, were 56 nm, 478 nm and 517 nm, respectively. As seen in the FE-SEM images in Figure 7A, the $BiVO_4$ in the 0.5 min sample did not completely cover the FTO surface, whose crystals are evident. However, after 5.25 min of electrodeposition, the FTO substrate was fully covered and a nanoporous $BiVO_4$ structure was produced, which tends to maintain the nanoflake structure of the electrodeposited BiOI material (refer to Appendix 4 for the FESEM images of electrodeposited BiOI), as the electrodeposition time increases and as the film thickness grows.

Based on the XRD patterns shown on Figure 8A, the samples with the 5.25 minutes and 10 minutes electrodeposition time, yielded the monoclinic scheelite structure. Meanwhile, the 0.5 minute sample yielded an XRD spectrum that coincides with that of the FTO, which suggests that a very thin layer of $BiVO_4$ was deposited on the FTO surface. This film was the thinnest electrode, and some portions of the FTO are still visible in the FE-SEM image. In agreement with the thickness measurements, the XRD peak intensities generated for the thickest film, *i.e.* 10 minutes of electrodeposition time, are generally higher compared to the other samples, which confirms that more material has been deposited on this FTO surface. This is seen most distinctively in the 2θ peak of 29^{o}. The mean crystallite size was the highest for the 5.25 min sample (112 nm) and the lowest for the 0.5 min sample (53 nm). In addition, the 0.5 min sample has a negligible (040) peak and, therefore, almost zero value of the (040)/(110) ratio. A preferential growth of the $BiVO_4$ crystals along the (040) direction was observed by increasing the electrodeposition time.

All the samples have manifested an absorption in the visible light region (see Appendix 2). As reported in Figure 9A, the band gap energy of the sample electrodeposited for 0.5 min (2.63 eV) is higher than those of the samples prepared during 5.25 min and 10 min of electrodeposition time, which have almost equal band gap energies, *i.e.* 2.55 eV and 2.56 eV, respectively. These band gap energy values are characteristic of monoclinic scheelite $BiVO_4$[55]. Being the thinnest electrode, some part of the FTO surface have been exposed in the 0.5 min sample, which resulted to a higher band gap energy due to the FTO that has a band gap energy of about 3.3 eV[130].

Upon examination of the XPS spectra in Figure 10A, a slight shift of the binding energy for the O 1s peak of the thinnest sample (0.5 min) relative to the 5.25 and 10 min samples was observed, which could be attributed to the exposure of the FTO. Meanwhile, the deconvolution of the O 1s spectra of the 5.25 min sample showed that there were more oxygen vacancies for this sample than that of

the 10 min sample. Moreover, from the surface composition analysis as shown in Figure 11A, it was seen that the highest surface Bi/V ratio (4.79) after testing was recorded for the 0.5 min sample, while the lowest surface Bi/V ratio (2.96) was recorded for the 5.25 min sample.

By merely looking at the contribution of the physico-chemical properties of these electrodes synthesized at different electrodeposition time, it can be inferred that the increase in photocurrent density (shown in Figure 9A) was mainly brought about by a higher crystallite size (112 nm), an optimal electrode thickness (478 nm), and the lowest surface Bi/V ratio.

A higher crystallite size appears to be favourable in enhancing the photoactivity. By observing the morphology of this sample, it can be seen that there is the highest interconnection among the crystals of the 5.25 min sample and a more closed porosity, which both could have played a role in better enhancing the carrier mobility in this electrode compared to the others.

There is an optimum thickness of $BiVO_4$ electrodeposited in the electrode after 5.25 min, which is higher in the present case (about 478 nm) than the optimum value of 200 nm that was previously reported for $BiVO_4$ electrodes prepared by other techniques such as dip-coating.[40] In this study, a further increase in the electrode thickness of 36 nm by electrodeposition for 10 min has caused a reduction of 13% in the photocurrent density. It is possible that the accompanying increase in thickness has contributed to more defect levels that could have acted as charge recombination sites.

The lowest surface Bi/V ratio is favourable because a high surface Bi/V ratio brings about a higher presence of Bi-O surface terminations, which might have contributed to the lower catalytic activity of $BiVO_4$ as an oxygen evolution catalyst.

Effect of calcination temperature

The effect of the calcination temperature was investigated at 350 ^oC, 425 ^oC, and 500 ^oC, at an electrodeposition time of 5.25 minutes and a Bi-KI to benzoquinone-EtOH ratio of 1.9.

There were very pronounced differences in the morphology of the samples calcined at different temperatures, as can be seen in Figure 7B. All the $BiVO_4$ films possess a nanoporous structure, but the pores decreased in size as the crystals grew. The 350 ^oC sample showed the formation of small crystals that are agglomerated in a network that follows the shape of the pristine BiOI nanoflakes (see Appendix 4), which seem to stick to one another. As the temperature increased, the small crystals sintered together into larger crystals, achieving up to about 200 nm of length and formed the interconnected globules, which are visible in the FESEM images of the samples calcined at 500 ^oC in Figure 7B.

XRD data in Figure 8B shows that the three $BiVO_4$ samples calcined at 350°C, 425 °C, and 500 °C clearly exhibited the monoclinic scheelite structure, characterized by the subtle emergence of the 18.5 ° and 29 ° in 2θ peaks. The presence of tetragonal zircon-type phase that could be present in the samples calcined at 350 °C can be excluded due to the absence of the main peaks at 24.3° and 32.7° that are associated with this crystalline structure. The peak splitting of the characteristic peaks observed at 18.5° and 35° of 2θ was more pronounced as the calcination temperature increased, which is most likely due to an increase in the crystallinity of the monoclinic scheelite phase in the $BiVO_4$ samples. Indeed, in agreement with the FESEM images, the mean crystallite sizes calculated from the XRD data also increased by increasing the calcination temperature. However, the peak related to the (040) facet was absent in the sample calcined at 350 °C, most probably due to the small size of the crystals (*i.e.* 22 nm and 13 nm for the (011) and (121) facets, respectively). Meanwhile, by increasing the temperature, the samples grew along all directions. It is noteworthy that the samples calcined at 425 °C and 500 °C have an almost similar mean crystal size of 112 and 115 nm, respectively, while having almost the same ratios of the (040)/(110) facets, that are 0.52 and 0.49, respectively, as shown in Figure 9B.

All the samples exhibited absorption in the visible light region. The corresponding plots are shown in Appendix 2. The band gap energy obtained for the samples calcined at different temperatures did not vary significantly and ranged from 2.51 to 2.55 eV, which are slightly higher than the generally reported values of 2.4 eV for $BiVO_4$[55]. It can be stated that the photon absorption capacities of the samples did not vary too much, with a very slight advantage towards the lowest temperature of 350 °C, because of its slightly lower band gap energy value.

Based on the XPS spectra for all the samples shown in Figure 10B, the Bi species are mainly Bi^{3+} and the V species are occurring mainly as V^{4+}. From the O 1s region, it can be seen that the sample 425 °C has the highest amount of oxygen vacancies among all the samples. Moreover, as reported in Figure 11B, the surface Bi/V ratios were almost equal for the 350 (2.92) and 425 °C (2.96) samples, while it was significantly higher for the 500°C sample (3.65).

The thickness of the electrodes that were calcined at 350 °C, 425 °C, and 500 °C were 365 nm, 478 nm, and 300 nm, respectively. There is no clear trend as to how the thickness of the electrode varies with the calcination temperature, but an optimal thickness value of 478 nm can be clearly correlated to the resulting photocurrent density.

When the crystallite sizes, band gap energy and the (040)/(110) ratio are almost the same, such as in the case of the 425°C and 500°C samples, the main parameters that distinguish whether which electrode is going to be more photoactive than the other are the thickness and the morphology. The electrode needs to be thick enough to enhance the absorption of the photons but at the same time, it needs to be thin

enough to avoid the formation of excessive defect levels that can act as charge recombination sites. A perfect compromise between these two properties is the ideal condition. Lastly, as observed from the FESEM images, the further growth of $BiVO_4$ crystals could cause less interconnected surface of the $BiVO_4$ crystals, and the exposure of free FTO substrate, which could possibly induce a lower rate of electron flow and collection, and a higher rate of charge (e^-/h^+) recombination.

Effect of Bi-KI to Benzoquinone-Ethanol Ratio

The effect of varying the Bi-KI to benzoquinone-ethanol ratio was also investigated by using the ratios of 1.3, 1.9, and 2.5, at a calcination temperature of 425 ^oC and an electrodeposition time of 5.25 minutes. As seen in Figure 7C, this parameter significantly affected the morphology of the synthesized $BiVO_4$ thin films. Although all the samples that were synthesized at these conditions yielded nanoporous structures, it can be seen that there were defined globules formed at the ratio of 1.3, which exhibited a high agglomeration and closure of most of the porosity. The samples 1.9 and 2.5 ratios have morphologies that are quite similar, both showing a higher degree of porosity than the one prepared with a ratio of 1.3.

Based on the XRD patterns shown in Figure 8C, all the samples that were prepared with different Bi-KI to benzoquinone-EtOH ratio possessed the monoclinic scheelite structure. The highest crystallite size was obtained for the 1.9 ratio sample (112 nm) while the lowest one was obtained for the 1.3 ratio sample. Comparing the (040)/(110) facet ratio, it can be seen that the 1.9 sample exhibited the highest ratio, while the 2.5 sample has the least.

In addition, all the samples exhibited absorption in the visible light region. The band gap energy values that were obtained for the samples did not vary significantly and ranged between 2.53 to 2.56 eV, suggesting that there were no significant differences in the photon absorption capacity of the synthesized samples.

Based on the XPS spectra for all the samples shown in Figure 10C, all the Bi species are mainly Bi^{3+}, and the V species are occurring mainly as V^{4+}. The O 1s deconvolution spectra showed that the amount of oxygen vacancies were quite comparable for all the three samples. Meanwhile, the surface Bi/V ratios as reported in Figure 11C was the lowest for the 1.9 sample (2.96), and the highest for the 2.5 sample (3.68).

The electrode thickness measurements for the 1.3, 1.9, and 2.5 ratio samples are 269 nm, 478 nm, and 457 nm, respectively. The thickness of the 1.9 and 2.5 ratio samples just differ by 21 nm, but they are much higher than that of the 1.3 ratio.

As shown in Figure 9C, the photocurrent density for the 1.9 and 2.5 ratio samples were practically the same at 0.45 mA/cm^2 and 0.43 mA/cm^2 at 1.23 V vs

RHE, respectively. Both electrodes possess almost similar morphologies, thicknesses, and band gap energies.

3.2.2 Effect of various factors on photoelectrochemical characteristics

This section summarizes the effect of varying the electrodeposition time, calcination temperature and the Bi-KI to benzoquinone-EtOH ratio, to the resulting photoelectrochemical characteristics of the electrodes. Linear sweep voltammetry (LSV), chronoamperometry (CA), and electrochemical impedance spectroscopy (EIS) data are reported in the following subsections.

Effect of electrodeposition time

The highest photocurrent density was obtained for the sample that was electrodeposited for 5.25 minutes, calcined at 425 ^{o}C, and synthesized at a Bi-KI to benzoquinone-EtOH ratio of 1.9. It resulted to a photocurrent density of 0.45 mA/cm^2 at 1.23 V *vs.* RHE (blue line), as reported in the LSV plot in Figure 12A.

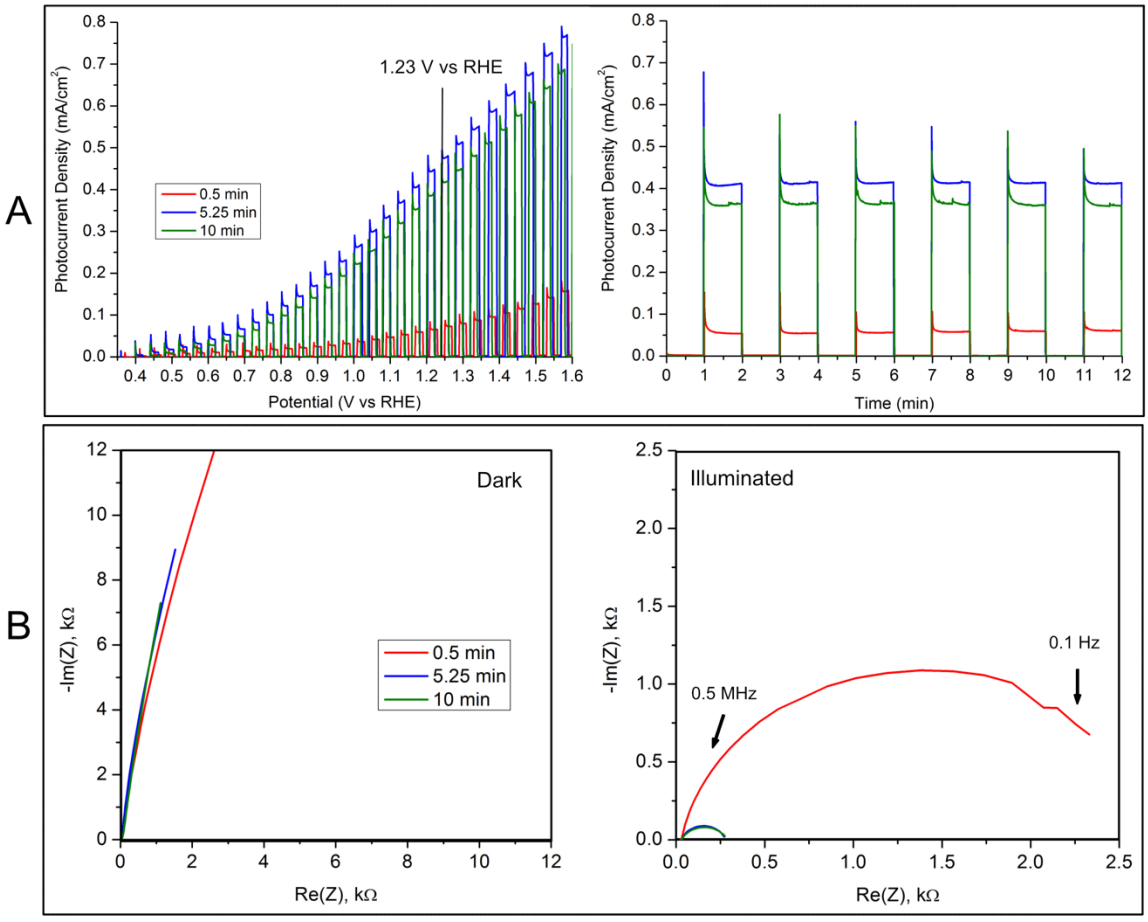

Figure 12. Photoelectrochemical characterization of samples at various electrodeposition time, at calcination temperature of 425^{o}C and Bi-KI to benzoquinone-EtOH ratio of 1.9. (RED: 0.5 min, BLUE: 5.25 min, GREEN: 10 min). (A) linear sweep voltammograms (electrolyte: 0.1 M Na-Pi pH 7, scan rate: 10 mV/s), and chronoamperometry plots (electrolyte: 0.1 M Na-Pi pH 7, potential: 1.23 V vs RHE), (B) Nyquist plots under dark and illuminated conditions.

The least photocurrent density was for the 0.5 minute sample (red line) having a photocurrent density of 0.06 mA/cm^2 at 1.23 V *vs.* RHE, while the 10 minute

sample generated a photocurrent density of 0.39 mA/cm^2 at 1.23 V *vs.* RHE (green line).

All the LSV curves were acquired by using chopped light measurements and they showed evidences of fast recombination of the photogenerated electron-hole pairs, characterized by the instantaneous dampening of the photocurrent density signal right after the light is turned on. The same is also evident in the CA plots displayed in Figure 12A. From the same plots, relatively stable mean photocurrent density values were obtained over the course of the measurement time of 12 minutes.

Electrochemical impedance spectroscopy (EIS) is a powerful technique that was used to gain insights about the charge transfer resistance. The charge transfer resistance (R_{ct}) is generally associated with the interfacial charge transfer rate of the photoelectrochemical reaction[131]. The EIS results in this study are reported using Nyquist plots, herein characterized by a single arc. The diameter of the arc in the Nyquist plot is proportional to the charge transfer resistance between the electrode-electrolyte interface.

The symmetric Nyquist plots in both the dark and illuminated conditions are shown in Figure 12B. From this, it can be clearly seen by looking at the diameter of the Nyquist plot that the worst-performing photoanode (0.5 min sample) has the highest charge transfer resistance, while the corresponding charge transfer resistances for the 5.25 min and 10 min samples are much smaller and equal. This explains the lowest photocurrent density of the 0.5 min sample, however, the charge transfer resistances of the 5.25 min sample and the 10 min sample are equal.

The specific Mott-Schottky plots are presented in Appendix 3. These information indicate the mobility of the majority carriers in the $BiVO_4$ samples and demonstrate their n-type behavior as indicated by the positive slope of the linear data. The donor density increased from the 0.5 min ($N_D = 2.35 \times 10^{19}$ cm^{-3}) to the 5.25 min ($N_D = 4.66 \times 10^{19}$ cm^{-3}) but then decreased at 10 min ($N_D = 3.00 \times 10^{19}$ cm^{-3}) of electrodeposition time. The higher N_D could have played a role in improving the photoelectrochemical response due to two main reasons.[47] First, it raises the Fermi level, creating more band bending in the space-charge region because of the bigger difference between the Fermi level and the redox potential of the electrolyte. Because of band bending, the electric field in the space charge layer is enhanced and this lowers the electron-hole recombination. Second, it enhances the electrical conductivity of the photoanode, thus, improving the charge transport properties within the material.

In addition, the onset potential of each electrode was determined to be 0.37, 0.36, and 0.40 V vs RHE for 0.5 min, 5.25 min, and 10 min samples, respectively. The 5.25 min sample has the least onset potential, closely followed by the 0.5 min

sample. A lower onset potential is important because it gives way to a practical implementation of the device to be achieved at a lower bias.

In conclusion, the highest photocurrent density of the 5.25 min sample can be attributed to the following photoelectrochemical characteristics: lowest charge transfer resistance, highest donor density, and lowest onset potential. Moreover, despite having equal charge transfer resistances and almost equal onset potentials, what differentiated the photoactivity of the 5.25 min sample from the 10 min sample was its higher donor density and the influence of the physico-chemical properties like higher crystallite size, optimal electrode thickness, and a lower surface Bi/V ratio, as earlier reported in the preceding section.

Effect of calcination temperature

Among the samples calcined at different temperatures, using 5.25 minutes of electrodeposition time and 1.9 Bi-KI to benzoquinone-EtOH ratio, the least photocurrent density was obtained for the 350°C sample (red line), which generated a very low photocurrent of 0.08 mA/cm^2 at 1.23 V *vs.* RHE, as shown in the LSV

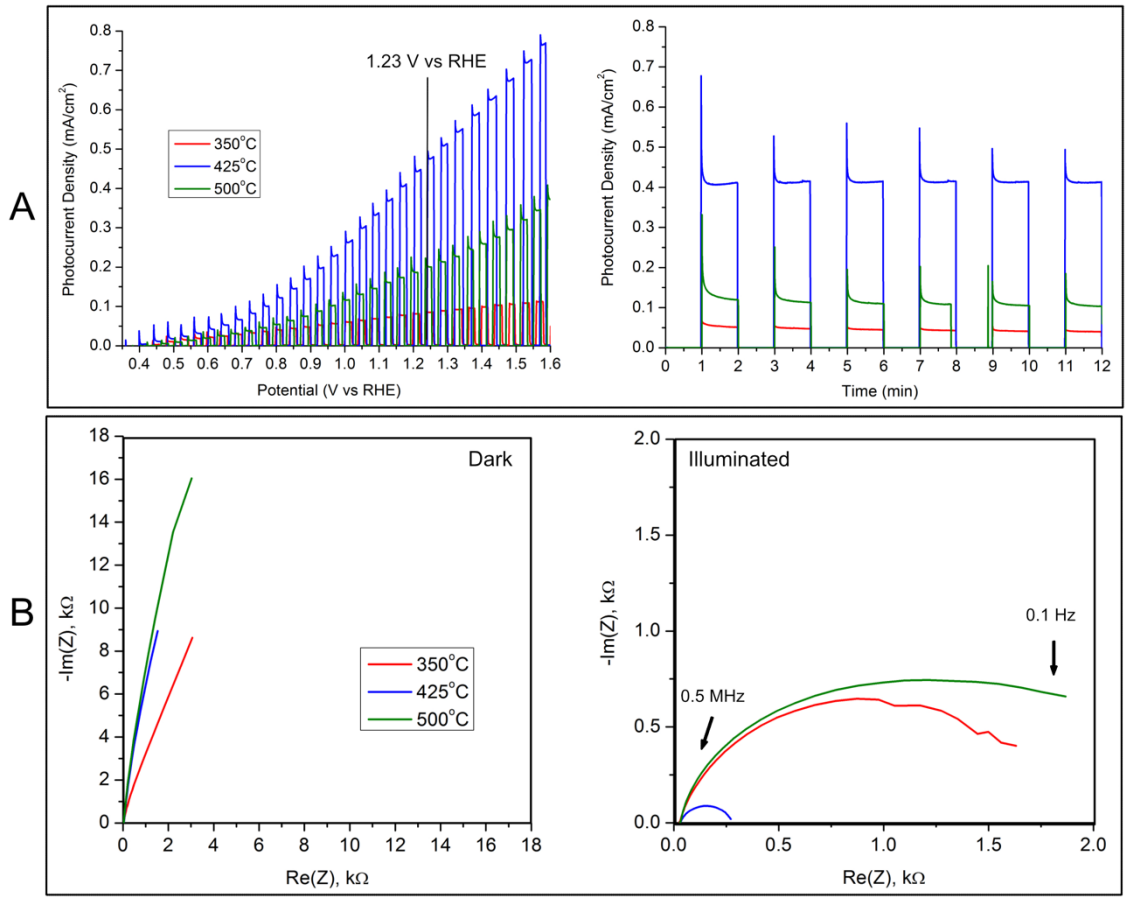

Figure 13. Photoelectrochemical characterization of samples at various calcination temperatures, at electrodeposition time of 5.25 min and Bi-KI to benzoquinone-EtOH ratio of 1.9. (RED: 350°C, BLUE: 425 °C, GREEN: 500 °C). (A) linear sweep voltammograms (electrolyte: 0.1 M Na-Pi pH 7, scan rate: 10 mV/s), and chronoamperometry plots (electrolyte: 0.1 M Na-Pi pH 7, potential: 1.23 V vs RHE), (B) Nyquist plots under dark and illuminated conditions.

plot in Figure 13A. Meanwhile, the 500 °C sample (green line) demonstrated a

photocurrent density of 0.19 mA/cm^2 at 1.23 V *vs.* RHE, which was 58 % higher than that of the 350 ^{o}C sample, but only 42 % of the maximum value achieved by the sample calcined at 425 ^{o}C (blue line).

The symmetric dark and illuminated Nyquist plots are shown in Figure 13B. The photoanode with the highest photocurrent density (425 ^{o}C sample) is clearly shown to have the lowest R_{ct}, indicated by the blue line in the illuminated Nyquist plot in Figure 13B. Meanwhile, the R_{ct} of the 350 ^{o}C sample (red line) is less than that of the 500 ^{o}C sample (green line).

From the Mott-Schottky plots shown in Appendix 3, the donor density values were obtained and were found to increase from 3.39 x 10^{19} cm^{-3} to 4.66 x 10^{19} cm^{-3} when the calcination temperature was increased from 350^{o}C to 425^{o}C. However, the calcination at 500^{o}C decreased the N_D value to 3.82 x 10^{19} cm^{-3}.

The onset potential for the 350 ^{o}C, 425 ^{o}C, and 500 ^{o}C samples are 0.44, 0.36, and 0.38 V vs RHE, respectively. The lowest onset potential obtained was for the 425 ^{o}C sample.

In conclusion, the highest photocurrent density of the 425 ^{o}C sample is attributed to the following photoelectrochemical characteristics: least charge transfer resistance, highest donor density, and lowest onset potential. Meanwhile, despite having a slightly higher charge transfer resistance and a lower thickness, the 500 ^{o}C sample exhibited a higher photocurrent density than the 350 ^{o}C sample, mainly due to the effect of the lower onset potential, higher donor density, and the presence of the (040) facet, as indicated in the preceding section.

Effect of Bi-KI to benzoquinone-EtOH ratio

Among the calcined samples made with different Bi-KI to benzoquinone-EtOH ratio using 425 ^{o}C calcination temperature and 5.25 minutes of electrodeposition time, the least photocurrent density was observed for the 1.3 ratio sample (0.29 mA/cm^2 at 1.23 V *vs.* RHE). The 2.5 ratio sample yielded a photocurrent density of 0.43 mA/cm^2 at 1.23 V *vs.* RHE, as reported in Figure 14A. The 1.3 ratio electrode performed 36 % lower than the best electrode while the 2.5 ratio electrode has a performance that is almost equal to that of the 1.9 ratio.

The symmetric dark and illuminated Nyquist plots are shown in Figure 14B. The worst-performing electrode which is that having 1.3 ratio (red line) showed the highest charge transfer resistance (R_{ct}) while the 2.5 ratio sample (green line) and the 1.9 ratio sample (blue line) showed almost similar values, with a slightly lower charge transfer resistance for the 2.5 ratio sample.

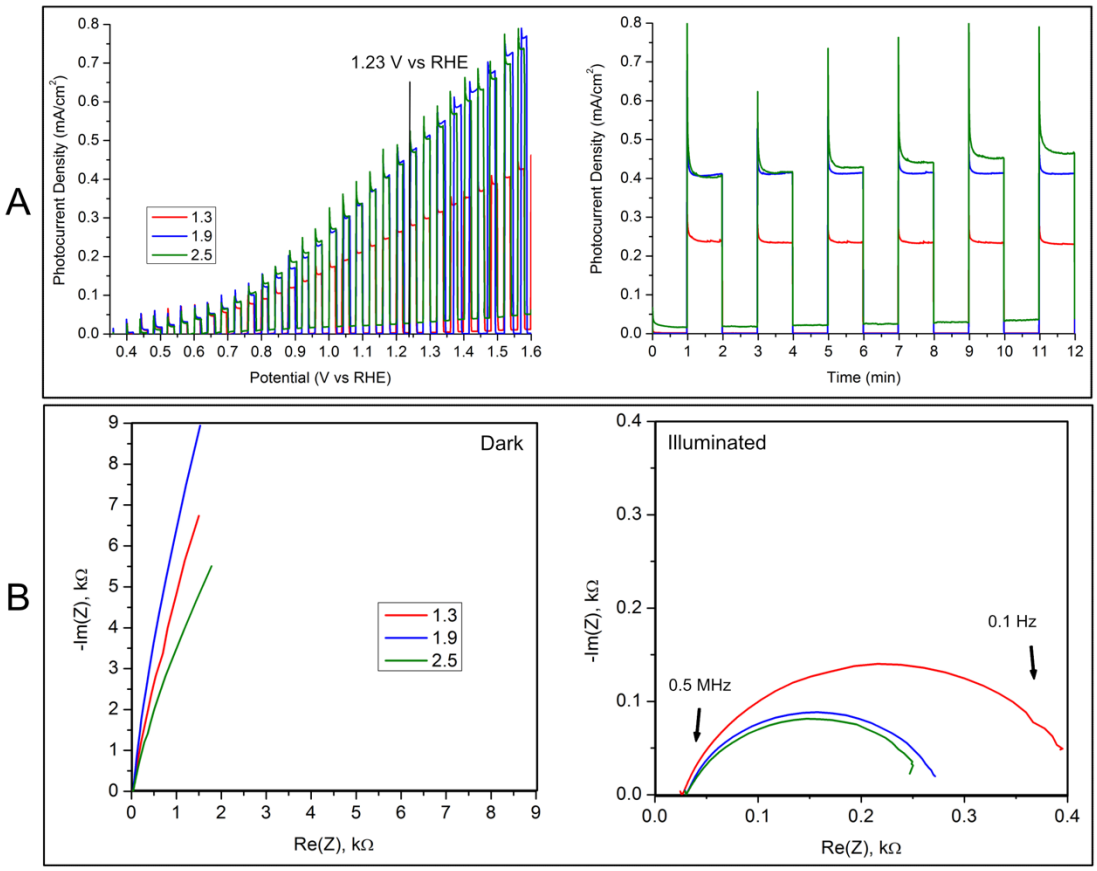

Figure 14. Photoelectrochemical characterization of samples at various Bi-Ki to benzoquinone-EtOH ratios, at electrodeposition time of 5.25 min and calcination temperature of 425°C. (RED: 1.3, BLUE: 1.9, GREEN: 2.5). (A) linear sweep voltammograms (electrolyte: 0.1 M Na-Pi pH 7, scan rate: 10 mV/s), and chronoamperometry plots (electrolyte: 0.1 M Na-Pi pH 7, potential: 1.23 V vs RHE), (B) Nyquist plots under dark and illuminated conditions.

The donor density values in Appendix 3 revealed that this value was the highest for the 1.9 ratio (4.66 x 10^{19} cm^{-3}), immediately followed by the 2.5 ratio (4.1 x 10^{19} cm^{-3}), while the 1.3 ratio has the least donor density (3.46 x 10^{19} cm^{-3}).

Meanwhile, the onset potential was equal for both the 1.9 ratio and 2.5 ratio (0.36 V vs RHE), while it was higher for the 1.3 ratio (0.4 V vs RHE).

Overall, the almost similar photocurrent density obtained for the 1.9 ratio sample and the 2.5 ratio sample was mainly due to the following photoelectrochemical characteristics: equal onset potentials and almost equal charge transfer resistances. Moreover, the physico-chemical properties of these samples such as morphology, thickness and band gap energies are also similar.

3.2.3 Optimization results

The Central Composite Design (CCD) embedded in the software Design Expert was used in the optimization studies. Three-dimensional response surface plots were generated as shown in Figure 15, to identify the ideal region of operability for this process.

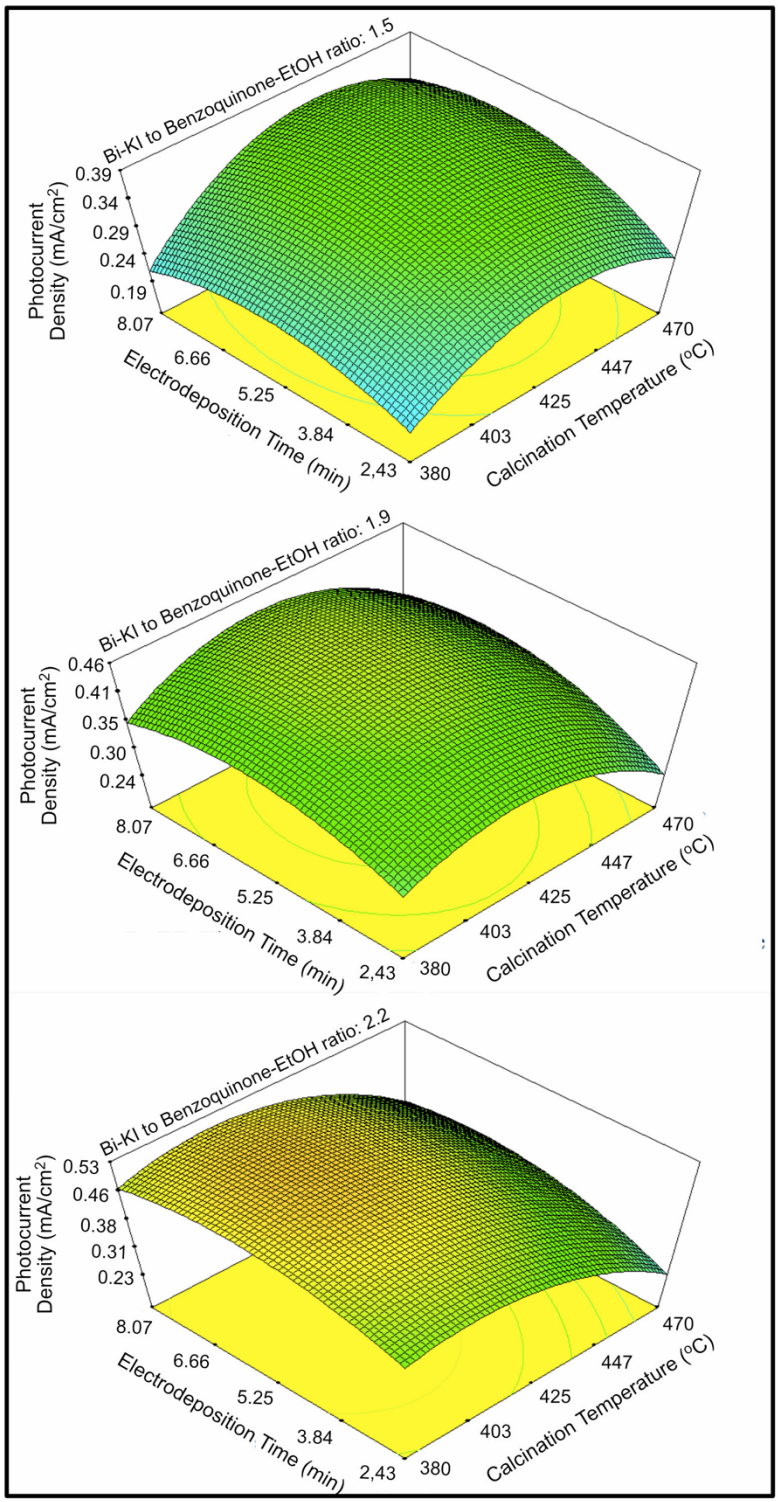

Figure 15. Response surface plots of optimization studies

An initial factor screening scheme (see Appendix 1) was implemented to identify the critical factors that affect the response variable (the photocurrent density). Response surface methodology (RSM) then produced an empirical polynomial model based on the Taylor series to yield an approximation of the response surface over a region of factors, while also considering the interaction of these factors. What has been described in the previous sections were the resulting behavior of the photocurrent density that was achieved by changing the values of

one factor at a time, while keeping the two remaining factors constant at one level/value. However, the response could change when the experiment is performed at a different value of the factors that were held constant, as a result of factor interactions, and this is what is being captured by studying the whole response surface.

Considering the 6-point replication that was performed, it can be reported that this process yielded an experimental value for the photocurrent density of 0.45 ± 0.05 mA/cm^2 at 1.23 V vs RHE for an electrodeposition time of 5.25 minutes, calcination temperature of 425 ^{o}C, and a Bi-KI to benzoquinone-EtOH ratio of 1.9. The optimization response surface plots in Figure 15 indicate that an optimal photocurrent density of 0.53 mA/cm^2 at 1.23 V vs RHE can be obtained by changing the Bi-KI to benzoquinone-EtOH ratio to 2.2. It was earlier shown experimentally that the resulting photocurrent density for the Bi-KI to benzoquinone-ratios 1.9 and 2.5 yielded similar photocurrent responses. Thus, it can already be stated that the photocurrent density that were experimentally obtained at an electrodeposition time of 5.25 minutes, a calcination temperature of 425 ^{o}C, and a Bi-KI to benzoquinone-EtOH ratio of 1.9 already lies within the optimal region of the response surface, and is already indicative of the desired window of operability for the water oxidation reaction using $BiVO_4$ photoanodes..

3.3 Conclusion

In this work, the optimization of $BiVO_4$ photoanode preparation via thin film electrodeposition on FTO was performed. Factors affecting the photoelectrochemical activity such as the electrodeposition time, ratio of the Bismuth precursor to the reduced reagent in the deposition bath, and the calcination temperature, have been investigated by using the Central Composite Design of Experiments. Pristine monoclinic scheelite $BiVO_4$ photoanodes having a photocurrent density of 0.45 ± 0.05mA/cm^2 at 1.23 V vs RHE have been obtained. It was shown that a high photocurrent density are generally dictated by the following physico-chemical properties: higher crystallite size, an optimal thickness, and a more compact, porous morphology. Furthermore, the following photoelectrochemical characteristics give rise to a higher photocurrent density: low onset potential, and a high donor density.

Chapter 4

$BiVO_4$ surface chemistry and modification

This chapter presents novel findings about the $BiVO_4$ surface characteristics. An organometallic chemistry approach was used to study this very important surface as well as to introduce surface modifications that could help improve the photoactivity and stability of this material. These surface modifications include the addition of overlayers as well as a water oxidation co-catalyst, the results of which are thoroughly discussed in the sections which follow.

$BiVO_4$ is a suitable photo-anode for the photo-electrochemical splitting of water, however, surface states on the $BiVO_4$ surface give rise to defect levels, which can mediate electron-hole recombination via the Shockley-Read-Hall mechanism[5]. In order to minimize the inefficiencies arising from electron-hole recombination and passivate the surface states, ultrathin overlayers of Al_2O_3 and TiO_2 were deposited to the $BiVO_4$ thin films that were synthesized via an electrodeposition method, in an ALD-like manner. This was also performed in an attempt to protect the $BiVO_4$ surface and increase its stability.

Moreover, this chapter presents useful information about the surface chemistry of $BiVO_4$ based on experimental methods, and gives unique insights on the characterization of the $BiVO_4$ surface.

4.1 $BiVO_4$ surface chemistry

4.1.1 Materials and Methods

Materials

Bismuth (III) nitrate pentahydrate ($Bi(NO_3)_3.5H_2O$,98%) was utilized as received from Strem Chemicals. Ammonium metavanadate (NH_4VO_3, 99%), ammonium carbonate ($(NH_4)_2CO_3$, ACS reagent), absolute ethanol (CH_3CH_2OH, ≥99.8%), and nitric acid (HNO_3,70%) were utilized as-received from Sigma-Aldrich. Trimethylaluminum ($AlMe_3$, 2M in toluene), titanium isopropoxide ($Ti[OCH(CH_3)_2]_4$, 99.999% trace metals basis), n-butyllithium (2.5 M in hexane) were obtained from Sigma-Aldrich and degassed prior to use. Degassed demineralized water (~15 MΩ cm), were used for all the grafting and ALD-like processes in the experiments while ultrapure water (~18 MΩ cm) were used for all other water requirements.

Synthesis of $BiVO_4$ powder

The $BiVO_4$ powder was synthesized via a hydrothermal method. $Bi(NO_3)_3•5H_2O$ (1.81g) was dissolved in 75 mL of 1 M HNO_3. Then, 1.16 g of $(NH_4)_2CO_3$ was slowly added to the Bi solution, after which 0.439g of NH_4VO_3 was dissolved into the solution. The resulting solution was then loaded to the autoclave, where it was heated at 180°C for 12 hours at a ramp rate of 5°C/min. The procedure, actual solution, and the actual product obtained are shown in Figure 16.

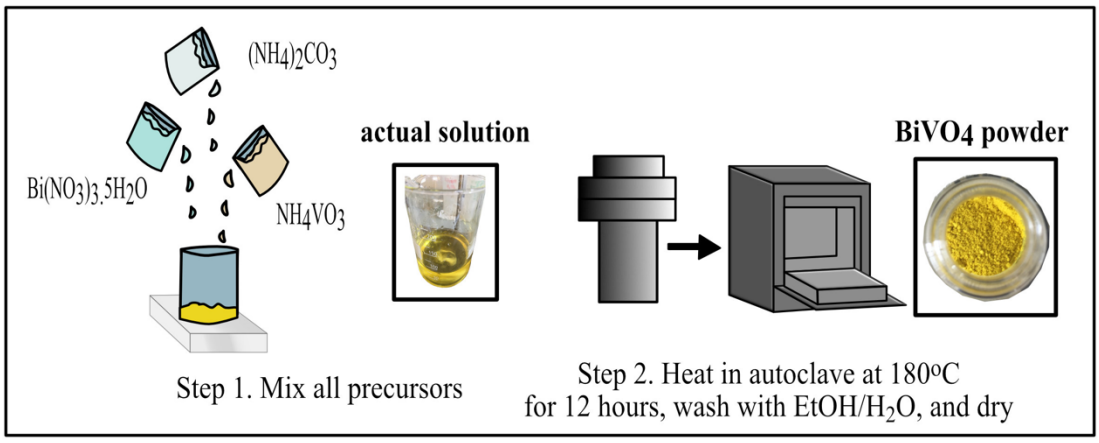

Figure 16. Hydrothermal synthesis of $BiVO_4$ powder

The precipitates were alternately washed with water and ethanol thrice, and then dried in the oven. Calcination of the dried precipitates was done for 2 hours at 400°C and a ramp rate of 5°C/min.

Chemical titration with n-BuLi

The hydrothermally-synthesized $BiVO_4$ powder was treated under ultra-high vacuum (UHV, ~ 10^{-5} mbar) at 400°C for 12 hours. A 1.001 mg sample was placed

in one compartment of a double Schlenk tube while the n-BuLi was placed on the other compartment. Degassed pentane was used as a solvent for the $BiVO_4$ powder. The chemical titration process was performed by adding an excess of the n-BuLi to the degassed pentane containing the $BiVO_4$ powder.

Material Characterization

A Merlin Zeiss Field Emission – Scanning Electron Microscope (FE-SEM) equipped with an Energy Dispersive X-ray Spectroscopy System (EDS) was used to study the morphology of the samples. The XRD spectra were obtained by using an X'Pert Phillips diffractometer under Cu Kα radiation (λ =1.5418 Å) set at 40 kV and 40 mA. N_2 adsorption and desorption isotherms were obtained at 77K on a degassed sample using Belsorp-Max from BEL-JAPAN. DRIFTS spectra were obtained using a Nicolet 6700-FT spectrometer. Gas chromatography (GC) measurements were determined using a HP 5890 gas chromatograph equipped with a flame ionization detector (FID) and a KCl/Al_2O_3 on fused silica column (50 m x 0.32 mm).

4.1.2 Results and Discussion

Morphology

From Figure 17, it is quite evident that there were very distinct differences between the resulting morphologies of the $BiVO_4$ powder that was synthesized hydrothermally, and the thin-film electrode that was synthesized as described in Chapter 3. The XRD spectra showed that both samples manifested the monoclinic scheelite structure (JCPDS No. 14-0688, space group: I2/a, a=5.195, b=11.701, c=5.092, β=90.38^o), which is evident from the peak splitting at the 18.5^o and 35^o of 2θ.

By looking at the morphology, it can be seen that the $BiVO_4$ powder was visibly more agglomerated and packed together, exhibiting bigger grain sizes, while the thin film electrode showed a more porous structure that is not agglomerated, and with smaller grains. In agreement with this, the crystallite sizes for the powder and thin film are found to be 320 and 112 nm, respectively. More intense peaks were observed from the powder samples because of the higher amount of material present than in the thin-film electrode. From FESEM-EDS, the ratio of Bi/V for each of the samples was both found to be 1.07, which means that the 1:1 ratio of Bi:V is well-maintained in the bulk. Nitrogen adsorption-desorption isotherms were used for the BET surface area measurements for the $BiVO_4$ powder, which revealed a very low surface area of 2-4 m^2/g.

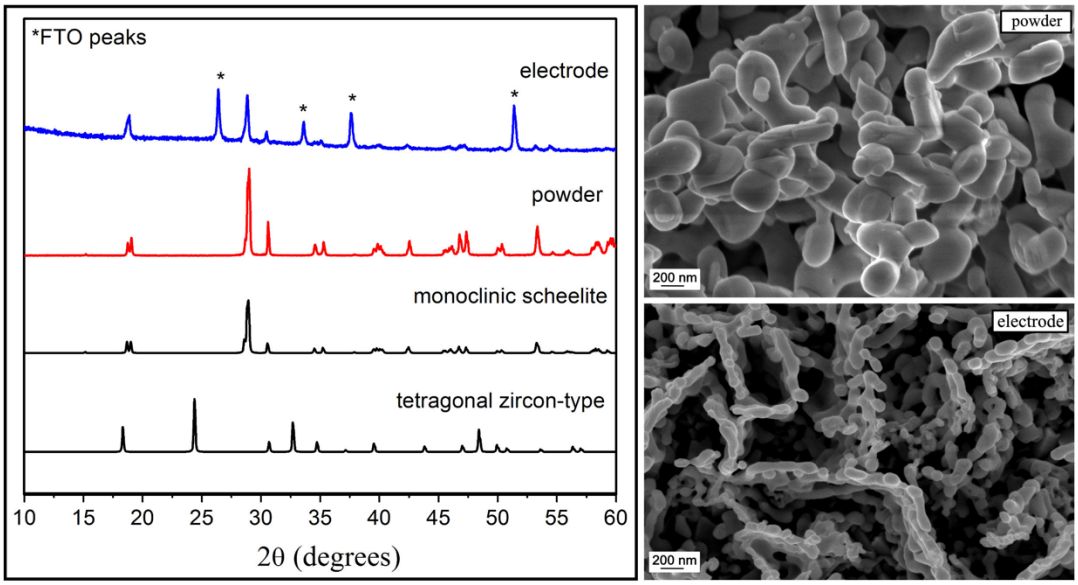

Figure 17. XRD and FESEM images of $BiVO_4$ powder and thin-film electrode

Nature of $BiVO_4$ powder surface

As mentioned in the previous chapter, $BiVO_4$ contains surface hydroxyl groups. However, based on an FTIR spectra, it is not very easy to confirm the presence of these surface hydroxyl groups on $BiVO_4$, possibly because of the very low surface area of $BiVO_4$, and of the low quantity of OH groups that are present. In order to be certain about this, chemical titration was performed with a strong base, n-butyllithium (n-BuLi, pKa ~50). The n-BuLi is known to react with the surface hydroxyls and chemisorbed water of inorganic oxides studied[132] to yield butane (C_4H_{10}) that can be quantified using a gas chromatograph (GC).

From the n-BuLi reaction, 8.752 μmol of butane gas (C_4H_{10}) was evolved when contacted with the thermally-treated $BiVO_4$. If one extrapolated such chemical reaction to exclusive reaction with surface hydroxyls, the result translates to 1.5 OH/nm^2 on the $BiVO_4$ surface. The reader is referred to Appendix 5 for the gas chromatography calculations.

The IR spectra of the pristine $BiVO_4$ powder (black line) and the titrated $BiVO_4$ powder (red line) in the 500 to 2000 cm^{-1} region is shown in Figure 18. The $BiVO_4$ powder titrated with n-BuLi showed two distinct IR bands in the 1098.5 cm^{-1} and 1259 cm^{-1} regions. The first peak at 1098.5 cm^{-1}is attributed to the ionic structure of Li^+O^{2-}, with the molecule consisting of electrostatically bound Li and O[133,134]. The second peak at 1259 cm^{-1} is possibly a C-O stretching. The interpretation of this particular peak and the accompanying chemical processes which led to it should be studied more deeply. This preliminary data necessitate further studies to fully characterize the surface chemical species and to ensure that no other chemical reactivity has occurred other than the hydroxyl to O-Li$^+$ titration with concomitant

alkane stoichiometric release . As of now, the 1.5 OH/nm² can be considered as an upper boundary estimate of the hydroxyl population on the $BiVO_4$ surface. To the best of our knowledge, this quantification of the OH groups in $BiVO_4$ surface has not been reported in literature.

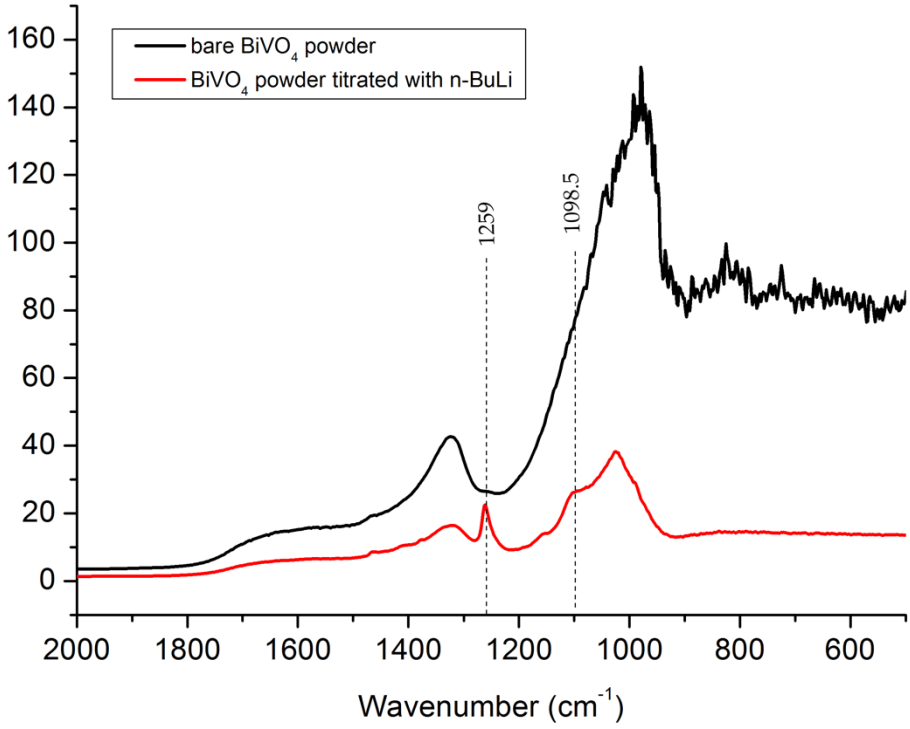

Figure 18. FTIR spectra of bare $BiVO_4$ and $BiVO_4$ titrated with n-BuLi

The $BiVO_4$ surface with the least surface energy according to theoretical calculations based on the density functional theory (DFT), are (010) and (110). Zhao *et al*[135] reported that for the (010) surface, the V atoms are fully-coordinated, and all the dangling bonds are derived from the broken Bi-O bonds, which means that the VO_4 tetrahedron remains intact while the BiO_8 dodecahedron is cut, exposing 2 x 2-fold coordinated O atoms in the surface. From the same study, it was reported that the (110) surface exposes fully 4-fold coordinated V atoms as well as coordinately unsaturated atoms, three 2-fold coordinated O atoms and a 5-fold coordinated Bi atom[135]. However, it should be recalled from the XPS measurements that were reported in Chapter 3 that V^{4+} species dominated the surface of the prepared $BiVO_4$ electrodes in this study.

Another surface which is of great interest as mentioned in Chapter 3 is the (040) surface because of the enhanced photocatalytic activity that is reportedly associated with it. As shown in Appendix 6, the (040) surface has 2 x 5-fold coordinated Bi atoms and 2 x 2-fold coordinated V atoms. These information about the surface termination of $BiVO_4$ is crucial and can offer possible links with regard to the physico-chemical properties of the $BiVO_4$, and can aid in understanding how to

better engineer or modify the surface given its proven influence in the photoactivity of this material.

4.2 $BiVO_4$ surface modification

4.2.1 Materials and Methods

Materials

For the synthesis of the $BiVO_4$ powder, bismuth (III) nitrate pentahydrate ($Bi(NO_3)_3.5H_2O$,98%) was utilized as received from Strem Chemicals. Ammonium metavanadate (NH_4VO_3,99%), ammonium carbonate ($(NH_4)_2CO_3$, ACS reagent), absolute ethanol (CH_3CH_2OH, ≥99.8%), and nitric acid (HNO_3,70%) were utilized as-received from Sigma-Aldrich.

For the synthesis of the $BiVO_4$ thin film electrodes, bismuth (III) nitrate pentahydrate ($Bi(NO_3)_3.5H_2O$, ≥98%), vanadyl acetylacetonate ($VO(acac)_2$, ≥98%), potassium iodide (KI, ≥99%), p-benzoquinone ($C_6H_4(=O)_2$, ≥98%), absolute ethanol (CH_3CH_2OH, ETOH,≥99.8%), dimethyl sulfoxide/DMSO ($(CH_3)_2SO$, ≥99.9%), nitric acid (HNO_3,70%) and sodium hydroxide (NaOH pellets, ≥97%), were utilized as-received from Sigma-Aldrich. Fluorine-doped tin oxide (FTO) conductive glasses with a sheet resistance of 7 Ω/cm^2 were obtained from Solaronix Inc. The FTO glasses were cleaned by sonicating in acetone, ethanol and water, respectively, for 10 minutes each, prior their use.

Trimethylaluminum ($AlMe_3$, 2M in toluene) and titanium isopropoxide ($Ti[OCH(CH_3)_2]_4$, 99.999% trace metals basis) were obtained from Sigma-Aldrich and degassed prior to use. Degassed demineralized water (~15 MΩ cm), were used for all the grafting and ALD-like processes in the experiments while ultrapure water (~18 MΩ cm) were used for all other water requirements. Colloidal Ni60-Mo40 (37.7 mg/L) nanoparticles were obtained from Aalto University.

Material Characterization

A Merlin Zeiss Field Emission – Scanning Electron Microscope (FE-SEM) equipped with an Energy Dispersive X-ray Spectroscopy System (EDS) was used to study the morphology of the samples. The XRD spectra were obtained by using an X'Pert Phillips diffractometer under Cu Kα radiation (λ =1.5418 Å) set at 40 kV and 40 mA. DRIFTS spectra were obtained using a Nicolet 6700-FT spectrometer. Gas chromatography (GC) measurements were determined using a HP 5890 gas chromatograph equipped with a flame ionization detector (FID) and a KCl/Al_2O_3 on fused silica column (50 m x 0.32 mm). EPR measurements were performed by Mr. Lhoussain Khrouz at ENS de Lyon on a Bruker EXELSYS E500 spectrometer at 120K.

Addition of Al_2O_3 overlayer on $BiVO_4$ powder

The hydrothermally-synthesized $BiVO_4$ powder was dehydroxylated under an ultra-high vacuum (UHV, ~ 10^{-5} mbar) at 400°C for 12 hours. A 5.885 mol of

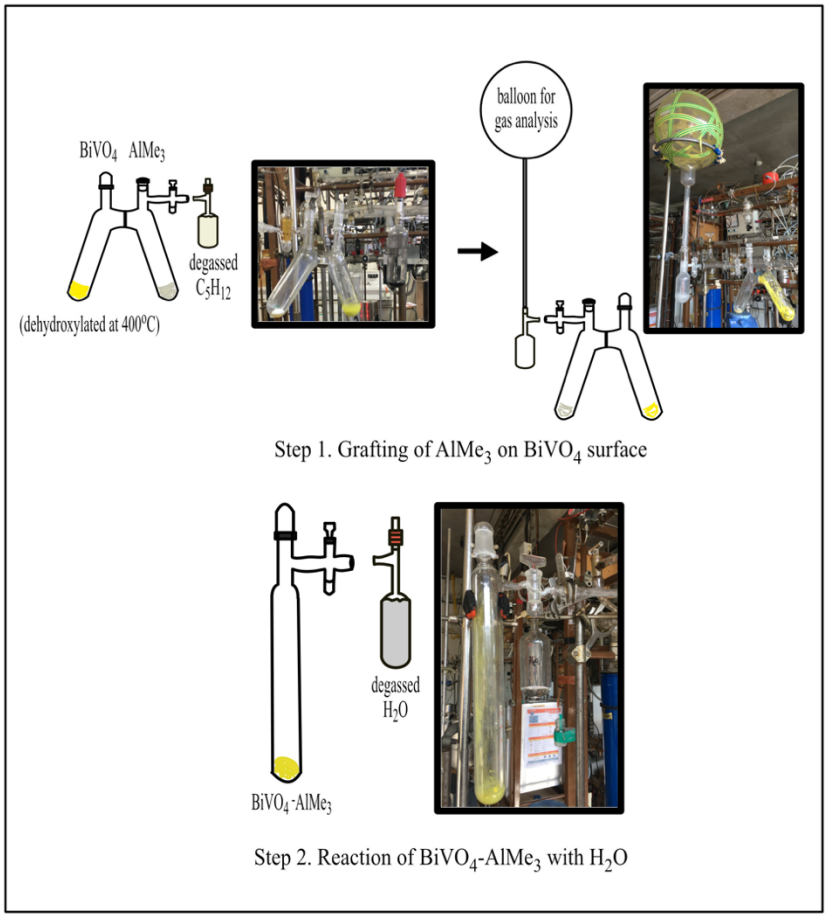

Figure 19. Surface modification of $BiVO_4$ powder with Al_2O_3

dehydroxylated sample was placed in one compartment of a double Schlenk tube while 1.2 mmol of $AlMe_3$ (2.0 M in toluene) was placed on the other compartment. Degassed pentane was used as a solvent for the $BiVO_4$ powder. The system was connected to an ultra-high vacuum line which is used to manipulate the transfer of liquids with the aid of liquid nitrogen, via pressure gradients. The first pulse was performed by adding the $AlMe_3$ to the degassed pentane containing the $BiVO_4$ powder. The reaction time used was 1 hour. The evolved gas was then collected in a 10 L gas balloon for analysis. The procedure is illustrated in Figure 19.

After the reaction for the 1st pulse, all the unreacted $AlMe_3$ was removed using the UHV. The $AlMe_3$-$BiVO_4$ sample was then placed in a 200 mL glass reactor for the 2nd pulse. Degassed water was introduced into the reactor and all unreacted H_2O was then removed from the system.

Addition of Al_2O_3 and TiO_2 overlayers on the $BiVO_4$ electrode

The modification of the $BiVO_4$ electrodes with Al_2O_3 and TiO_2 were done using a glass reactor with 2 ball compartments separating the precursors, as shown in

Figure 20. The whole system was connected to an UHV line which was used to manipulate the transfer of liquids with the aid of liquid nitrogen, using pressure gradients.

For the Al_2O_3 overlayer, the first pulse was the $AlMe_3$. A reaction time of 30 minutes at a temperature of 60°C was used. All the unreacted $AlMe_3$ was removed. Then, the 2nd pulse (degassed H_2O) was introduced. The reaction time was kept constant at 30 minutes using a temperature of 60°C. All the unreacted H_2O was then removed after the reaction. The samples were calcined under air at 380°C for 30 minutes at 2°C/min ramp rate. One cycle consists of 1 pulse of each precursor. Various cycles of Al_2O_3 were investigated.

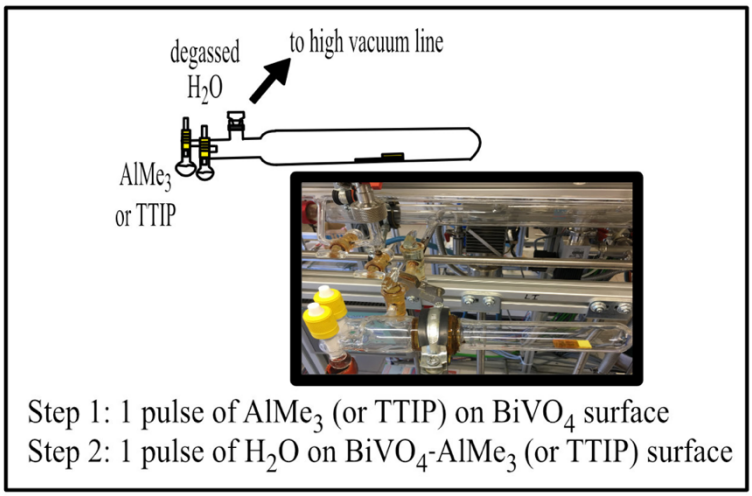

Figure 20. Surface modification of $BiVO_4$ electrode

For the TiO_2 overlayer, the first pulse was the titanium isopropoxide (TTIP). A reaction time of 30 minutes at a temperature of 150°C was used. All the unreacted TTIP was removed. Then, the 2nd pulse (degassed H_2O) was introduced. The reaction time was kept constant at 30 minutes and a temperature of 150°C. All the unreacted H_2O was then removed after the reaction. Some samples were calcined under air at 550°C for 60 minutes at 2°C/min ramp rate while one sample was kept amorphous. One cycle consists of 1 pulse of each precursor. Various cycles of TiO_2 were investigated.

Addition of OEC overlayer on $BiVO_4$ electrode

A 100 μL colloidal solution of Ni60-Mo40 nanoparticles in acetone was added dropwise to the $BiVO_4$ electrode and then air-dried overnight.

Photoelectrochemical Characterization

The photoelectrochemical tests were performed in the same manner as described in Chapter 3. In addition, rapid scan voltammetry was performed by Dr. Fatwa Abdi of Helmholtz-Zentrum Berlin. A constant potential of 1.5 V vs

Ag/AgCl (2.1 V vs RHE) for 2 minutes as a conditioning step, followed by a quick potential sweep to -0.2 V vs Ag/AgCl (0.4 V vs RHE) with a scan rate of 1 V/s. Comparison of the curves with and without conditioning yields the surface capacitance (C) through the equation $C=(J_{\text{with cond}} - J_{\text{w/out cond}})/\text{scan rate}$.

4.2.2 Al_2O_3 overlayer on $BiVO_4$ powder

The addition of an Al_2O_3 overlayer on $BiVO_4$ powder was performed in order to understand how the $BiVO_4$ - Al_2O_3 interface is formed, and to be able to closely follow these processes using several powder characterization techniques. From literature, it is well-understood that Al_2O_3 can be grown on high surface area substrates like silica, that are populated with surface OH groups. The expected mechanism is shown below, with * denoting the surface species[136].

$$\text{(A) Al-OH}^* + \text{Al(CH}_3)_3 \longrightarrow \text{Al-O-Al(CH}_3)_3^* + \text{CH}_4$$
$$\text{(B) Al-CH}_3^* + \text{H}_2\text{O} \longrightarrow \text{Al-OH}^* + \text{CH}_4$$

When the reaction is performed in a sequential manner, i.e. A-B-A-B-A-B…, a controlled layer-by-layer growth of Al_2O_3 is achieved. However, to the best of our knowledge, the mechanism of the growth of an Al_2O_3 overlayer on $BiVO_4$ has not been investigated to date. We have earlier established and quantified the presence of OH groups on the $BiVO_4$ surface in the beginning of this chapter, and we have hypothesized that the same OH groups can serve as initial binding sites for the Al atoms as indicated in sequence A. Consequently, the growth of the Al_2O_3 in an A-B-A-B-A-B sequential manner can also be achieved on $BiVO_4$.

Figure 21 shows the IR spectra of the dehydroxylated pristine $BiVO_4$, $BiVO_4$ powder with 1 pulse of $AlMe_3$, and finally, after reaction with H_2O. Dehydroxylated bare $BiVO_4$, which is the starting surface for the 1st pulse of $AlMe_3$, is characterized by peaks at 720 cm^{-1}, 826 cm^{-1}, and 977 cm^{-1} which correspond to V-O waging, symmetric, and asymmetric vibrations, respectively[135]. The peaks associated with O-H stretching vibrations are seen in 3374 cm^{-1} and 3700 cm^{-1} wavenumbers, although for the case of $BiVO_4$ it is not readily seen in the IR spectra as mentioned in the previous section.

Upon addition of the first pulse of $AlMe_3$, the presence of the $AlCH_3$* surface species were observed via the very prominent C-H stretching vibrations seen at 2822-2962 cm^{-1} corresponding to sp^3 C-H stretching, 3015 cm^{-1} corresponding to sp^2 C-H stretching, and the symmetric Al-CH_3 deformation mode at 1207 cm^{-1} [135]. The subsequent H_2O pulse resulted to a broadened O-H band at 3400 cm^{-1} brought about by adsorbed water molecules and with contributions from AlO-H stretching vibrations from AlOH* surface species in the 3600 cm^{-1} region[135].

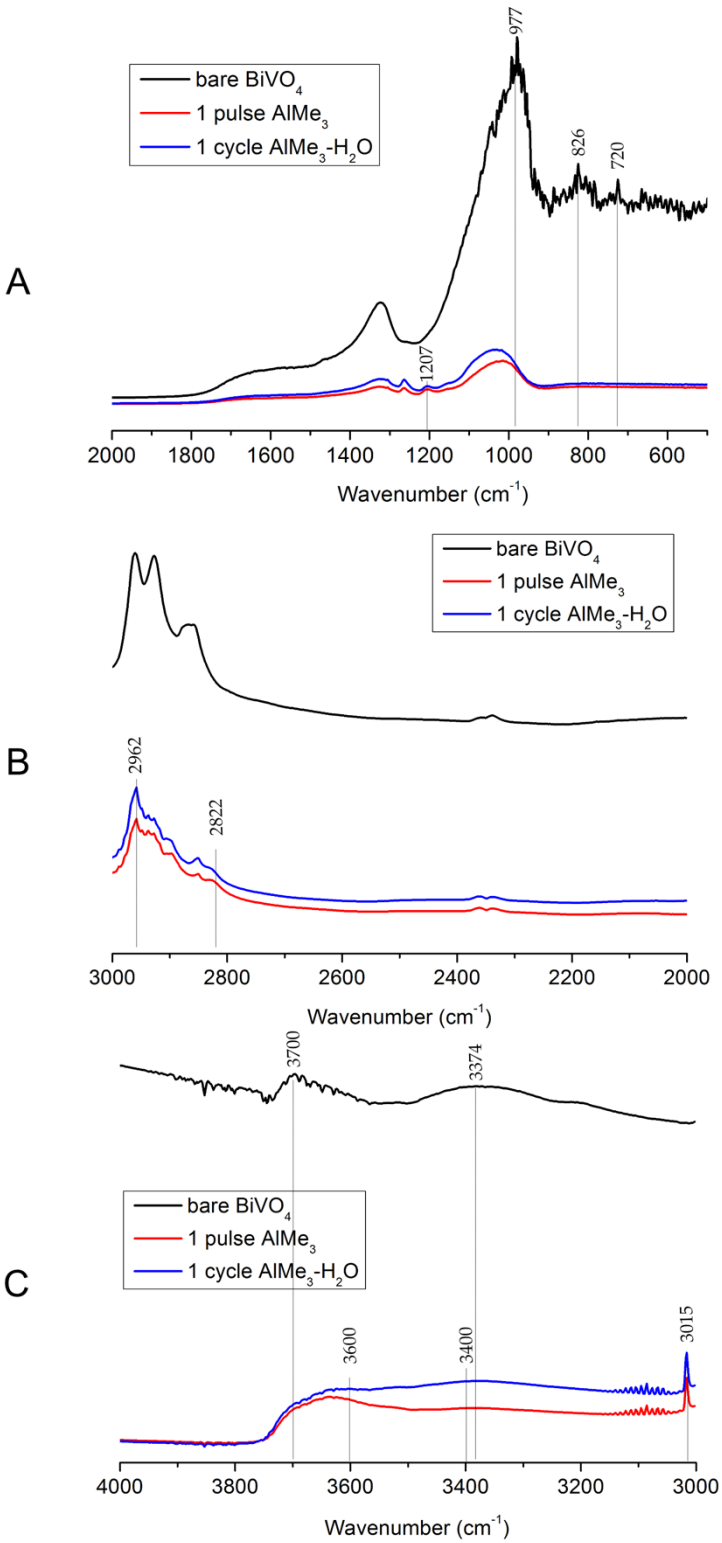

Figure 21. FTIR Spectra of dehydroxylated bare $BiVO_4$ powder, $BiVO_4$ powder with 1 pulse of $AlMe_3$ and 1 cycle $AlMe_3$-H_2O at (A) 2000-500 cm^{-1} wavenumbers, (B) 3000-2000 cm^{-1} wavenumber, (C) 4000-3000 cm^{-1} wavenumber

The quantity of methane evolved in the hydrolysis step was determined by gas chromatography (GC). There are 1.8 CH_4 molecules per nm^2 that were evolved upon addition of the H_2O pulse to the $AlMe_3$-modified $BiVO_4$. If the CH_4 evolution

is measured on a per OH basis, the corresponding quantities are 1.2 CH_4/Bi-OH for 1 pulse $AlMe_3$ followed by 1 pulse of H_2O.

Electron paramagnetic resonance (EPR) is a technique used to study the energy differences arising from the interaction of a magnetic field with unpaired electrons in the sample. Because of the unpaired electron spins, the molecule exhibits paramagnetism, and transitions can be induced by applying a magnetic field. This spectroscopic technique is analogous to nuclear magnetic resonance (NMR) spectroscopy, however, in EPR it is the electron spins that are excited instead of the nuclei spins.

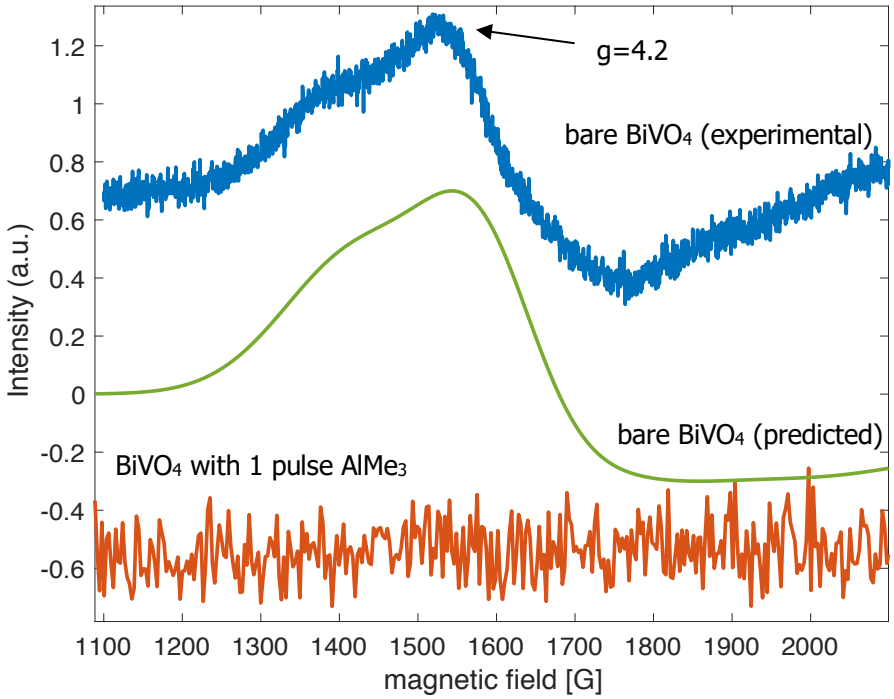

Figure 22. EPR spectra of bare $BiVO_4$ and $BiVO_4$ with 1 pulse of $AlMe_3$

In $BiVO_4$, the EPR signal may be induced by the reduced V ions (V^{4+}) arising from surface states/defect structures. In a perfectly crystalline $BiVO_4$ that is defect-free, V ions manifest as V^{5+} which is diamagnetic, which is not detected by EPR[137]. Thus, the peak with the g-factor of 4.2 indicated in Figure 22 is assigned to V^{4+} [138]. It is not an isolated V^{4+}, but rather one that is possibly in dipole interaction with another V^{4+}, or with a radical O. It is worth noting that this particular peak is absent in the $BiVO_4$ with 1 pulse of $AlMe_3$.

4.2.3 Al_2O_3 overlayer on $BiVO_4$ electrode

The effect of varying the number of cycles in the ALD-like deposition method on the photoactivity of the $BiVO_4$ thin film electrodes was investigated. Figure 23A shows the linear sweep voltammetry (LSV) curves under chopped light conditions for all the samples modified with "Al_2O_3", as compared with that of the bare $BiVO_4$

thin film electrode. Indeed, for very few pulses of $AlMe_3$-H_2O cycles, the formation of alumina oxide cannot be inferred, but the nomenclature Al_2O_3 will be used throughout for simplicity. All curves manifested the initial current spikes appearing readily when the light source was turned on, which eventually dampened, which suggests the occurrence of fast electron-hole recombination. For the bare $BiVO_4$ sample, a photocurrent density of 0.35 mA/cm^2 at 1.23 V vs RHE was achieved. It can be clearly seen from the same figure that an improvement in photocurrent density values was achieved with 2 cycles and 5 cycles of Al_2O_3 deposition, yielding 0.54 mA/cm^2 at 1.23 V vs RHE and 0.49 mA/cm^2 at 1.23 V vs RHE, respectively. However, the least photocurrent density was observed when the number of cycles of Al_2O_3 deposition was increased to 8. It is noteworthy that the reaction temperature used in the ALD-like deposition of Al_2O_3 on the $BiVO_4$ surface which yielded the better performance is low enough at 60^{o}C, which is not commonly demonstrated in typical ALD processes involving Al_2O_3, commonly performed at 125-500^{o}C[136].

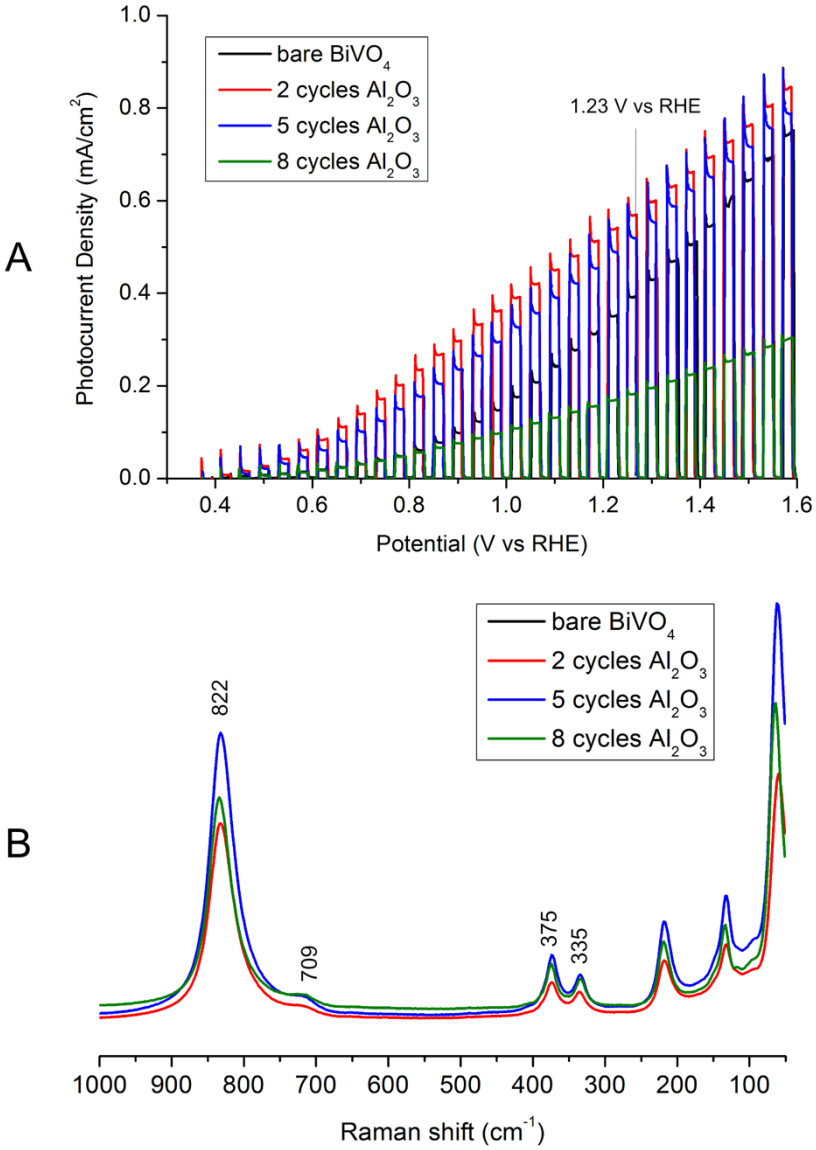

Figure 23. (A) LSV plot (electrolyte: 0.1M Na-Pi pH 7, scan rate: 10 mV/s) and (B) Raman spectra for bare $BiVO_4$ and Al_2O_3-modified $BiVO_4$

The Raman spectra of bare and Al_2O_3-modified $BiVO_4$ thin film electrodes are shown in Figure 23B. The most intense band at 822 cm^{-1} is assigned to the V-O stretching mode. The weak shoulder at 709 cm^{-1} is assigned to antisymmetric V-O stretching, and the bands at 375 cm^{-1} and 335 cm^{-1} correspond to the symmetric and antisymmetric bending of VO_4 tetrahedra. All plots are similar for the bare $BiVO_4$ and Al_2O_3-modified samples, which means that the Al_2O_3 did not induce structure modifications on the $BiVO_4$.

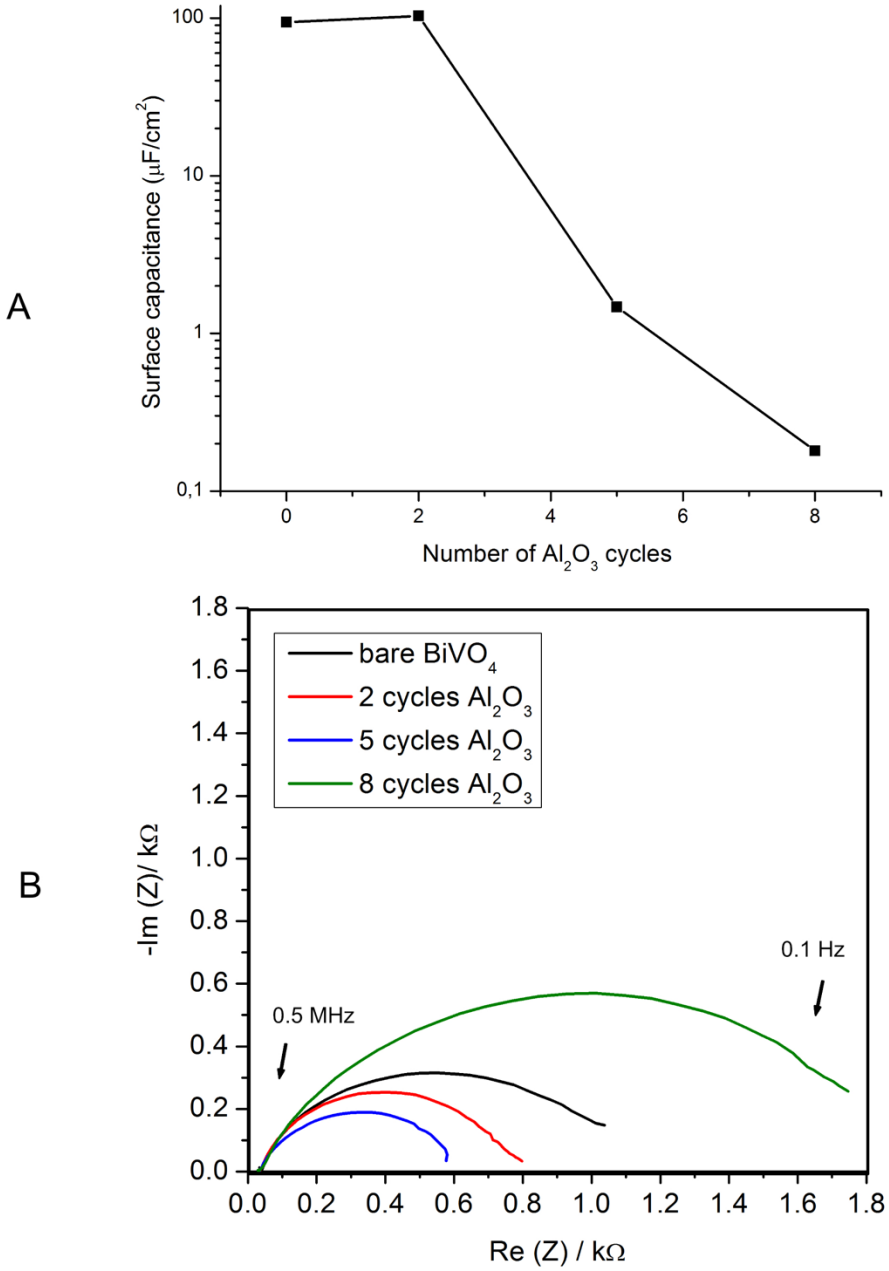

Figure 24. (A) Surface capacitance and (B) Nyquist impedance plots for bare and Al_2O_3-modified $BiVO_4$

In order to verify if the Al_2O_3 overlayer is indeed passivating the surface states in the $BiVO_4$ electrode surface, rapid scan voltammetry was performed to determine

the surface capacitance of the electrodes. As shown in Figure 24A, the surface capacitance decreases by orders of magnitude with increasing number of cycles of Al_2O_3, in agreement with passivating surface states that serve as charge recombination sites. This is very significant, because the photocurrent of $BiVO_4$ is limited more by surface recombination than the charge transfer[139].

Meanwhile, the Nyquist impedance plot is shown in Figure 24B. The charge transfer resistance, which was indicated by the diameter of the arc, is seen to be highest for the 8 cycles Al_2O_3 electrode (green arc), and greater than that of bare $BiVO_4$ (black arc). This is consistent with the trend observed for the photocurrent density, where it was seen that the bare $BiVO_4$ performed better than the 8 cycles Al_2O_3. Therefore, the thickest layer of Al_2O_3 overlayer contributed in slowing down the transfer of holes on the $BiVO_4$-electrolyte interface. Also, it can be seen from Figure 24B, that the 2 cycles Al_2O_3 (red arc) and the 5 cycles Al_2O_3 (blue arc) have lower charge transfer resistances than the bare $BiVO_4$, thus, both having higher photocurrent density relative to the bare $BiVO_4$. However, between these 2 electrodes, it turned out that the 5 cycles Al_2O_3 has a lower charge transfer resistance than the 2 cycles Al_2O_3, which was the opposite behaviour of the observed photocurrent density. It appears that the higher photocurrent density of the 2 cycles Al_2O_3 electrode is explained by the donor densities as derived from the Mott-Schottky plots, wherein the 2 cycles Al_2O_3 electrode manifested a donor density of 1.49×10^{20} cm^{-3}, while the 5 cycles Al_2O_3 electrode has a lower donor density of 1.16×10^{20} cm^{-3}. As discussed in Chapter 3, the higher donor density can improve the photoelectrochemical response by raising the Fermi level, which creates more band bending that enhances electric field in the space charge layer, thus, lowering the electron-hole recombination. Second, it enhances the electrical conductivity of the photoanode, thus, improving the charge transport properties within the material.

The onset potentials of these electrodes were almost equal at 0.39 V, 0.37 V, 0.38 V, and 0.37 V vs RHE, for bare $BiVO_4$, 2 cycles Al_2O_3, 5 cycles Al_2O_3, and 8 cycles Al_2O_3, respectively.

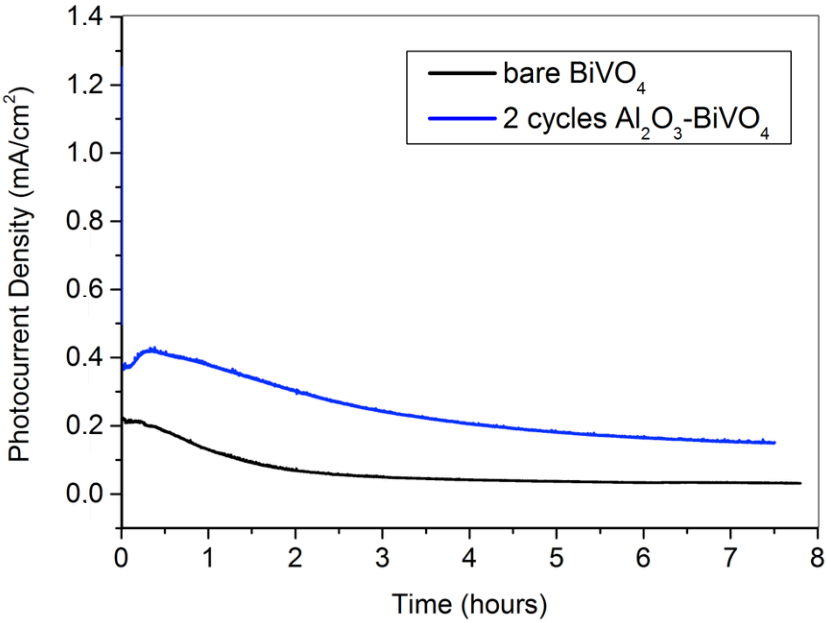

Figure 25. Stability test (chronoamperometry) plot for 2 cycles Al_2O_3 and bare $BiVO_4$ (electrolyte: 0.1 M Na-Pi pH 7, potential: 1.23 V vs RHE)

In addition, the 2 cycles Al_2O_3 electrode, which exhibited the best photocurrent density, was subjected to a stability test along with the bare $BiVO_4$ electrode. The result of the stability test is shown in Figure 25.

The bare $BiVO_4$ (black line) showed an 85% decay in photocurrent density after 7.5 hours while the 2 cycles Al_2O_3 (blue line) sample showed 59.6% decay. Although the stability of the $BiVO_4$ photoanode clearly remains an issue, it was demonstrated here that the presence of an Al_2O_3 overlayer on the $BiVO_4$ surface arrested some of the photocorrosion, and reduced the photocurrent decay by 15%.

4.2.4 TiO_2 overlayer on $BiVO_4$ electrode

The use of a TiO_2 overlayer on the $BiVO_4$ thin film electrodes did not result to an improvement in the photocurrent density as shown in the LSV plots in Figure 26A. Also, among the modified-TiO_2 samples, the highest photocurrent density up until 1.23 V vs RHE was observed for the 3 cycles TiO_2 electrode (green line) that was amorphous.

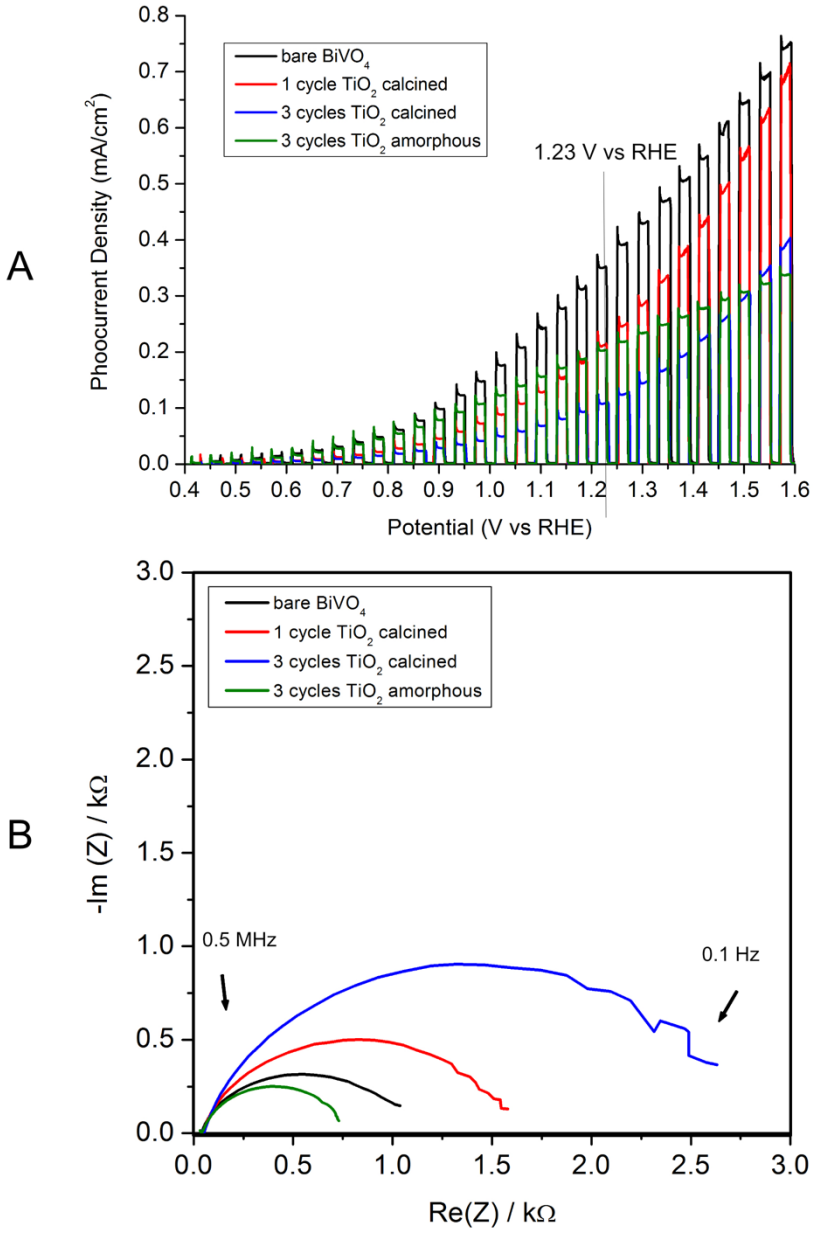

Figure 26. (A) LSV (electrolyte: 0.1 M Na-Pi pH 7, scan rate: 10 mV/s) and (B) Nyquist impedance plots for bare and TiO_2-modified $BiVO_4$

In agreement with this, the Nyquist impedance plot shown in Figure 26B reveal that among the TiO_2-modified samples, the 3 cycles TiO_2 (green arc) has the least charge transfer resistance. However, while this was also true in comparison with the bare $BiVO_4$, the photocurrent density for the 3 cycles TiO_2 was lower than that of bare $BiVO_4$, possibly due to charge recombination phenomena in the bulk. It should be noted that the synthesis conditions that were used for the deposition of the TiO_2 overlayer on the surface of $BiVO_4$ have to be further examined and optimized.

4.2.5 Oxygen evolution catalyst overlayer on $BiVO_4$ electrode

As extensively discussed in Chapter 2, the problem of a sluggish water oxidation kinetics with $BiVO_4$ can be addressed by adding an oxygen evolution catalyst (OEC). This section explored the effect of the addition of an OEC on the bare and Al_2O_3 -modified $BiVO_4$ surfaces.

The OEC used in this study was a colloidal solution of Ni-Mo nanoparticles (60% Ni, 40% Mo) obtained from Aalto University. Ni-Mo is more commonly used as a hydrogen evolution reaction (HER) catalyst. Ni-Mo composites have been extensively studied because they offer the highest activity and stability among non-noble metals and is quite comparable to the activity of Pt[140,141]. Quite recently, the use of colloidal Ni-Mo nanoparticles have been explored and found to be good catalysts for the oxygen evolution reaction as well[142]. In this section, we have evaluated the use of Ni-Mo nanoparticles as an OEC for water oxidation. It was deposited as an overlayer for bare $BiVO_4$ photoanode and the 2 cycles Al_2O_3-$BiVO_4$ photoanode to assess its effect on the photoactivity.

As seen on Figure 27A, addition of Ni-Mo to bare $BiVO_4$ (red line) increases the photocurrent density by 3-fold, from 0.35 mA/cm^2 to 1 mA/cm^2 at 1.23 V vs RHE. This was mainly due to the much lower charge transfer resistance with respect to bare $BiVO_4$, as seen on the Nyquist impedance plot on Figure 27B.

Moreover, it can also be seen from the same plot that the addition of Ni-Mo to $BiVO_4$ with an overlayer of 2 cycles of Al_2O_3 (blue line) produces a photocurrent density (0.39 mA/cm^2 at 1.23 V vs RHE) that is slightly higher than that of the bare $BiVO_4$ for potentials up to 1.3 V vs RHE. From this, it can be inferred that the presence of Al_2O_3 on this $BiVO_4$ surface did not produce synergistic effects in enhancing the photocurrent density along with the Ni-Mo. It is apparent that the charges were able to transfer more efficiently from the $BiVO_4$ surface to the Ni-Mo, than from the Al_2O_3 overlayer to the Ni-Mo. This very important interface needs to be further examined and optimized.

Based on the Nyquist plot in Figure 27, the charge transfer resistance is just slightly lower for the 2 cycles Al_2O_3-$BiVO_4$ with Ni-Mo (blue line) than the $BiVO_4$ with Ni-Mo (red line). However, the photocurrent density of the latter is almost 3 times that of the former. This behaviour can be explained by examining the other photoelectrochemical characteristics.

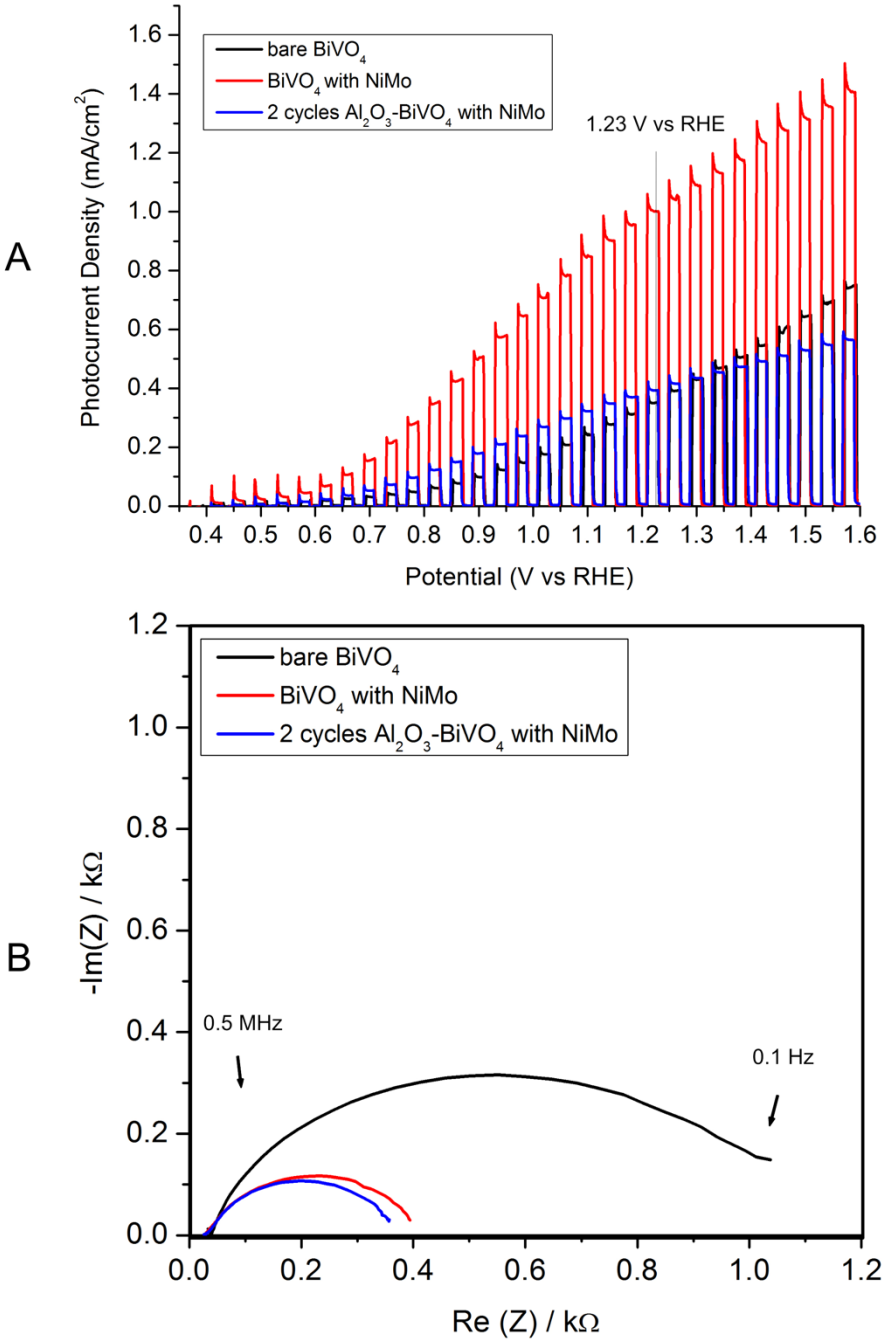

Figure 27. (A) LSV (electrolyte: 0.1 M Na-Pi pH 7, scan rate: 10 mV/s) and (B) Nyquist plots for bare $BiVO_4$, $BiVO_4$ with NiMo and 2 cycles Al_2O_3-$BiVO_4$ with NiMo

The onset potentials for bare $BiVO_4$, $BiVO_4$ with Ni-Mo, and 2 cycles Al_2O_3-$BiVO_4$ with Ni-Mo are 0.37 V, 0.37 V, and 0.41 V vs RHE, respectively. The lower onset potential of the 2 cycles Al_2O_3-$BiVO_4$ with Ni-Mo compared to the $BiVO_4$ with Ni-Mo contributed to the lower photocurrent density of the former. In addition, the donor density derived from Mott-Schottky plots revealed that the $BiVO_4$ with Ni-Mo electrode has a much higher donor density (2.65×10^{20} cm^{-3}) than the 2 cycles Al_2O_3 – $BiVO_4$ with Ni-Mo (0.72×10^{20} cm^{-3}).

4.3 Conclusion

The nature of the $BiVO_4$ surface was studied in this chapter. The existence of surface hydroxyl groups on $BiVO_4$ was confirmed and quantified (max 1.5 OH/nm^2) via chemical titration. The reaction of the $BiVO_4$ powder with one pulse of $AlMe_3$ and 1 pulse of H_2O showed that there were 1.2 molecules of CH_4 evolved per Bi-OH.

Surface states on the $BiVO_4$ surface give rise to defect levels, which can mediate electron-hole recombination via the Shockley-Read-Hall mechanism[5]. In order to minimize the inefficiencies due to electron-hole recombination and passivate the surface states, ultrathin overlayers of Al_2O_3 and TiO_2 were deposited to the $BiVO_4$ thin film electrodes in an ALD-like manner. This was also performed in order to protect the $BiVO_4$ surface from photocorrosion and increase its stability. A photocurrent density of 0.54 mA/cm^2 at 1.23 V vs RHE was obtained for the Al_2O_3-modified $BiVO_4$, which was a 54% improvement from the bare $BiVO_4$ that demonstrated a photocurrent density of 0.35 mA/cm^2 at 1.23 V vs RHE. A 15% increase in stability of the Al_2O_3- modified $BiVO_4$ electrode was also observed over 7.5 hours of continuous irradiation. Moreover, through surface capacitance measurements, it was shown that the Al_2O_3 overlayer was indeed passivating the surface states of the $BiVO_4$ electrodes. Meanwhile, there were no photocurrent density improvements that were observed for the TiO_2-modified $BiVO_4$ at the synthesis conditions that were used in this experiment.

The addition of Ni-Mo to bare $BiVO_4$ increases the photocurrent density by 3-fold, from 0.35 mA/cm^2 to 1 mA/cm^2 at 1.23 V vs RHE. This was mainly due to the much lower charge transfer resistance of this electrode with respect to bare $BiVO_4$. Moreover, the addition of Ni-Mo to $BiVO_4$ with an overlayer of 2 cycles of Al_2O_3 produces a photocurrent density (0.39 mA/cm^2 at 1.23 V vs RHE) that is lower than that of just $BiVO_4$ with Ni-Mo, and slightly higher than that of the bare $BiVO_4$ for potentials up to 1.3 V vs RHE. It is apparent that the charges were able to transfer more efficiently from the $BiVO_4$ surface to the Ni-Mo, than from the Al_2O_3 overlayer to the Ni-Mo. This very important interface needs to be further examined and optimized.

Chapter 5

Conclusion and future directions

Photoelectrochemical (PEC) water splitting is a direct way of producing a solar fuel like hydrogen from water. The bottleneck of this process is the photoanode which is responsible for the water oxidation side of the reaction[1,2]. Semiconductor metal oxides are preferred catalysts for this reaction because of their stability under oxidizing conditions and being generally low-cost. However, no single catalyst can fulfil all the requirements for an efficient water oxidation reaction. There are always trade-offs among the light-harvesting ability, the charge transport and charge transfer processes, and the catalyst's influence in the kinetics of the reaction.

In this work, the use of $BiVO_4$ as a photoanode was extensively studied in order to improve its photoactivity. $BiVO_4$ has a conduction band edge position that almost coincides with the thermodynamic hydrogen evolution potential, thus, it can promote an earlier photocurrent onset, and can generate a higher photocurrent in the low bias region compared to the other photoanodes. These properties are vital in obtaining a high overall operating current and can eventually lead to a higher STH efficiency. In addition, $BiVO_4$ has a relatively low band gap energy of 2.4-2.5 eV, which makes it readily absorb visible light[3]. Its theoretical maximum photocurrent density is 7.5 mA/cm^2[143]. However, the drawbacks of using $BiVO_4$ photoanodes are poor electron mobility and poor water oxidation kinetics. Poor electron mobility brings about the loss of the photon efficiency to electron-hole recombination[4]. Moreover, $BiVO_4$ is not a good water oxidation catalyst.

Highlights

The optimization of $BiVO_4$ photoanode synthesis via thin film electrodeposition on FTO was performed. The factors affecting the

photoelectrochemical activity such as the electrodeposition time, ratio of the Bi-KI to benzoquinone-EtOH in the deposition bath, and the calcination temperature, have been investigated by using the Central Composite Design of Experiments. Pristine monoclinic scheelite $BiVO_4$ photoanodes having a photocurrent density of 0.45 ± 0.05mA/cm^2 at 1.23 V vs RHE have been obtained. It was shown that a high photocurrent density are generally dictated by the following physico-chemical properties: higher crystallite size, an optimal thickness, and a more compact, porous morphology. Furthermore, the following photoelectrochemical characteristics give rise to a higher photocurrent density: low onset potential, and a high donor density.

The nature of the $BiVO_4$ surface was studied. The existence of surface hydroxyl groups on $BiVO_4$ was confirmed and quantified (max 1.5 OH/nm^2) via chemical titration. The reaction of the $BiVO_4$ powder with one pulse of $AlMe_3$ and 1 pulse of H_2O showed that there were 1.2 molecules of CH_4 evolved per Bi-OH.

Surface states on the $BiVO_4$ surface give rise to defect levels, which can mediate electron-hole recombination via the Shockley-Read-Hall mechanism[5]. In order to minimize the inefficiencies due to electron-hole recombination and passivate the surface states, ultrathin overlayers of Al_2O_3 and TiO_2 were deposited to the $BiVO_4$ thin film electrodes in an ALD-like manner. This was also performed in order to protect the $BiVO_4$ surface from photocorrosion and increase its stability. A photocurrent density of 0.54 mA/cm^2 at 1.23 V vs RHE was obtained for the Al_2O_3-modified $BiVO_4$, which was a 54% improvement from the bare $BiVO_4$ that demonstrated a photocurrent density of 0.35 mA/cm^2 at 1.23 V vs RHE. A 15% increase in stability of the Al_2O_3- modified $BiVO_4$ electrode was also observed over 7.5 hours of continuous irradiation. Moreover, through surface capacitance measurements, it was shown that the Al_2O_3 overlayer was indeed passivating the surface states of the $BiVO_4$ electrodes. Meanwhile, there were no photocurrent density improvements that were observed for the TiO_2-modified $BiVO_4$ at the synthesis conditions that were used in this experiment.

The addition of Ni-Mo to bare $BiVO_4$ increases the photocurrent density by 3-fold, from 0.35 mA/cm^2 to 1 mA/cm^2 at 1.23 V vs RHE. This was mainly due to the much lower charge transfer resistance of this electrode with respect to bare $BiVO_4$. Moreover, the addition of Ni-Mo to $BiVO_4$ with an overlayer of 2 cycles of Al_2O_3 produces a photocurrent density (0.39 mA/cm^2 at 1.23 V vs RHE) that is lower than that of just $BiVO_4$ with Ni-Mo, and slightly higher than that of the bare $BiVO_4$ for potentials up to 1.3 V vs RHE. It is apparent that the charges were able to transfer more efficiently from the $BiVO_4$ surface to the Ni-Mo, than from the Al_2O_3 overlayer to the Ni-Mo. This very important interface needs to be further examined and optimized.

Future Directions

Electrodeposited $BiVO_4$ photoanodes provide a promising synthesis route for large-scale applications, but the photoanodes that were synthesized here were not transparent. In order to be useful as light absorbers in tandem cell devices, the $BiVO_4$ photoanode has to be transparent, thus, the control of the thickness and growth of the material is very important.

The effect of the operating temperature on the performance of the photoanodes should be investigated. Our preliminary tests indicate that this plays a huge role in the resulting performance.

Although the addition of passivation layers improved the stability of the thin film electrodes that were reported in this study, this is still far from being sufficient to support practical applications. In order to be practical, PEC water splitting systems have to be stable for a long period of time, the typical benchmark being a lifetime of 10 years[120].

References

(1) Hurst, J. K. *Science* **2010**, *328* (April1 J. K. Hurst, Science (80-.)., 2010, 328, 315–316.), 315–316.
(2) Grätzel, M.; Moser, J. **2001**, *5*, 589–644.
(3) Kudo, A.; Ueda, K.; Kato, H.; Mikami, I. **1998**, *53*, 229–230.
(4) Ma, Y.; Pendlebury, S. R.; Reynal, A.; le Formal, F.; Durrant, J. R. *Chemical Science* **2014**, *5* (8), 2964.
(5) Bonilla, R. S.; Hoex, B.; Hamer, P.; Wilshaw, P. R. **2017**, *214* (7).
(6) Contribution of Working Groups I, II and III to the Fifth Assessment Report of the Intergovernmental Panel on Climate Change [Core Writing Team, R. K. P. and L. A. M. (eds.). *IPCC Fifth Assessment Report* **2014**, 151.
(7) van de Krol, R.; Grätzel, M. *Photoelectrochemical Hydrogen Production*; 2012.
(8) Pinaud, B. A.; Benck, J. D.; Seitz, L. C.; Forman, A. J.; Chen, Z.; Deutsch, T. G.; James, B. D.; Baum, K. N.; Baum, G. N.; Ardo, S.; Wang, H.; Miller, E.; Jaramillo, T. F. *Energy & Environmental Science* **2013**, *6* (7), 1983–2002.
(9) Fujishima, A.; Honda, K. *Nature* **1972**, *238* (5358), 37–38.
(10) Gray, H. B. *Nature chemistry* **2009**, *1* (1), 7.
(11) Chen, Z.; Dinh, H. N.; Miller, E. *Photoelectrochemical Water Splitting*; 2013.
(12) Walter, M. G.; Warren, E. L.; McKone, J. R.; Boettcher, S. W.; Mi, Q.; Santori, E. A.; Lewis, N. S. *Chemical Reviews (Washington, DC, United States)* **2010**, *110* (11), 6446–6473.
(13) Inoue, H.; Shimada, T.; Kou, Y.; Nabetani, Y.; Masui, D.; Takagi, S.; Tachibana, H. *ChemSusChem* **2011**, *4* (2), 173–179.
(14) Wang, M.; Artero, V.; Hammarstr, L.; Martinez, J.; Karlsson, J.; Gust, D.; Summers, P.; Machan, C.; Brueggeller, P.; Windle, C. D.; Kageshima, Y.; Cogdell, R.; Tolod, K. R.; Kibler, A.; Apaydin, D. H.; Fujita, E.; Ehrmaier, J.; Shima, S.; Gibson, E.; Karadas, F.; Harriman, A.; Inoue, H.; Kudo, A.; Takayama, T.; Wasielewski, M.; Cassiola, F.; Yagi, M.; Ishida, H.; Franco, F.; Park, H.; Sun, L.; Setoyama, T.; Kang, Y. S. **2017**, 353–395.
(15) Kumagai, H.; Hammarstr, L.; Whang, D. R.; Shinohara, Y.; Martinez, J.; Karlsson, J.; Summers, P.; Windle, C. D.; Kodera, M.; Cogdell, R.; Tolod, K. R.; Apaydin, D. H.; Fujita, E.; Kibler, A.; Fan, F.; Gibson, E. A.; Usami, H.; Iwase, A.; Inoue, H.; Kudo, A.; Gust, D.; Yamakata, A.; Li, C.; Sun, L.; Park, H. **2017**, 481–507.
(16) Sivula, K.; Formal, F. Le; Grätzel, M. **2011**, 432–449.
(17) Cherepy, N. J.; Liston, D. B.; Lovejoy, J. A.; Deng, H.; Zhang, J. Z. **1998**, *5647* (97), 770–776.
(18) Kennedy, J. H.; Frese, K. W. **1978**, *125* (5), 709–714.
(19) Dare-Edwards, M. P.; Goodenough, J. B.; Hamnett, A.; Trevellick, P. R. **1983**, No. 1, 2027–2041.
(20) Press, S. P.; Britain, G. **1963**, *24*, 1183–1196.
(21) Chen, S.; Wang, L. W. *Chemistry of Materials* **2012**, *24* (18), 3659–3666.
(22) Butler, M. A. **2008**, *1914* (August).
(23) Kafizas, A.; Franca, L.; Sotelo-vazquez, C.; Ling, M.; Li, Y.; Glover, E.;

Mcca, L.; Blackman, C.; Darr, J.; Parkin, I. *The Journal of Physical Chemistry C* **2017**, *121*, 5.
(24) Steier, L.; Herraiz-cardona, I.; Gimenez, S.; Fabregat-santiago, F.; Bisquert, J.; Tilley, S. D.; Grätzel, M. **2014**.
(25) Sivula, K.; Florian, B.; Formal, L.; Gra, M. **2010**, 1099–1107.
(26) Abdi, F. F.; Han, L.; Smets, A. H. M.; Zeman, M.; Dam, B.; van de Krol, R. *Nature Communications* **2013**, *4*, 1–7.
(27) Mohamed, E. A.; Zahran, Z. N.; Naruta, Y. *Journal of Materials Chemistry A: Materials for energy and sustainability* **2017**, *5*, 6825–6831.
(28) Zheng, H.; Ou, J. Z.; Strano, M. S.; Kaner, R. B.; Mitchell, A. **2011**, 2175–2196.
(29) Tacca, A.; Meda, L.; Marra, G.; Savoini, A.; Caramori, S.; Cristino, V.; Bignozzi, A.; Pedro, G.; Boix, P. P. **2012**, 3025–3034.
(30) Liu, Y.; Li, J.; Li, W.; Yang, Y.; Li, Y.; Chen, Q. **2015**.
(31) Liu, Y.; Li, Q.; Gao, S.; Shang, J. K. **2014**, 7493–7501.
(32) Seabold, J. A.; Choi, K. **2011**, 1105–1112.
(33) Lim, A. R.; Choh, S. H.; Jang, M. S. *Journal of Physics: Condensed Matter* **1995**, *7* (37), 7309–7323.
(34) Martinez Suarez, C.; Hernández, S.; Russo, N. *Applied Catalysis A: General* **2015**, *504*, 158–170.
(35) Kim, T. W.; Choi, K.-S. **2014**, *343* (February), 990–995.
(36) Cooper, J. K.; Gul, S.; Toma, F. M.; Chen, L.; Glans, P.-A.; Guo, J.; Ager, J. W.; Yano, J.; Sharp, I. D. *Chemistry of Materials* **2014**, *26* (18), 5365–5373.
(37) Abdi, F. F.; Firet, N.; vandeKrol, R. *ChemCatChem* **2013**, *5* (2), 490–496.
(38) Abdi, F. F.; Savenije, T. J.; May, M. M.; Dam, B.; Krol, R. Van De. *J. Phys. Chem. Lett.* **2013**, *4*, 2752–2757.
(39) Rettie, A. J. E.; Lee, H. C.; Marshall, L. G.; Lin, J.-F.; Capan, C.; Lindemuth, J.; McCloy, J. S.; Zhou, J.; Bard, A. J.; Mullins, C. B. *Journal of the American Chemical Society* **2013**, *135* (30), 11389–11396.
(40) Seabold, J. A.; Zhu, K.; Neale, N. R. *Phys. Chem. Chem. Phys.* **2014**, *16* (3), 1121–1131.
(41) Roth, R.; Waring, J. *The American Mineralogist* **1963**, *18*, 1348–1356.
(42) Bhattacharya, a K. *Materials Letters* **1997**, *30* (January), 7–13.
(43) Walsh, A.; Yan, Y.; Huda, M. N.; Al-Jassim, M. M.; Wei, S.-H. H. *Chemistry of Materials* **2009**, *21* (3), 547–551.
(44) Cooper, J. K.; Gul, S.; Toma, F. M.; Chen, L.; Glans, P.-A.; Guo, J.; Ager, J. W.; Yano, J.; Sharp, I. D. *Chemistry of Materials* **2014**, *26* (18), 5365–5373.
(45) Payne, D. J.; Robinson, M. D. M.; Egdell, R. G.; Walsh, A.; McNulty, J.; Smith, K. E.; Piper, L. F. J. *Applied Physics Letters* **2011**, *98* (21), 46–49.
(46) Kudo, A.; Omori, K.; Kato, H. **1999**, No. 14, 11459–11467.
(47) Park, Y.; McDonald, K. J.; Choi, K.-S. *Chemical Society Reviews* **2013**, 2321–2337.
(48) Kim, T. W.; Ping, Y.; Galli, G. A.; Choi, K.-S. *Nature Communications* **2015**, *6*, 8769.
(49) Kronawitter, C. X.; Vayssieres, L.; Shen, S.; Guo, L.; Wheeler, D. a.; Zhang, J. Z.; Antoun, B. R.; Mao, S. S. *Energy & Environmental Science* **2011**, *4* (10), 3889.
(50) Cho, S.; Jang, J. W.; Lee, K. H.; Lee, J. S. *APL Materials* **2014**, *2* (1).
(51) Sinclair, T. S.; Hunter, B. M.; Winkler, J. R.; Gray, H. B.; Astrid, M. M.

2015, 22–24.
(52) Zhou, M.; Bao, J.; Xu, Y.; Zhang, J.; Xie, J.; Guan, M.; Wang, C.; Wen, L.; Lei, Y.; Xie, Y. *ACS Nano* **2014**, *8* (7), 7088–7098.
(53) Nair, V.; Perkins, C. L.; Lin, Q.; Law, M. *Energy Environ. Sci.* **2016**, *9* (4), 1412–1429.
(54) Han, H. S.; Shin, S.; Kim, D. H.; Park, I. J.; Kim, J. S.; Huang, P.-S.; Lee, J.-K.; Cho, I. S.; Zheng, X. *Energy & Environmental Science* **2018**, 1299–1306.
(55) Kim, T. W.; Choi, K.-S. *Science* **2014**, *343* (6174), 990–994.
(56) McDonald, K. J.; Choi, K.-S. *Energy & Environmental Science* **2012**, *5* (9), 8553.
(57) Pihosh, Y.; Turkevych, I.; Mawatari, K.; Uemura, J.; Kazoe, Y.; Kosar, S.; Makita, K.; Sugaya, T.; Matsui, T.; Fujita, D.; Tosa, M.; Kondo, M.; Kitamori, T. *Scientific Reports* **2015**, *5* (February), 11141.
(58) Oliveira, A. T.; Rodriguez, M.; Andrade, T. S.; de Souza, H. E. A.; Ardisson, J. D.; Oliveira, H. S.; Oliveira, L. C. A.; Lorençon, E.; Silva, A. C.; Nascimento, L. L.; Patrocínio, A. O. T.; Pereira, M. C. *Solar RRL* **2018**, *1800089*, 1800089.
(59) Qiu, Y.; Liu, W.; Chen, W.; Chen, W.; Zhou, G.; Hsu, P.-C.; Zhang, R.; Liang, Z.; Fan, S.; Zhang, Y.; Cui, Y. *Science Advances* **2016**, *2* (6), e1501764.
(60) Shi, X.; Choi, I. Y.; Zhang, K.; Kwon, J.; Kim, D. Y.; Lee, J. K.; Oh, S. H.; Kim, J. K.; Park, J. H. *Nature communications* **2014**, *5*, 4775.
(61) Mohamed, E. A.; Zahran, Z. N.; Naruta, Y. *J. Mater. Chem. A* **2017**, *5* (15), 6825–6831.
(62) Kim, J. H.; Jo, Y.; Kim, J. H.; Jang, J. W.; Kang, H. J.; Lee, Y. H.; Kim, D. S.; Jun, Y.; Lee, J. S. 1–27.
(63) Shi, X.; Zhang, K.; Shin, K.; Ma, M.; Kwon, J.; Choi, I. T.; Kim, J. K.; Kim, H. K.; Wang, D. H.; Park, J. H. *Nano Energy* **2015**, *13*, 182–191.
(64) Kim, J. H.; Jang, J. W.; Kang, H. J.; Magesh, G.; Kim, J. Y.; Kim, J. H.; Lee, J.; Lee, J. S. *Journal of Catalysis* **2014**, *317*, 126–134.
(65) Wang, D.; Li, R.; Zhu, J.; Shi, J.; Han, J.; Zong, X.; Li, C. **2012**.
(66) Park, Y.; Kang, D.; Choi, K.-S. *Physical Chemistry Chemical Physics* **2014**, *16* (3), 1238–1246.
(67) Kanan, M. W.; Nocera, D. G. *Science (New York, N.Y.)* **2008**, *321* (5892), 1072–1075.
(68) Lutterman, D. A.; Surendranath, Y.; Nocera, D. G. *Journal of the American Chemical Society* **2009**, *131* (11), 3838–3839.
(69) Zhong, D. K.; Choi, S.; Gamelin, D. R. *Journal of the American Chemical Society* **2011**, *133*, 18370–18377.
(70) Pilli, S. K.; Furtak, T. E.; Brown, L. D.; Deutsch, T. G.; Turner, J. A.; Herring, A. M. *Energy & Environmental Science* **2011**, *4* (12), 5028.
(71) Zhong, M.; Hisatomi, T.; Kuang, Y.; Zhao, J.; Liu, M.; Iwase, A.; Jia, Q.; Nishiyama, H.; Minegishi, T.; Nakabayashi, M.; Shibata, N.; Niishiro, R.; Katayama, C.; Shibano, H.; Katayama, M.; Kudo, A.; Yamada, T.; Domen, K. *Journal of the American Chemical Society* **2015**, *137* (15), 5053–5060.
(72) Joya, K. S.; Takanabe, K.; De Groot, H. J. M. *Advanced Energy Materials* **2014**, *4* (16), 2–7.
(73) Kim, J. H.; Magesh, G.; Kang, H. J.; Banu, M.; Kim, J. H.; Lee, J.; Lee, J. S. *Nano Energy* **2015**, *15*, 153–163.
(74) Mccrory, C. C. L.; Jung, S.; Peters, J. C.; Jaramillo, T. F. 1–32.

(75) McCrory, C. C. L.; Jung, S.; Ferrer, I. M.; Chatman, S. M.; Peters, J. C.; Jaramillo, T. F. *Journal of the American Chemical Society* **2015**, *137* (13), 4347–4357.
(76) Pickrahn, K. L.; Park, S. W.; Gorlin, Y.; Lee, H.-B.-R.; Jaramillo, T. F.; Bent, S. F. *Advanced Energy Materials* **2012**, *2* (10), 1269–1277.
(77) Jia, Q.; Iwashina, K.; Kudo, A. *Pnas* **2012**, *109* (29), 11564–11569.
(78) Ma, M.; Kim, J. K.; Zhang, K.; Shi, X.; Kim, S. J.; Moon, J. H.; Park, J. H. **2014**.
(79) Hernández, S.; Gerardi, G.; Bejtka, K.; Fina, A.; Russo, N. *Applied Catalysis B: Environmental* **2016**, *190*, 66–74.
(80) Thalluri, S. M.; Rojas, R. M.; Rivera, O. D.; Hernandez, S.; Russo, N.; Rodil, S. E. *Physical Chemistry Chemical Physics* **2015**, *17* (27), 17821–17827.
(81) Thalluri, S. M.; Martinez Suarez, C.; Hernández, S.; Bensaid, S.; Saracco, G.; Russo, N. *Chemical Engineering Journal* **2014**, *245*, 124–132.
(82) Hernández, S.; Thalluri, S. M.; Sacco, A.; Bensaid, S.; Saracco, G.; Russo, N. *Applied Catalysis A: General* **2015**, *504*, 266–271.
(83) Berglund, S. P.; Rettie, A. J. E.; Hoang, S.; Mullins, C. B. **2012**, 7065–7075.
(84) Luo, W.; Li, Z.; Yu, T.; Zou, Z. *Journal of Physical Chemistry C* **2012**, *116* (8), 5076–5081.
(85) Park, H. S.; Kweon, K. E.; Ye, H.; Paek, E.; Hwang, G. S. **2011**, 1–5.
(86) Jo, W. J.; Jang, J. W.; Kong, K. J.; Kang, H. J.; Kim, J. Y.; Jun, H.; Parmar, K. P. S.; Lee, J. S. *Angewandte Chemie - International Edition* **2012**, *51* (13), 3147–3151.
(87) Parmar, K. P. S.; Kang, H. J.; Bist, A.; Dua, P.; Jang, J. S.; Lee, J. S. *ChemSusChem* **2012**, *5* (10), 1926–1934.
(88) Luo, W.; Yang, Z.; Li, Z.; Zhang, J.; Liu, J.; Zhao, Z.; Wang, Z.; Yan, S.; Yu, T.; Zou, Z. *Energy & Environmental Science* **2011**, *4* (10), 4046.
(89) Jeong, H. W.; Jeon, T. H.; Jang, J. S.; Choi, W.; Park, H. *The Journal of Physical Chemistry C* **2013**, *117* (18), 9104–9112.
(90) He, H.; Berglund, S. P.; Rettie, A. J. E.; Chemelewski, W. D.; Xiao, P.; Zhang, Y.; Mullins, C. B. *Journal of Materials Chemistry A* **2014**, *2* (24), 9371–9379.
(91) Yao, W.; Iwai, H.; Ye, J. *Dalton transactions (Cambridge, England : 2003)* **2008**, No. 11, 1426–1430.
(92) Thalluri, S. M.; Hernández, S.; Bensaid, S.; Saracco, G.; Russo, N. *Applied Catalysis B: Environmental* **2016**, *180*, 630–636.
(93) Thalluri, S. M.; Martinez Suarez, C.; Hussain, M.; Hernandez, S.; Virga, A.; Saracco, G.; Russo, N. *Industrial & Engineering Chemistry Research* **2013**, *52*, 17414–17418.
(94) Pattengale, B.; Ludwig, J.; Huang, J. *The Journal of Physical Chemistry C* **2016**, acs.jpcc.5b11451.
(95) Gong, H.; Freudenberg, N.; Nie, M.; Van De Krol, R.; Ellmer, K. *AIP Advances* **2016**, *6* (4).
(96) Kim, J. H.; Jo, Y.; Kim, J. H.; Jang, J. W.; Kang, H. J.; Lee, Y. H.; Kim, D. S.; Jun, Y.; Lee, J. S.; Al, K. I. M. E. T. *Nano* **2015**, No. 12, 11820–11829.
(97) Monfort, O.; Pop, L.; Sfaelou, S.; Plecenik, T.; Roch, T.; Dracopoulos, V.; Stathatos, E.; Plesch, G.; Lianos, P. **2016**, *286*, 91–97.
(98) Wang, H.; Zhang, L.; Chen, Z.; Hu, J.; Li, S.; Wang, Z.; Liu, J.; Wang, X. *Chemical Society reviews* **2014**, *43* (15), 5234–5244.
(99) Su, J.; Guo, L.; Bao, N.; Grimes, C. a. *Nano letters* **2011**, *11* (5), 1928–1933.
(100) Murcia-López, S.; Fàbrega, C.; Monllor-Satoca, D.; Hernández-Alonso, M.

D.; Penelas-Pérez, G.; Morata, A.; Morante, J. R.; Andreu, T. *ACS Applied Materials and Interfaces* **2016**, *8* (6), 4076–4085.
(101) Zhang, L.; Reisner, E.; Baumberg, J. J. *Energy & Environmental Science* **2014**, *7* (4), 1402.
(102) Pilli, S. K.; Deutsch, T. G.; Furtak, T. E.; Brown, L. D.; Turner, J. a; Herring, A. M. *Physical Chemistry Chemical Physics* **2013**, *15*, 3273–3278.
(103) Shi, X.; Jeong, H.; Oh, S. J.; Ma, M.; Zhang, K.; Kwon, J.; Choi, I. T.; Choi, I. Y.; Kim, H. K.; Kim, J. K.; Park, J. H. *Nature Communications* **2016**, *7* (May), 11943.
(104) Rao, P. M.; Cai, L.; Liu, C.; Cho, I. S.; Lee, C. H.; Weisse, J. M.; Yang, P.; Zheng, X. *Nano Letters* **2014**, *14* (2), 1099–1105.
(105) Field, S. **2005**, No. June.
(106) Tolod, K.; Hernández, S.; Russo, N. *Catalysts* **2017**, *7* (1), 13.
(107) Filatova, E. O.; Konashuk, A. S. **2015**.
(108) Dingemans, G.; Beyer, W.; Sanden, M. C. M. Van De; Kessels, W. M. M. **2012**, *152106* (2010), 1–4.
(109) Chang, G.; Zhang, D. W. Y.; Aldalbahi, A. *Nuclear Science and Techniques* **2016**, 2–7.
(110) Kafizas, A.; Xing, X.; Selim, S.; Mesa, C. A.; Ma, Y.; Burgess, C.; McLachlan, M. A.; Durrant, J. R. *Catalysis Today* **2017**, No. July.
(111) Thomson, A. F.; Mcintosh, K. R. **2012**, No. July 2011, 343–349.
(112) Jo, W. J.; Jang, J.; Kong, K.; Kang, H. J.; Kim, J. Y.; Jun, H.; Parmar, K. P. S.; Lee, J. S. **2012**, 3147–3151.
(113) Zhao, J.; Guo, Y.; Cai, L.; Li, H.; Wang, K. X.; Cho, I. S.; Lee, C. H.; Fan, S.; Zheng, X. *ACS Energy Letters* **2016**, *1*, 68–75.
(114) Yu, J.; Kudo, A. *Advanced Functional Materials* **2006**, *16* (16), 2163–2169.
(115) Chen, L.; Toma, F. M.; Cooper, J. K.; Lyon, A.; Lin, Y.; Sharp, I. D.; Ager, J. W. **2015**, 1066–1071.
(116) Alarco, E.; Chen, L.; Hettick, M.; Mashouf, N.; Lin, Y.; Ager, J. W. **2014**, 1651–1657.
(117) Wang, G.; Ling, Y.; Lu, X.; Qian, F.; Tong, Y.; Zhang, J. Z.; Lordi, V.; Rocha Leao, C.; Li, Y. *Journal of Physical Chemistry C* **2013**, *117* (21), 10957–10964.
(118) Kho, Y. K.; Teoh, W. Y.; Iwase, A.; Mädler, L.; Kudo, A.; Amal, R. *ACS Applied Materials and Interfaces* **2011**, *3* (6), 1997–2004.
(119) Ganduglia-Pirovano, M. V.; Hofmann, A.; Sauer, J. *Surface Science Reports* **2007**, *62* (6), 219–270.
(120) Bard, A. J.; Fox, M. A. *Acc. Chem. Res* **1995**, *28*, 141–145.
(121) Toma, F. M.; Cooper, J. K.; Kunzelmann, V.; McDowell, M. T.; Yu, J.; Larson, D. M.; Borys, N. J.; Abelyan, C.; Beeman, J. W.; Yu, K. M.; Yang, J.; Chen, L.; Shaner, M. R.; Spurgeon, J.; Houle, F. A.; Persson, K. A.; Sharp, I. D. *Nat Commun* **2016**, *7* (May), 12012.
(122) Dall'Antonia, L. H.; de Tacconi, N. R.; Chanmanee, W.; Timmaji, H.; Myung, N.; Rajeshwar, K. *Electrochemical and Solid-State Letters* **2010**, *13* (5), D29.
(123) Rossell, M. D.; Agrawal, P.; Borgschulte, A.; Hébert, C.; Passerone, D.; Erni, R. *Chemistry of Materials* **2015**, *27* (10), 3593–3600.
(124) Wang, S.; Chen, P.; Bai, Y.; Yun, J. H.; Liu, G.; Wang, L. *Advanced Materials* **2018**, *30* (20), 1–7.
(125) Wu, J.; Chen, Y.; Pan, L.; Wang, P.; Cui, Y.; Kong, D.; Wang, L.; Zhang, X.; Zou, J. *Applied Catalysis B: Environmental* **2018**, *221* (August 2017),

187–195.
(126) Silversmit, G.; Depla, D.; Poelman, H.; Marin, G. B.; Gryse, R. De. **2004**, No. April.
(127) Zhang, Y.; Guo, Y.; Duan, H.; Li, H.; Sun, C. *Phys. Chem. Chem. Phys.* **2014**, *16*, 24519–24526.
(128) Sayama, K.; Nomura, A.; Arai, T.; Sugita, T.; Abe, R.; Oi, T.; Iwasaki, Y.; Abe, Y.; Sugihara, H. *The Journal of Physical Chemistry B* **2006**, *3*, 11352–11360.
(129) Passerone, D.; Erni, R. **2015**.
(130) Banerjee, A. N.; Kundoo, S.; Saha, P.; Chattopadhyay, K. K. *Journal of Sol-Gel Science and Technology* **2003**, *28* (1), 105–110.
(131) Gim, S.; Bisquert, J.; Principles, F. B.; Devices, A. *Photoelectrochemical Solar Fuel Production*; 2016.
(132) Copéret, C.; Comas-Vives, A.; Conley, M. P.; Estes, D. P.; Fedorov, A.; Mougel, V.; Nagae, H.; Nunez-Zarur, F.; Zhizhko, P. A. *Chemical Reviews* **2016**, *116*, 323–421.
(133) Gittleson, F. S.; Yao, K. P. C.; Kwabi, D. G.; Sayed, S. Y.; Ryu, W. H.; Shao-Horn, Y.; Taylor, A. D. *ChemElectroChem* **2015**, *2* (10), 1446–1457.
(134) Hatzenbuhler, D. a. *The Journal of Chemical Physics* **1972**, *56* (1972), 3398.
(135) Zhao, Z.; Li, Z.; Zou, Z. *RSC Advances* **2011**, *1* (5), 874–883.
(136) Groner, M. D.; Fabreguette, F. H.; Elam, J. W.; George, S. M. **2004**, No. 16, 639–645.
(137) Kerber, R. N.; Kermagoret, A.; Callens, E.; Florian, P.; Massiot, D.; Lesage, A.; Copéret, C.; Delbecq, F.; Rozanska, X.; Sautet, P. *Journal of the American Chemical Society* **2012**, *134* (15), 6767–6775.
(138) Yin, C.; Zhu, S.; Chen, Z.; Zhang, W.; Gu, J.; Zhang, D. *Journal of Materials Chemistry A* **2013**, *1* (29), 8367–8378.
(139) Zachäus, C.; Abdi, F. F.; Peter, L. M.; Van De Krol, R. *Chemical Science* **2017**, *8* (5), 3712–3719.
(140) McKone, J. R.; Marinescu, S. C.; Brunschwig, B. S.; Winkler, J. R.; Gray, H. B. *Chemical Science* **2014**, *5* (3), 865–878.
(141) McKone, J. R.; Sadtler, B. F.; Werlang, C. A.; Lewis, N. S.; Gray, H. B. *ACS Catalysis* **2013**, *3* (2), 166–169.
(142) Marzun, G.; Levish, A.; Mackert, V.; Kallio, T.; Barcikowski, S.; Wagener, P. *Journal of Colloid and Interface Science* **2017**, *489*, 57–67.
(143) Hu, S.; Xiang, C.; Haussener, S.; Berger, A. D.; Lewis, N. S. *Energy & Environmental Science* **2013**, *6* (10), 2984–2993.

Appendices

Appendix 1

Preliminary experiments for factor screening

Initially, 6 factors have been identified and preliminarily screened in order to identify the significant factors to be subjected to design of experiments. The factors that were investigatedwere: potential, electrodeposition time, Bi-KI to benzoquinone-ethanol ratio, V precursor solvent, calcination temperature and ramp rate.

A1.1 Effect of Potential

With all other factors held constant, the effect of potential (-0.05V to -2Vvs Ag/AgCl (3M KCl)) was investigated. Electrodeposition time was set at 3 min and Bi-KI to benzoquinone-ethanol ratio of 2.5.

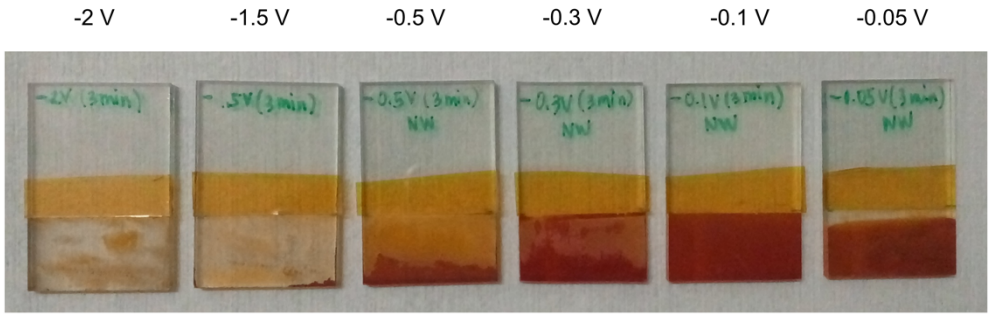

Figure A1. Electrodeposition with varying potentials

As seen in Figure A1, deposition was accomplished with a uniform coverage of the electrode at a potential of -0.1Vvs Ag/AgCl (3M KCl). Depositing at higher potentials did not yield a film that adhered to the FTO surface while using a lower potential did not entirely cover the set electrodeposition area. For this reason, the applied potential was fixed at -0.1Vvs Ag/AgCl (3M KCl) for the experimental runs.

A1.2 Effect of electrodeposition time

Varying the electrodeposition time varies the thickness of electrodeposited films, as shown in Figure A2.

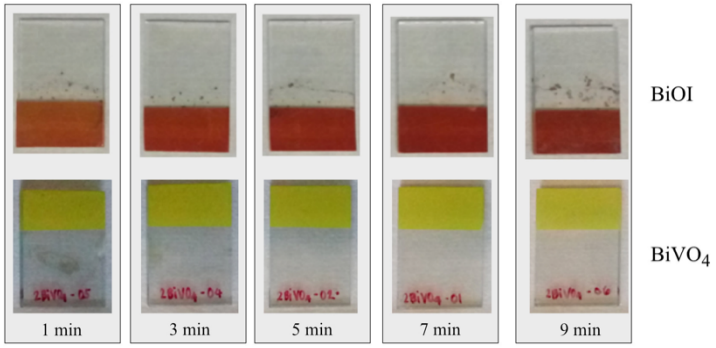

Figure A2. Electrodeposited BiOI (TOP) and synthesized $BiVO_4$ (BOTTOM) at different electrodeposition times, (Bi-KI to benzoquinone-ethanol ratio at 2.5 and the calcination temperature of 450ºC)

For the design of experiments, a wider range of electrodeposition time, from 0.5 min to 10 min, has been considered.

A1.3 Effect of the Bi-KI to Benzoquinone-ETOH ratio

The electrodeposition of BiOI onto the FTO glass is made possible by the reduction of p-benzoquinone to hydroquinone. The p-benzoquinone consumes H^+ in the solution during the process, which results in a local pH increase enabling the precipitation of BiOI on the FTO glass working electrode.[55]

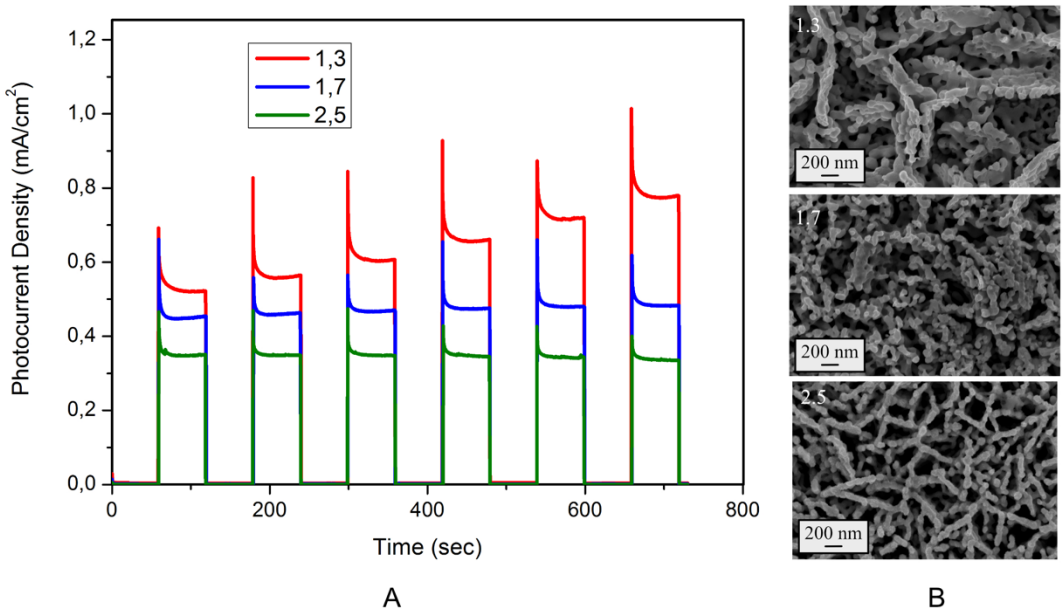

Figure A3. Water oxidation activity results by varying the Bi-KI to benzoquinone-EtOH ratio. (A) Chronoamperometry plots of the photocurrent density and the (B) corresponding FE-SEM images, (electrodeposition time of 3 minutes and calcination temperature of 450 ºC)

The ratios investigated for the Bi-KI to benzoquinone-ethanol are 1.3 to 2.5 because differences in morphology were observed among the samples synthesized at different ratios in the preliminary tests. At a ratio of 1, no deposition was observed.

A1.4 Effect of the Vanadium precursor solvent

Two V precursor solvents were intially used. The photocurrent densities obtained using DMSO (dimethyl sulfoxide) were slightly higher than those using DMF (dimethylfuran). For this reason and due to the safety considerations, the V precursor solvent chosen was DMSO.

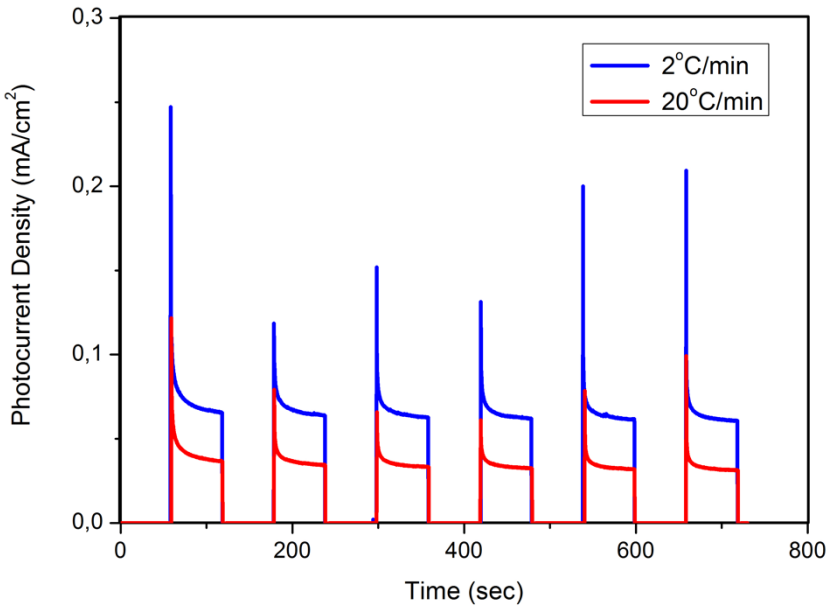

Figure A4. Chronoamperometry plot showing the effect of the Vanadium precursor solvent on the photocurrent density (electrodeposition time of 3 minutes and calcination temperature of 450°C)

A1.5 Effect of the calcination temperature

Significant morphology changes as well as different grain sizes were observed upon calcination at the temperature range of 350°C to 500°C. This was the same range that was employed in the design of experiments.

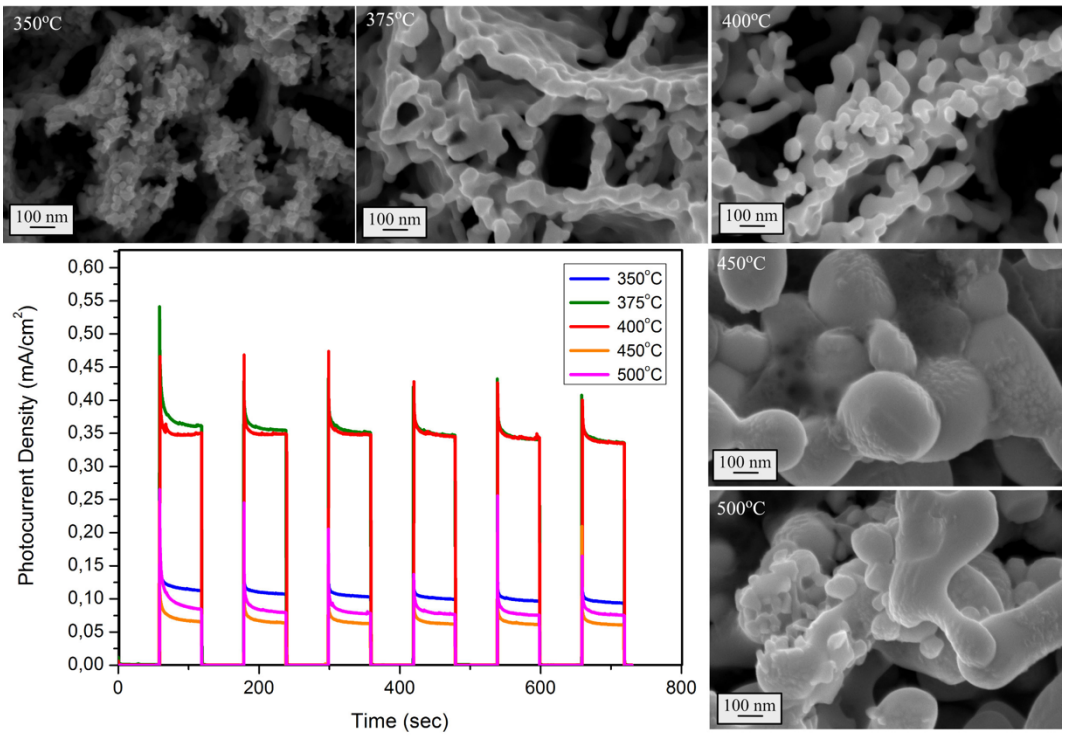

Figure A5. Chronoamperometry plot showing the effect of calcination temperature on the photocurrent density and the resulting morphologies, as shown by the FE-SEM images (electrodeposition time of 3 minutes and Bi-KI to benzoquinone-EtOH ratio of 2.5)

A1.6 Effect of the calcination heating rate

A fast (20°C) and slow (2°C) ramp rate were preliminarily tested to identify the effect of heating rate during calcination on the morphology and photocurrent density of the material. Based on preliminary tests, a slower ramp rate is preferred, thus, the heating rate was fixed to 2°C/min.

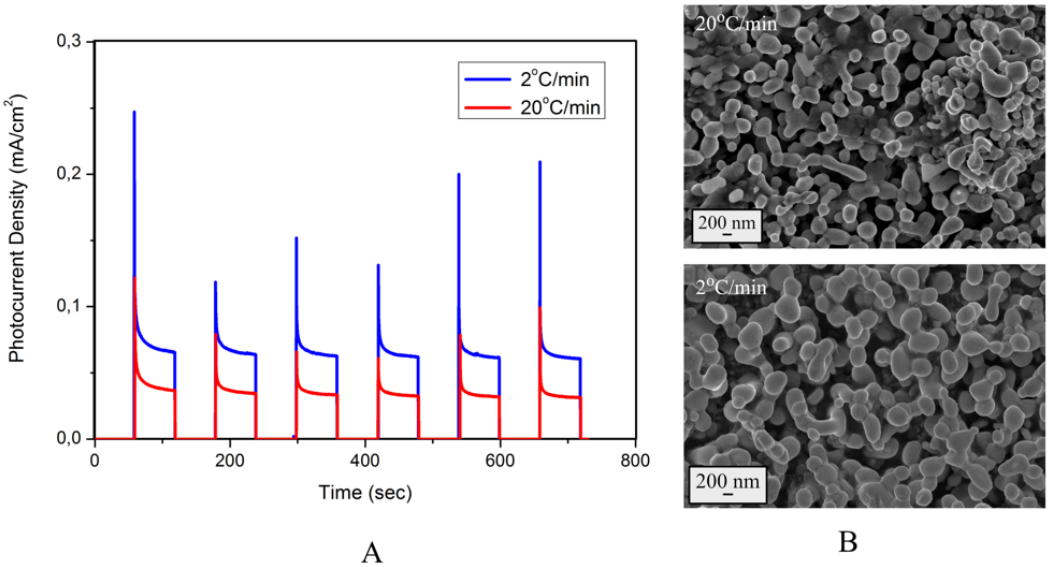

Figure A6. Water oxidation activity results by varying calcination heating/ramp rate. (A) Chronoamperometry plot showing the photocurrent density and the (B) corresponding FE-SEM images, (electrodeposition time of 3 minutes and calcination temperature of 450 °C)

Appendix 2

UV-vis diffuse reflectance spectra

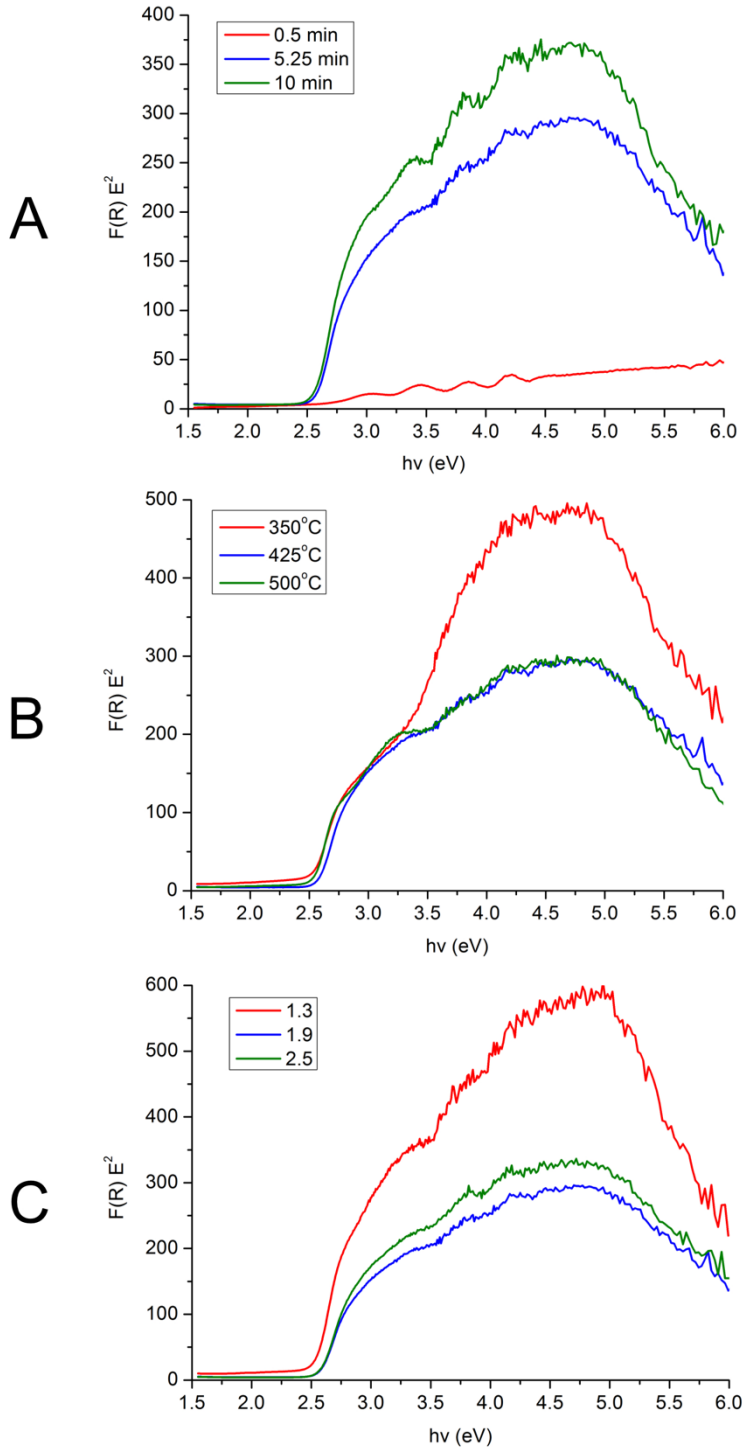

Figure A7.Kubelka-Munk function versus photon energy at various (A) electrodeposition time, (B) calcination temperature, and (C) Bi-KI to benzoquinone-EtOH ratio

Appendix 3

Mott-Schottky plots

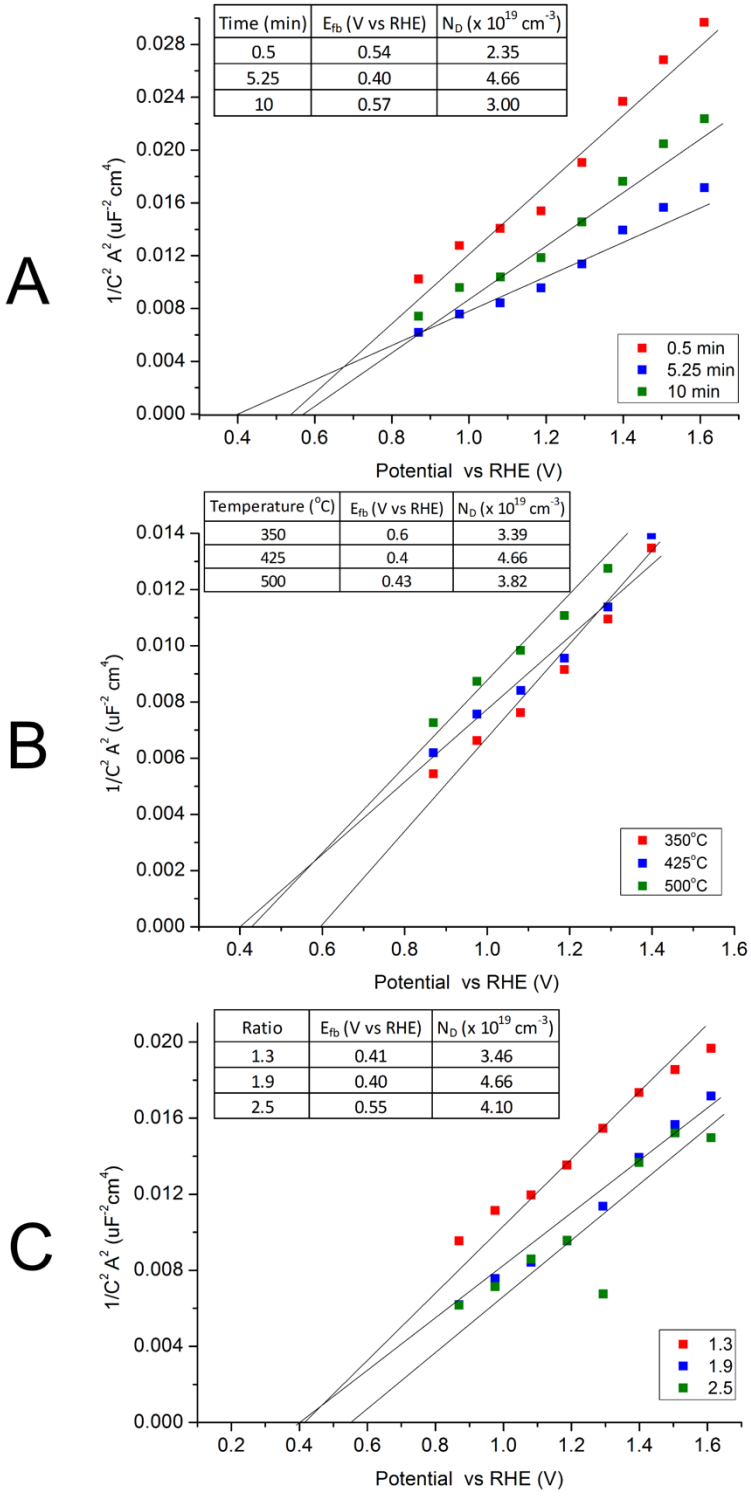

Figure A8. Mott-Schottky plots at various (A) electrodeposition time, (B) calcination temperature, and (C) Bi-KI to benzoquinone-EtOH ratio, measured at 7.6 kHz

Appendix 4

FE-SEM Images of BiOI

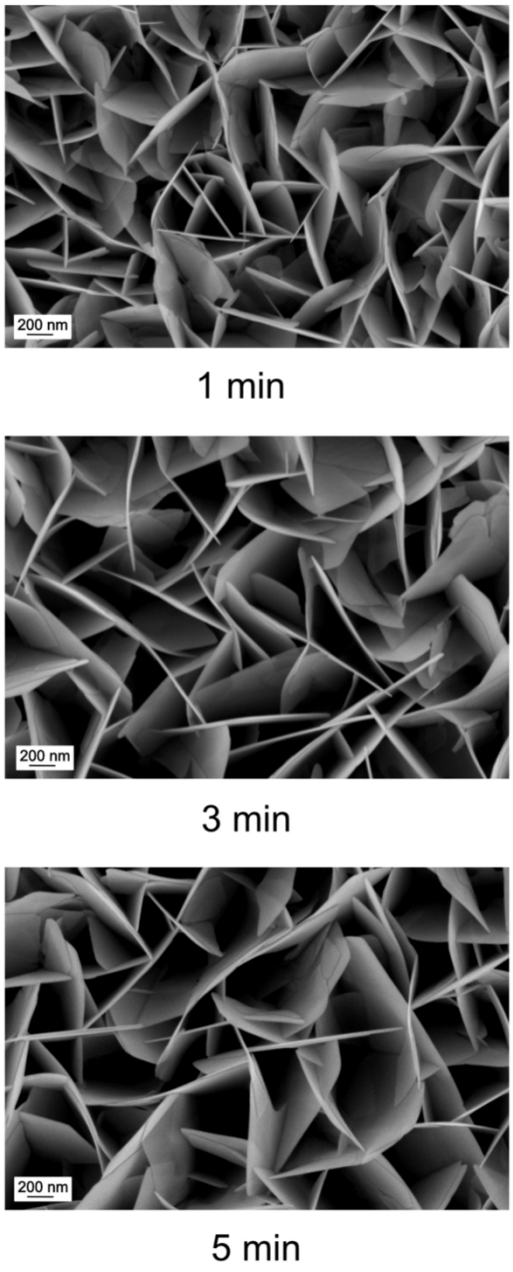

Figure A9. FE-SEM Images of electrodeposited BiOI at different electrodeposition time (1 min, 3min, and 5 min)

Appendix 5

GC calculations for n-BuLi titration

Given quantities:

Volume of gas balloon ($V_{balloon}$): 6000 mL
Volume of gas sample injected (V_{gas}): 0.5 mL
GC peak area: 2098.9
Surface area of $BiVO_4$: 3.4792 m^2/g
GC constant: 1.39 x 10^{-12}
Amount of $BiVO_4$ powder sample: 1.001 g

Calculation of amount of C_4H_{10}:

$$No.of\ moles\ of\ C_4H_{10} = \frac{GC\ peak\ area\ x\ V_{balloon}\ x\ GC\ constant}{No.of\ C\ atoms\ x\ V_{gas}}$$

$$No.of\ moles\ of\ C_4H_{10} = \frac{2098.9\ x\ 6000\ x\ 1.39\ x\ 10^{-12}}{4\ x\ 0.5}$$

$$\boldsymbol{No.of\ moles\ of\ C_4H_{10} = 8.752\ \mu mol}$$

Calculation of amount of OH:

$$No.of\ OH = \frac{Moles\ of\ butane\ x\ Avogadro's\ number\ x\ conversion\ factor}{Total\ amount\ of\ sample\ x\ Surface\ area}$$

$$No.of\ OH = \frac{8.752\ \mu mol\ x\ 6.0221\ 10^{23}\ atoms/mol\ \ x\ 10^{-18}}{1.001\ g\ x\ 3.4792\ m^2/g}$$

$$\boldsymbol{No.of\ OH = 1.51\ OH/nm^2}$$

Appendix 6

Possible $BiVO_4$ surface termination

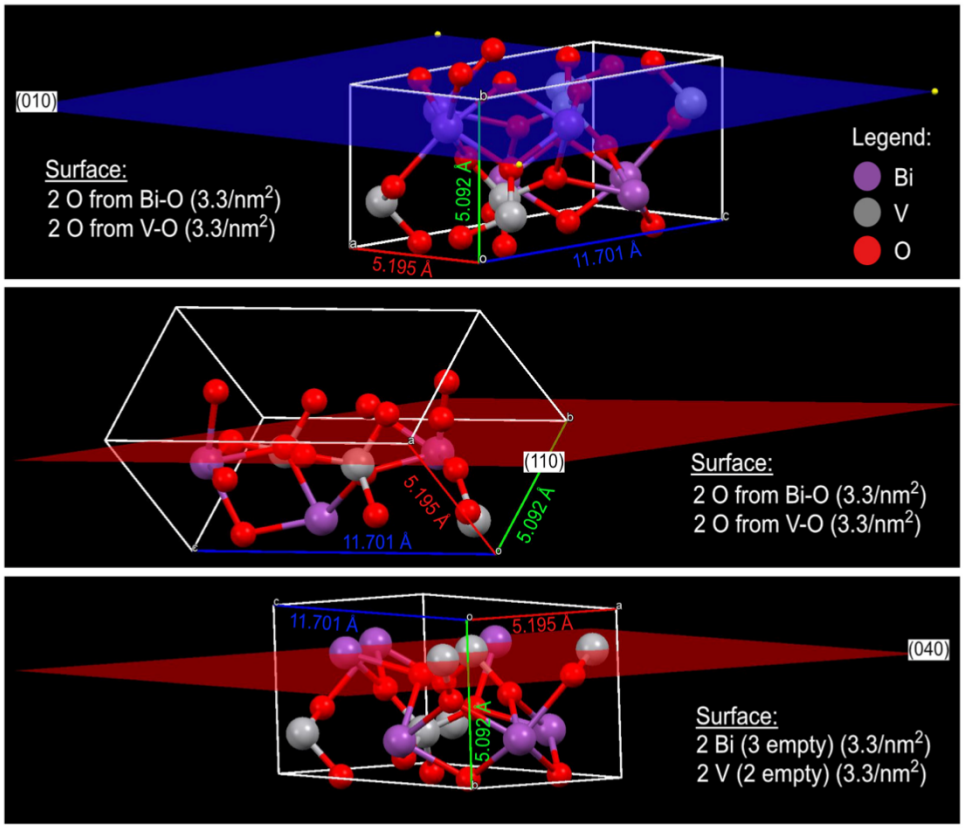

Figure A10. $BiVO_4$ surface termination considering (010), (110), and (040) surfaces

Appendix 7

Pyridine desorption IR spectra

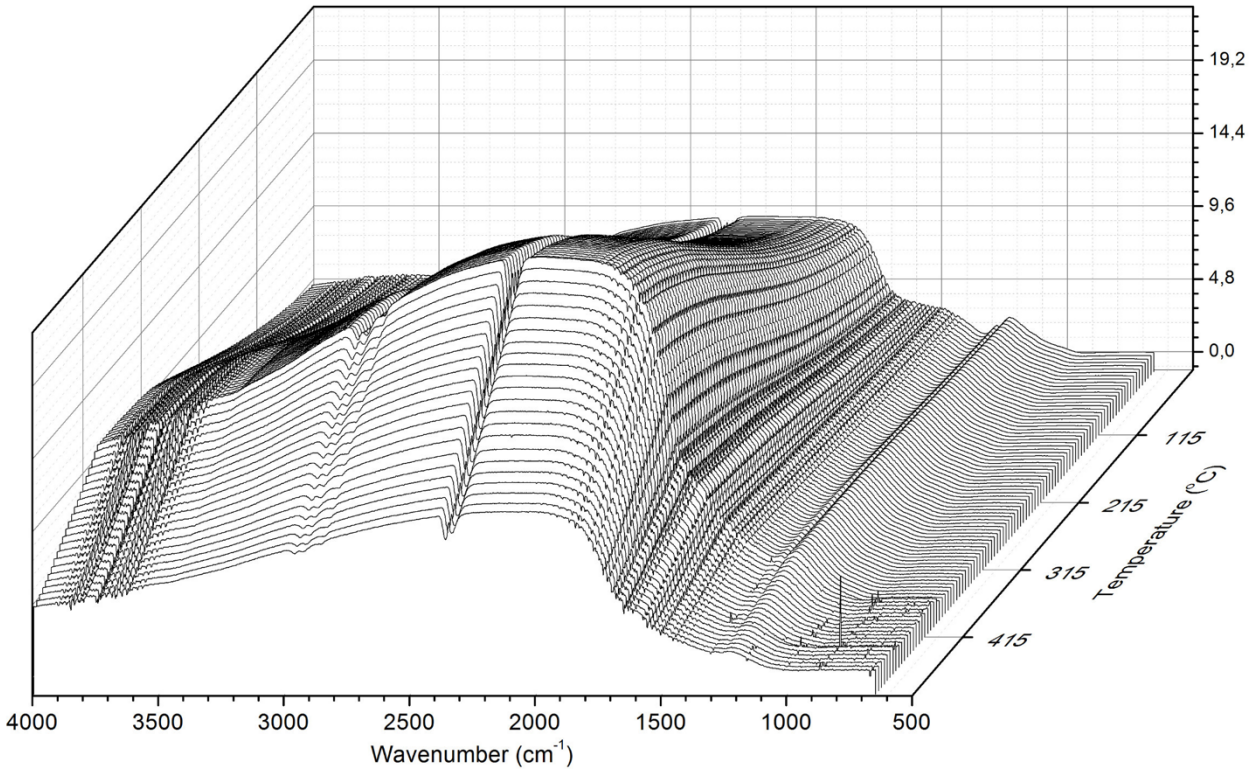

Figure A11. In-situ FTIR of pyridine adsorption-desorption from 20°C to 500°C at 5°C/min ramp rate

Appendix 8

GC calculations for Al_2O_3-modified $BiVO_4$ powder

1. 1st pulse: $AlMe_3$

Given quantities:

Volume of gas balloon ($V_{balloon}$): 10000 mL
Volume of gas sample injected (V_{gas}): 0.5 mL
GC peak area: 3625
Surface area of $BiVO_4$: 3.4792 m^2/g
GC constant: 1.39 x 10^{-12}
Amount of $BiVO_4$ powder sample: 1.9063 g

Calculation of amount of CH_4:

$$No.of\ moles\ of\ CH_4 = \frac{GC\ peak\ area\ x\ V_{balloon}\ x\ GC\ constant}{No.of\ C\ atoms\ x\ V_{gas}}$$

$$No.of\ moles\ of\ CH_4 = \frac{3625\ x\ 10\ x\ 1.39\ x\ 10^{-12}}{1\ x\ 0.5\ \mu L}$$

$$\boldsymbol{No.of\ moles\ of\ CH_4 = 0.1008\ mmol}$$

Calculation of molecules of CH_4:

$$No.of\ CH_4 = \frac{Moles\ of\ methane\ x\ Avogadro's\ number\ x\ conversion\ factor}{Total\ amount\ of\ sample\ x\ Surface\ area}$$

$$No.of\ CH_4 = \frac{0.1008\ mmol\ x\ 6.0221\ x\ 10^{23}\ atoms/mol\ x\ 10^{-18}}{1.9063\ g\ x\ 3.4792\ m^2/g}$$

$$\boldsymbol{No.of\ CH_4 = 9.15\ CH_4/nm^2}$$

2. 2nd pulse: degassed H_2O

Given quantities:

Volume of reactor ($V_{reactor}$): 200 mL
Volume of gas sample injected (V_{gas}): 0.5 mL
GC peak area: 16769
Surface area of $BiVO_4$: 3.4792 m^2/g
GC constant: 1.39 x 10^{-12}
Amount of $AlMe_3$-$BiVO_4$ powder sample: 0.9063 g

Calculation of amount of CH_4:

$$No.of\ moles\ of\ CH_4 = \frac{GC\ peak\ area\ x\ V_{reactor}\ x\ GC\ constant}{No.of\ C\ atoms\ x\ V_{gas}}$$

$$No.of\ moles\ of\ CH_4 = \frac{16769\ x\ 200\ mL\ x\ 1.39\ x\ 10^{-12}}{1\ x\ 0.5\ \mu L}$$

$$\boldsymbol{No.of\ moles\ of\ CH_4 = 9.32\ \mu mol}$$

Calculation of molecules of CH_4:

$$No.of\ moles\ of\ CH_4 = \frac{Moles\ of\ \ x\ Avogadro's\ number\ x\ conversion\ factor}{Total\ amount\ of\ sample\ x\ Surface\ area}$$

$$No.of\ CH_4 = \frac{9.32\ mol\ x\ 6.0221\ \ x\ 10^{23}\ atoms/mol\ \ x\ 10^{-18}}{0.9063\ g\ x\ 3.4792\ m^2/g}$$

$$\boldsymbol{No.of\ CH_4 = 1.8\ CH_4/nm^2}$$